Adaptive Optics based on Liquid Total Internal Reflection Mirrors

ii

Adaptive Optics based on liquid Total Internal Reflection Mirrors

Proefschrift

ter verkrijging van de graad van doctor
aan de Technische Universiteit Delft,
op gezag van de Rector Magnificus prof. ir. K.C.A.M. Luyben,
voorzitter van het College voor Promoties,
in het openbaar te verdedigen op maandag 31 maart 2014 om 10:00 uur

door

Eric Stephan TEN HAVE

natuurkundig ingenieur
geboren te Berlijn, Duitsland.

Dit proefschrift is goedgekeurd door de promotor:

Prof. dr. P.J. French

Samenstelling promotiecommissie:

Rector Magnificus,	voorzitter
Prof. dr. P.J. French,	Technische Universiteit Delft, promotor
Prof. C. Keller,	Universiteit Leiden
Prof. dr. ir. A.J.P. Theuwissen	Technische Universiteit Delft
Prof. dr. H.P. Urbach	Technische Universiteit Delft
Prof. dr. ir. M.H.G. Verhaegen	Technische Universiteit Delft
Dr. M. Gowin	
Dr. G.V. Vdovin	OKO Technologies
Prof. dr. ir. G.C.M. Meijer	Technische Universiteit Delft, reservelid

And then, that hour the star rose up,
the clearest, brightest star, that always heralds
the newborn light of day, the deep-sea-going ship
made landfall on the island . . . Ithaca, at last.

Homer
The Odyssey
translated by Robert Fagles, Penguin Books 1996.

to my mom

Contents

iii

Bibliography   129

List of Abbreviations   141

List of Figures   143

List of Tables   149

Summary   151

Samenvatting   155

Zusammenfassung   159

Acknowledgements   163

Publications   165

About the Author   167

Chapter 1

Outline

1.1 Thesis context

Any application using free space propagation of light through the atmosphere will be affected by the influence of the atmosphere on the quality of the propagating wavefront, e.g. astronomical observations or optical link telecommunication. All applications will suffer from adverse effects, e.g. beam spreading, scintillation, beam wander, and many others. In Astronomy this leads to a loss in image resolution and for free space laser applications to increased power requirements.

Adaptive Optics can be used to minimize and compensate the influence of the atmosphere. Generally, an Adaptive Optics system (Figure 1.1) consists of a wavefront sensor that receives light from an observed source and measures the distortions of the received wavefront, e.g. from a star in an astronomical imaging system or from a laser source in a free-space optical communication system. The measured wavefront is passed to a control unit that processes the data and calculates the necessary control signals for the wavefront corrector, e.g. a deformable mirror. The wavefront corrector is then configured in such a way that it compensates for the measured distortions, so that the atmospheric distortions at the receiver are corrected for.

An Adaptive Optics system can be realized and applied in different forms: e.g. in wavefront correction for the optimization of beam shapes, in Fine Imaging for
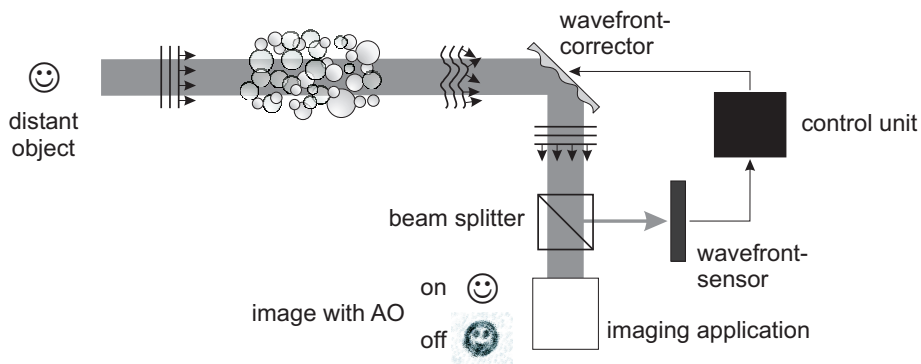
Figure 1.1: *Schematic setup of an Adaptive Optics system for an imaging application.*

the maximization of the sharpness of transmitted images, in Fine Tracking for the steering of a beam towards a moving target, or as a Spatial Light Modulator for modification of the shape of the beam.

This thesis concentrates on the central part of the Adaptive Optics system: the deformable mirror.
Generally, deformable mirrors consist of a solid reflecting surface to which an actuator structure is attached. Through manipulation of the actuators the shape of the mirror may be modified to fulfill a certain goal, e.g. the compensation of distorted wavefronts. There are different types of deformable mirrors:

- **Piezoelectric Mirrors**
  Piezoelectric mirrors are formed by a thin solid reflecting plate to which a two-dimensional array of actuators is directly attached (figure 1.2 (left)). Shaping of the mirror surface is effected by applying a voltage to the piezoelectric material, which will contract or expand perpendicular to the optical surface and locally push or pull the mirror [1, 2].
  Piezoelectric mirrors combine strokes of about 10 μm with high accuracy and allow the application of thousands of actuators. At the same time their resonant frequencies are far above 10 kHz making very short response times possible. However, they are complex to manufacture, require bulky electronics, and suffer from creep of the piezoelectric material. The mirrors require complex manufacturing processes that are time consuming and costly [1, 3].

- **Bimorph Mirrors**
  Bimorph mirrors also apply piezoelectric materials, but here two disks are bonded together, one of which is attached to the mirror surface. Bimorph mirrors use the transverse piezoelectric effect: when a voltage is applied one

disk will contract parallel to the mirror surface while the other disk will expand. The combined effect results in a curvature of the reflecting surface (figure 1.2 (right)) [1, 4].

Bimorph mirrors exhibit strokes of about 10 μm and good accuracy similar to piezoelectric mirrors, but with a limited number of actuators (hundreds) and much lower frequencies of a few hundred Hz. They may be manufactured with less complicated manufacturing processes at moderate costs, but still require bulky electronics and suffer from creep of the piezoelectric material. [1, 3, 5].
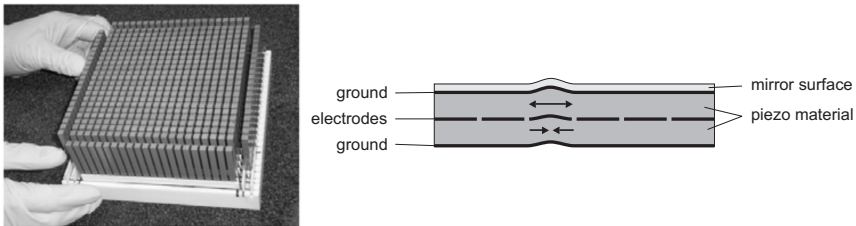
Figure 1.2: *Left: Example of a piezoelectric mirror [1], right: principle of the bimorph mirror.*

- **Membrane Mirrors**
  Membrane mirrors consist of a thin reflecting membrane with thicknesses around $0.5 - 10$ μm that is suspended at its edge above a two-dimensional electrode structure. Because the electrodes can only exert an attractive force on the membrane, it has to be biased in order to allow movement in both directions [2, 4, 6].
  While the total stroke of a membrane mirror may be as large as several tens of μm the individual strokes of each actuator are limited to a few μm. They display good accuracy, but the total diameter is limited to a few cm with an even smaller effective pupil, since the membrane is clamped at the edge. Membrane mirrors have negligible hysteresis and show hight temporal stability [2, 7, 8].

- **MEMS Mirrors**
  Micro electro-mechanical systems (MEMS) utilize the manufacturing techniques of the semiconductor industry to fabricate highly miniaturized and integrated mechanical and optical structures. This allows compact deformable mirrors with thousands of individual actuators. MEMS mirrors may apply a continuous reflecting membrane that is deformed by micro electrodes similar to a membrane mirror or a segmented mirror surface where the segments are manipulated by individual mechanical actuators [1, 9].

While MEMS mirrors allow thousands of actuators within a compact design with fast response times, at the same time their small size limits the available stroke to a few μm. In the case of individual actuators diffraction may degrade the imaging quality of the mirror [1, 3, 10].

- **Voice Coil Actuator Mirrors**
  For voice coil actuator mirrors the reflection surface is fitted with a large number of permanent magnets that are positioned opposite the voice coils. When a current is sent through the voice coil a magnetic field is created that interacts with the permanent magnet on the reflection surface. Similar to the membrane mirror the voice coil mirror needs to be biased, since it only allows a repelling force. Shaping of the mirror is effected by varying the current through the voice coils [1, 3, 11].
  Voice coil mirrors require large actuator spacing of about 30 mm to avoid interference between the individual magnetic fields and thus result in very large mirrors with diameters of 1 m and larger that can only be used for large astronomic telescopes. They allow strokes of 100 μm or more with an accurate position feedback through integrated capacitive sensors at reaction of about 1 ms. Because of the magnetic actuators these mirrors dissipate several kW of power and require sophisticated cooling systems that make the mirrors very complex to manufacture and expensive (several 10s of M€) [1, 3, 12, 13].
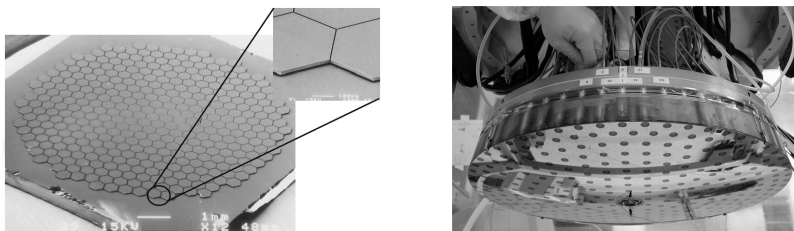
Figure 1.3: *Left: Example of a MEMS mirror [9], right: adaptive voice coil mirror of the MMT telescope [14].*

- **Liquid Crystal Spatial Light Modulators**
  In contrast to the above deformable mirrors a liquid crystal spatial light modulator (LC SLM) does not work through reflection of the light but through transmission. Electrically or optically addressable SLMs consist of a thin sheet of liquid crystal fluid that is sandwiched between two glass plates with transparant electrodes. Through their high resolution the information coded onto the electrode is directly translated to the intensity, phase, or polarization profile of the transmitted beam [15, 16].

LC SLMs offer the possibility of thousands of actuators, but their pixelated design leads to diffraction and aliasing effects. Furthermore, the modulation of the phase leads to chromatic effects that limit the use for broad wavelength applications. The maximum phase amplitudes are limited to a few π, which may be improved through phase wrapping to several tens of π. While nematic LC SLMs only allow frame rates of about 100 Hz, ferroelectric LC SLM make kHz frame rates possible[15, 17–19].

Piezoelectric mirrors are the most versatile of the above mentioned deformable mirrors - in principle, they allow large reflecting surfaces, good accuracy, many actuators, large strokes, and fast reaction times. However, real systems may be optimized for some of those parameters, but not all of them at the same time. Additionally, the cost of such a device increases exponentially with its size and complexity. Similar arguments hold for all deformable mirror technologies: certain tradeoffs will always have to be made. One thing all of these systems have in common though, is cost - even a low-cost deformable mirror costs several k€ [1, 20].

This thesis examines a novel deformable mirror that works on the basis of the electrostatic deformation of a liquid surface. Static electric fields are applied to manipulate a liquid surface which is used to shape the wavefronts of a laser beam via total internal reflection (TIR). This low-cost mirror was demonstrated in principle and was attributed with the following advantages [21]:

1. large surface displacements with relatively low applied voltages,

2. possibility of a large number of actuators,

3. possibility of adjustment of the dynamics and the influence function through modification of the physical properties of the liquid,

4. simple design without the need for sophisticated technology, and

5. close to 100% reflectivity for a broad wavelength range.

The goal of this thesis is to verify these claims, to demonstrate that the liquid mirror is capable of dynamically correcting distorted wavefronts, and to investigate the boundaries in which the liquid mirror may be used.

1.2   Overview of the Thesis

The thesis is structured as follows: chapter 2 covers the theory of turbulence and Adaptive Optics, it outlines the theory of the propagation of light through the atmosphere, reviews the theoretical framework of turbulence and its effects on beam propagation, and introduces Adaptive Optics for the compensation of the effects of turbulence as is relevant to this thesis. In chapter 3 all aspects regarding

the liquid nature of the liquid mirror are covered: the theoretical background for the electrostatic deformation of a liquid interface is reviewed and supported by results from simulations and experiments. The theory of sloshing is introduced and applied to the behavior of the liquid in the context of the volume containing the liquid for the liquid mirror. The physical parameters of the liquid are experimentally determined and compared to the predictions of theory. In chapter 4 the liquid mirror is applied in an optical setup where both aspects, the liquid behavior and the optical beam propagation, are experimentally investigated in different applications, i.e. the correction of distorted beams (wavefront correction), maximizing image sharpness (Fine Imaging), and beam shaping (spatial light modulation). Chapter 5 explores the possibilities for scaling of the liquid mirror. Based on the results of chapter 3 the prospects and limitations of making very large or very small liquid mirrors are investigated. Experiments are performed and linked to the results of chapter 4. In chapter 6 the results of the work will be summarized and recommendations and an outlook for further work will be given.

Because I know that time is always time
And place is always and only place
And what is actual is actual only for one time
And only for one place

<div align="right">

T. S. Eliot
The Waste Land and other poems, from the poem
"Ash-Wednesday" (1930), Faber and Faber Ltd. 1999.

</div>

Chapter 2

Basic Optics

In this chapter a concise introduction to the optical phenomena relevant to this thesis will be given. In particular, the topics of beam propagation through the atmosphere, turbulence, and Adaptive Optics (AO) will be elucidated. From the mathematical description of the effects of turbulence on a beam propagating through the atmosphere a number of important parameters can be derived that an Adaptive Optics system has to take into account. The interplay between these parameters and the properties of the AO system has important consequences for the ability of the AO system to successfully compensate atmospheric wavefront errors.

Any application involving the propagation of light will have to cope with the errors introduced by the optical path the light follows. An ideal collimated beam will consist of a succession of flat wavefronts perpendicular to the direction of propagation traveling along the optical path. Errors introduced during the propagation of the light will effect the wavefronts of the propagating beam, so that the wavefronts may no longer be flat nor perpendicular to the optical path.
The propagating wavefronts may be compared with sheets of paper: when more and more errors accumulate the initially flat sheets first start to bend and then show more and more wrinkles until they are completely creased. Once the wavefronts of the propagating beam are severely distorted they can be likened to crumpled pieces of paper (figures 2.1 and 2.2).
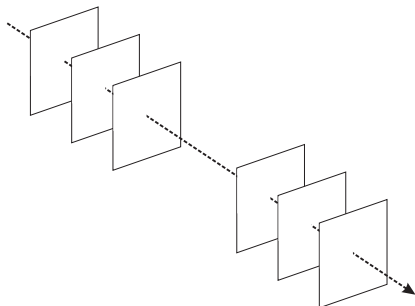
Figure 2.1: *An ideal beam with a succession of flat wavefronts.*
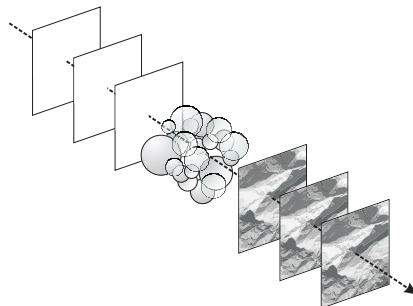
Figure 2.2: *Due to errors introduced by turbulence along the optical path the wavefronts are no longer flat.*

In table-top experiments with high quality optical elements the errors may be limited to a fraction of a wavelength so that they can be safely ignored. Other experiments may include propagation through turbulent media, e.g. air in atmospheric optics or the human eye in Ophthalmology, that introduce significant wavefront distortions that prohibit the acquisition of usable results. In that case Adaptive Optics can help to compensate the errors and obtain flat wavefronts at the end of the optical path.

This thesis examines a novel type of adaptive mirror that is based on the electrostatic deformation of a liquid surface on which the wavefronts of a laser beam can be shaped through total internal reflection.

2.1   Beam Propagation through the Atmosphere

While the wavefront distortion introduced by the human eye in Ophthalmology is mainly caused by imperfections of the interfaces of the different components of the eye, atmospheric distortions are caused by the bulk material of the medium, i.e. the air itself interacts with the beam. One manifestation of that interaction is the absorption of certain wavelengths, which is illustrated in figure 2.3 where the transmission spectrum of the atmosphere (left) and water vapor (right) are shown.

The propagation of light of wavelengths that are not absorbed is also influenced by the medium, since the atmosphere is a dynamic system. Local variations in temperature and humidity in the atmosphere can change the density of air, which leads to local variations in the index of refraction and thus the propagation of the
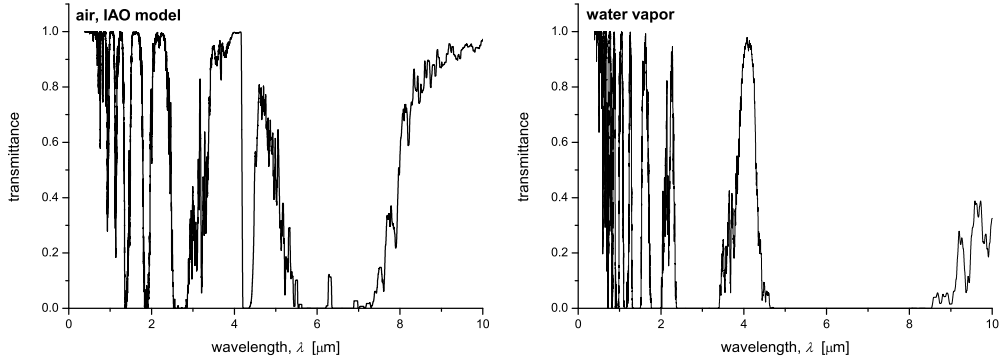
Figure 2.3: *Transmission spectra for air (left) and water vapor (right). The curves were obtained with* HITRAN *on the Web using the IAO model for the atmosphere (at zero altitude, mean latitudes, and summer season) for the atmospheric transmission and the molecular data of water for the water vapor transmission for path lengths of 1000 m [22–25].*
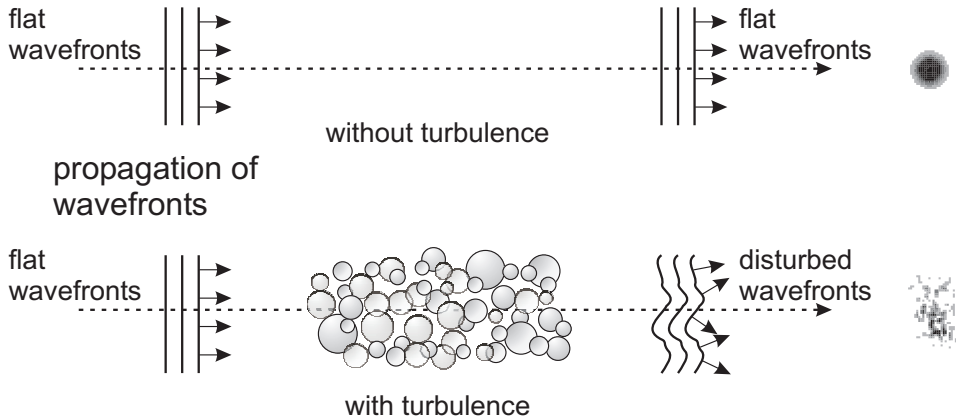
Figure 2.4: *Wavefronts propagating through the atmosphere are disturbed by turbulence.*

light. This is turbulence and will be described in detail in the next section. Turbulence disturbs the wavefronts (figure 2.4) leading to degradation of the quality of the beam profile.

2.1.1 Turbulence

Turbulence in the atmosphere is caused by local differences in, e.g., solar irradiation, temperature, humidity, or wind. This results initially in large bodies of air close to the ground with different physical properties. When two or more of these large bodies of air collide, they start to mix and form eddies. This leads to the disintegration of the large uniform bodies of air into smaller volumes with diverse physical properties (figure 2.5). Since the density of the atmosphere decreases exponentially with altitude, the effects of local differences of the physical properties are generally greatest in the boundary layer, i.e., the first 2.5 km above the ground, and decrease exponentially thereafter [26].

The effects of turbulence on the propagation of a beam of light is characterized by significant differences of scale in time and space: the difference in size between the wavelength of light and the size of the turbulence cells measures about five orders of magnitude. This means that diffractive effects are extremely small and can be neglected in most circumstances, which leaves the differences in the index of refraction to be considered (Rytov approximation, section 2.1.3) [26].
At the same time there is a difference of eleven orders of magnitude between the duration of a single oscillation of light and the typical persistence time of the turbulence. Thus, the turbulence can be regarded as 'frozen' for light passing through it [27]. The duration for which this assumption holds depends on the strength of the turbulence and the velocity of the wind, generally it is on the order of about one ms for strong turbulence [28].

For the understanding and quantitative analysis of the atmospheric processes that affect the beam propagation through the turbulence A. N. Kolmogorov developed a model of the occurring physical processes in 1941 [29, 30], which he refined in 1962 [31].

2.1.2 The Kolmogorov model

The Kolmogorov model is based on the transfer of energy from large structures to subsequently smaller and smaller structures within the Earth's atmosphere (figure 2.6).
The energy is supplied to the system by way of solar radiation: during daytime convection cells are directly heated by the sun at the Earth's surface while at night the energy is supplied by the mixing of air masses of different temperature. The large structures that put the energy into the system have typical sizes of L_0 of a few 100 m and form the 'outer scale' of the system. Through an energy cascade the energy is transferred to subsequently smaller structures by the decay of the turbulent flow until the energy is dissipated by molecular friction. At this point the structures have typical sizes of l_0 of a few mm and form the 'inner scale' of the system. L_0 and l_0 form the boundaries of the inertial range [32].
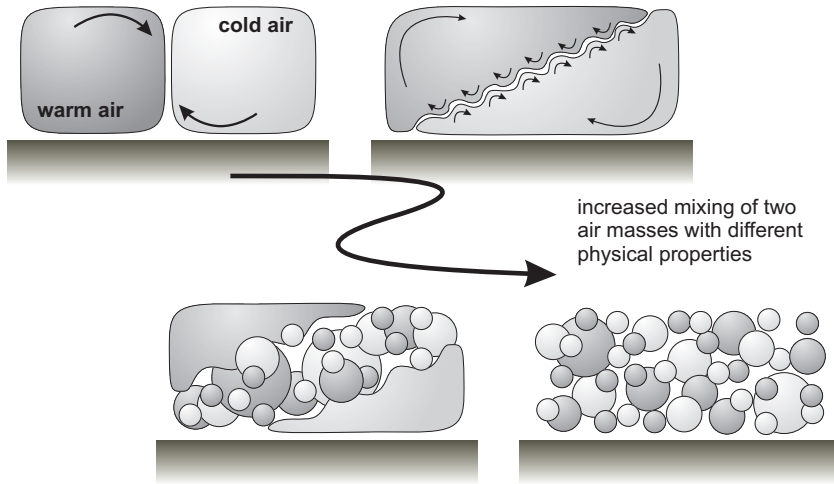
Figure 2.5: *Mixing of air masses with different physical properties.*
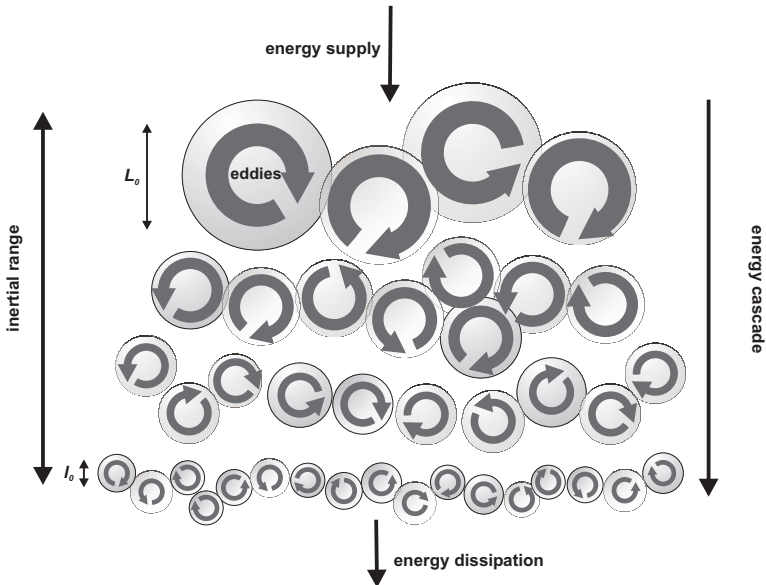
Figure 2.6: *The turbulent energy of the atmosphere is transferred through an energy cascade to subsequently smaller structures by the decay of the turbulent flow [33].*

For the energy cascade to proceed as a stable process, supply and dissipation of the turbulent energy have to be equal. This leads to the condition that the velocity fluctuation V in the atmosphere depends only on the scale ℓ and the energy dissipation ε, which means that the turbulent energy contained in eddies of size ℓ is proportional to $\ell^{2/3}$. When the wavenumber of a turbulent eddy is given by $\kappa = 2\,\pi/\ell$ and $\Phi(\kappa)$ is the spectral density of the fluctuations, the spectral power density for the one-dimensional case can be derived as:

$$\Phi(\kappa) \propto \kappa^{-5/3} \tag{2.1}$$

which is valid for all scale sizes within the inertial range, i.e. $L_0 > \ell > l_0$ [34].

A mathematical characterization of turbulence leads automatically to a description of the atmosphere. This description is based on a number of non-stationary stochastic meteorological quantities, e.g. temperature, pressure, or humidity, whose mean values vary over periods of minutes or hours. Difference functions can be used to differentiate these changes of the mean value from turbulent fluctuations:

$$F_t(\tau) = f(t + \tau) - f(t) \tag{2.2}$$

with $f(t)$ a non-stationary stochastic function representing the progression of a meteorological quantity [35]. In this way $F_t(\tau)$ is independent of slow changes in the mean value of $f(t)$, so that $F_t(\tau)$ can be regarded as a stationary stochastic function, even if $f(t)$ is not.
Then a structure function can be defined as:

$$D_f(\tau) = \langle [F_t(\tau)]^2 \rangle = \langle [f(t + \tau) - f(t)]^2 \rangle \tag{2.3}$$

with $\langle\rangle$ representing the mean value [35]. $D_f(\tau)$ is a measure for the magnitude of the fluctuations of $f(t)$ over periods of equal or smaller than τ. This approach is valid for all quantities t resp. τ that exhibit appropriate statistical characteristics. The characterization of turbulence involves primarily spatial properties of the atmosphere with $\langle\rangle$ representing the spatial mean value.
A structure function for the velocity of two eddies with a mutual distance r along a coordinate x can be defined as [36]:

$$D_v(r) = |V(x) - V(x + r)|^2 = C_V^2\, r^{2/3} \tag{2.4}$$

This is Kolomogorov's law and describes the mechanical characteristics of turbulence. The perturbations in the propagation of light are caused by fluctuations of the temperature and humidity dependent index of refraction, so that in a dry atmosphere in thermal equilibrium turbulence can occur without affecting the propagation of light [26].

However, under normal circumstances that does not happen, since turbulence causes the mixing of masses of air with different properties, generating fluctuations of temperature and humidity that have the same dimensions as the underlying eddies. This means that analogous to equation 2.4 a structure function for the refractive index variations can be derived:

$$D_n(r) = C_n^2 \, r^{2/3} \tag{2.5}$$

with C_n^2 the refractivity turbulence structure constant [34, 37].

The spectral power density of the refractive index variations for the three-dimensional case can be derived analogous to equation 2.1 [36, 38]:

$$\Phi_n(\kappa) = 0.033 \, C_n^2 \, \kappa^{-11/3}. \tag{2.6}$$

Equation 2.5 implies that with increasing distance the mean difference of the refractive index between two points increases to infinity. By introducing the outer scale of the system, L_0, the result is physically real again, since the difference of the refractive index between two points does not increase beyond L_0.
At the same time equation 2.6 implies that the power spectrum rises to infinity for $\kappa \to 0$. Again, the result makes sense physically with the introduction of the inner and outer scale, l_0 resp. L_0, in the modified von Karman spectrum (figure 2.7):

$$\Phi_n(\kappa) = \frac{0.033 \, C_n^2}{(\kappa^2 + \kappa_0^2)^{11/6}} \; \exp\left(-\frac{\kappa^2}{\kappa_m^2}\right) \tag{2.7}$$

with $\kappa_0 = 2 \, \pi / L_0$ and $\kappa_m = 2 \, \pi / l_0$ [39–41].
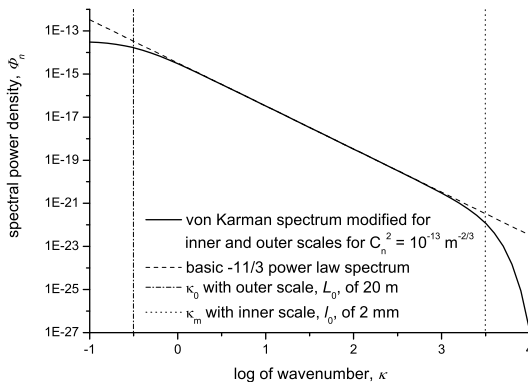
Figure 2.7: *Three-dimensional power spectrum of refractive index variations.*

2.1.3   Optical effects of turbulence

A description of turbulence is not enough for the correction of a disturbed beam of light through a turbulent atmosphere. The theory has to be expanded by a consideration of the effects of turbulence on the propagation of light, which include (see references for more information):

- beam spreading [32, 42],

- beam wander [32, 43–45],

- image jitter [32],

- loss of spatial coherence [45, 46], and

- scintillation [47–49].

The first effects can be described with perturbation theory with first and second order statistics, the Rytov formalism [34, 39, 45, 46, 50, 51]. Scintillation on the other hand is the occurrence of intensity fluctuations and requires fourth order statistics [52]. It manifests itself e.g. as the blinking of stars low over the horizon. Empirical evidence showed that in this case the Rytov approximation only holds for weak turbulence, which led to the introduction of the Markov approximation, in which the wave equation is substituted by a parabolic approximation [39, 42, 53].

In atmospheric optics, Fried's parameter or Fried's radius, r_0, is commonly used to describe the loss of spatial coherence:

$$r_0 = \left[0.423\, k^2\, \sec\left(\zeta\right) \int_0^L C_n^2\left(h\right)\, dh \right]^{-3/5} \tag{2.8}$$

with ζ the zenith angle of the beam direction [4].
Fried's parameter corresponds to the radius over which the variance of the phase fluctuations has a value of $1\,\mathrm{rad}^2$ [26, 54].

2.1.4   Turbulence dynamics

An Adaptive Optics system measures and corrects the wavefront error along a single optical path. If the corrected beam propagates along a path that differs by an angle θ from the original optical path, additional so called anisoplanatic errors are introduced, since the turbulence along the two paths is different.

The isoplanatic angle corresponds to the angle over which the turbulence is practically constant and the resulting variance of the phase fluctuations have a value of $1\,\text{rad}^2$ [52]. The isoplanatic angle is given by:

$$\theta_0 = \left[2.914\, k^2\, \sec\left(\zeta\right)^{8/3} \int_0^L C_n^2\left(h\right) h^{5/3}\, dh \right]^{-3/5} \tag{2.9}$$

with ζ the zenith angle [26].

Since the time scale for changes of turbulence is much larger than for an oscillation of light, atmospheric turbulence is assumed to be frozen [27, 55]. This means that the structure of turbulence for a time τ_0 is constant. The time, for which this assumption is true, resp. the frequency, $f_G = 1/\tau_0$ (Greenwood frequency), with which the structure of the turbulence changes, is given by:

$$f_G = \left[0.102\, k^2\, \sec\left(\zeta\right) \int_0^L C_n^2\left(h\right) v\left(h\right)^{5/3}\, dh \right]^{3/5} \tag{2.10}$$

with ζ the zenith angle and v the velocity of the wind along the beam propagation path [56].

It is assumed that for an Adaptive Optics system the frequency with which the wave fronts have to be measured resp. corrected has to be larger than the Greenwood frequency by at least a factor of six [57]:

$$f_{AO} = 6 \cdot f_G. \tag{2.11}$$

These three parameters, the Fried parameter, r_0, the isoplanatic angle, θ_0, and the Greenwood frequency, f_G, essentially determine the performance of an Adaptive Optics system [58].

2.2   Adaptive Optics

The main goal of an Adaptive Optics system is to compensate the degradation of the beam profile caused by passing through a turbulent medium, e.g. the human eye or the atmosphere. In imaging applications, e.g. Ophthalmology or Astronomy, this is achieved by compensation of the wavefront errors after the beam has passed through the atmosphere (Figure 2.8, A and B) [59–65].

This requires knowledge about the state of the turbulence so that the Adaptive Optics system can be set to the corresponding shape. Because the atmosphere is

A propagation through turbulence without Adaptive Optics

flat
wavefronts

aberrated
wavefronts

B imaging through turbulence with Adaptive Optics

flat
wavefronts

AO

aberrated
wavefronts

flat
wavefronts

C beam projection through turbulence with Adaptive Optics

AO

flat
wavefronts

aberrated
wavefronts

flat
wavefronts
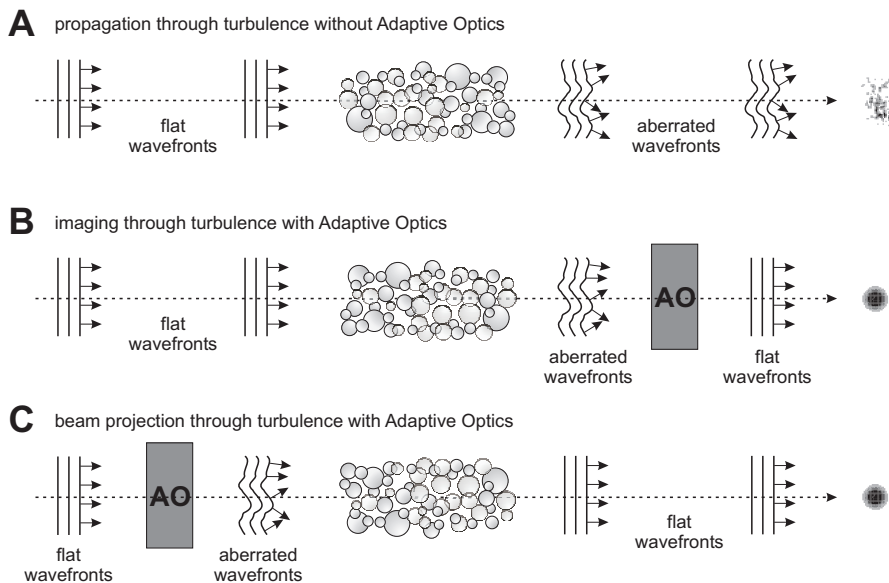
Figure 2.8: *Application of Adaptive Optics systems – A: without AO the wavefronts are aberrated after passing through turbulence; B: compensation of turbulence in imaging applications – the wavefront errors are compensated after the light has passed through the turbulence and before detection; C: compensation of turbulence in beam projection applications – the wavefront errors are compensated before the beam passes through the turbulent atmosphere.*

a dynamic system and changes its state with time, the Adaptive Optics system consists necessarily of a wavefront sensor and a wavefront corrector. The Adaptive Optics system additionally requires a control unit to link the information from the wavefront sensor to the wavefront corrector.

Thus the wavefront sensor measures the current state of the atmosphere and relays that information to the control unit. The control unit processes the wavefront data and calculates the signals for the wavefront corrector in order to control the movement of the actuators. The actuators modify the wavefront corrector such that the wavefronts of the beam are shaped so that the errors introduced by the propagation through the turbulence are correctly compensated and the beam regains its flat wavefronts.

When the wavefront analysis is performed on the light of beam of interest itself the mode of operation is called wavefront correction which is examined in section 4.1 of this thesis. When the wavefront analysis is performed on the light of a different source that travels collinear with the beam of interest, as with Ophthalmology or Astronomy when a Laser Guide Star (LGS) is used, this mode of operation is sometimes called Fine Imaging which is investigated in section 4.2.

In the same way an Adaptive Optics system functions for an optical system that projects a beam through the atmosphere, e.g. for optical communication. If the current state of the turbulence is known, a wavefront corrector can shape the wavefronts of the beam at the sending location in such a way that the flat wavefronts are recovered after the beam has passed through the turbulence (Figure 2.8, A and C).
The ability to shape wavefronts in a desired way is explored in section 4.3 where the liquid mirror is used a spatial light modulator.

2.2.1   Representation of Wavefronts with Zernike modes

Similar to Fourier analysis of wave patterns, wavefronts too can be represented by a series of orthogonal modes of increasing order. Different sets of polynomials may be used, but in optics commonly two-dimensional Zernike polynomials are used, since these are defined in polar coordinates on a unit circle, which makes them especially useful when round apertures are used. Also, the Zernike polynomials allow a more accurate representation of the wavefronts than a corresponding zonal representation, where the wavefront is represented by an array of subapertures. At the same time Zernike polynomials of low order correspond to well-known optical modes like focus and astigmatism [26, 66, 67].

Zernike polynomials are defined in polar coordinates with azimuthal frequency m and radial degree n, with $m \leq n$ and $n - m$ even. Generally, Zernike polynomials are ordered in such a sequence j that even values of j correspond to the symmetrical modes with $\cos(m\,\theta)$ and odd vales of j correspond to asymmetric modes with $\sin(m\,\theta)$. The polynomials are normalized such that the variance over the unit circle equals one and are given by [68]:

$$
\begin{aligned}
Z_{evenj} &= \sqrt{n+1}\, R_n^m(r)\, \sqrt{2}\, \cos(m\,\theta) && \text{for } m \neq 0 \\
Z_{oddj} &= \sqrt{n+1}\, R_n^m(r)\, \sqrt{2}\, \sin(m\,\theta) && \text{for } m \neq 0 \\
Z &= \sqrt{n+1}\, R_n^0(r) && \text{for } m = 0
\end{aligned}
\tag{2.12}
$$

with

$$
R_n^m(r) = \sum_{S=0}^{(n-m)/2} \frac{(-1)^S\,(n-S)!\,r^{n-2S}}{S!\,\left[\frac{n+m}{2}-S\right]!\,\left[\frac{n-m}{2}-S\right]!}.
\tag{2.13}
$$

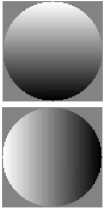The first 15 Zernike polynomials with their corresponding graphical representations are summarized in table 2.1.
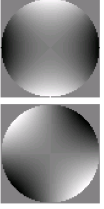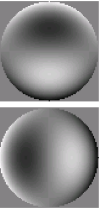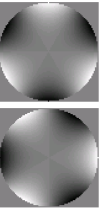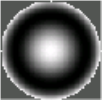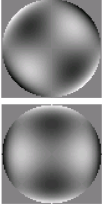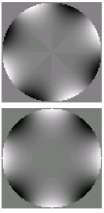
radial degree, n	azimuthal frequency, m				
	0	1	2	3	4
0	$Z_1 = 1$ piston				
1		$Z_2 = 2\,r\cos\theta$ $Z_3 = 2\,r\sin\theta$ tip and tilt			
2	$Z_4 = \sqrt{3}\,(2\,r^2 - 1)$ focus		$Z_5 = \sqrt{6}\,r^2\sin 2\theta$ $Z_6 = \sqrt{6}\,r^2\cos 2\theta$ astigmatism		
3		$Z_7 = \sqrt{8}\,(3\,r^2 - 2\,r)\sin\theta$ $Z_8 = \sqrt{8}\,(3\,r^2 - 2\,r)\cos\theta$ coma		$Z_9 = \sqrt{8}\,r^3\sin 3\theta$ $Z_{10} = \sqrt{8}\,r^3\cos 3\theta$ trifoil	
4	$Z_{11} = \sqrt{5}\,(6\,r^4 - 6\,r^2 + 1)$ spherical abberation		$Z_{12} = \sqrt{10}\,(4\,r^4 - 3\,r^2)\cos 2\theta$ $Z_{13} = \sqrt{10}\,(4\,r^4 - 3\,r^2)\sin 2\theta$ secondary astigmatism		$Z_{14} = \sqrt{10}\,r^4\cos 4\theta$ $Z_{15} = \sqrt{10}\,r^4\sin 4\theta$ quatrefoil

Table 2.1: *Zernike polynomials [68, 69].*

An arbitrary phase function $\phi(r.\theta)$ across a round aperture can be represented as a sum of Zernike polynomials [26]:

$$\phi(r,\theta) = \sum_{0}^{\infty} a_j \, Z_j(r,\theta) \qquad (2.14)$$

where the amplitudes of the Zernike polynomials is given by [26]:

$$a_j = \int \phi(r,\theta) \, Z_j(r,\theta) \, d^2r. \qquad (2.15)$$

The amplitude of the modes decreases with increasing mode number, since the Kolmogorov power spectrum possesses a $f^{-8/3}$-dependence. If Zernike polynomials are used as basis for the compensation of turbulence, the low order modes, i.e. tilt, focus, and astigmatism, are compensated first [26].

2.2.2   Compensation of turbulence

An Adaptive Optics system consists of a wavefront sensor that measures the shape of the wavefront. This information is routed to a control unit that processes the data and calculates the signals to drive the wavefront corrector that actually corrects the wavefront abberations. During all these steps errors can occur, so that the resulting wavefront correction may not compensate the actual wavefront deformation.

The residual total error of the wavefront, σ_{AO}, can be represented by the sum of the errors due to the constituent components of the AO system:

$$\sigma_{AO}^2 = \sigma_F^2 + \sigma_{WFS}^2 + \sigma_{TR}^2 + \sigma_{TD}^2 + \sigma_A^2 \qquad (2.16)$$

with σ_F the fitting error due to the ability to only imperfectly measure (with the wavefront sensor) and recreate (with the deformable mirror) the shape of the wavefront, σ_{WFS} the error due to signal and noise limitations in the wavefront sensor, σ_{TR} the error due to a limited bandwidth of the feedback system, σ_{TD} the error due to the delay between measurement and correction of the wavefront, and σ_A the error due to spatial lag when tracking a moving target [26, 70].

When looking at the characteristics of a deformable mirror only the fitting error, σ_F, the bandwidth error, σ_{TR}, and the delay error, σ_{TD}, are of importance, since these wholly or partly depend on the properties of the mirror. Therefore they will be looked at in more detail; the other errors are completely determined by other factors.

2.2.2.1   The fitting error

The fitting error is given by:

$$\sigma_F^2 = c_F \, N_S^{-5/6} \left(\frac{D}{r_0}\right)^{5/3} \tag{2.17}$$

with c_F a formfactor that depends on the characteristics of the wavefront sensor and the deformable mirror, N_S the number of actuators or rather the number of corrected modes, D the diameter of the sending aperture, and r_0 Fried's radius [26, 70].

Only two of these parameters actually depend on the characteristics of the mirror, i.e. the formfactor, c_F, and the number of actuators, N_S.
While the influence of the number of actuators is quite straightforward to see, the value of the formfactor depends subtly on the properties of the mirror, viz. c_F generally lies between $0.14 \, \text{rad}^2$ for mirrors with actuators that have both piston and tilt and $1.26 \, \text{rad}^2$ for mirrors with actuators that only have piston. Mirrors whose actuators show complex influence functions like pyramid- or Gauss-functions have formfactors between $0.2 \, \text{rad}^2$ and $0.3 \, \text{rad}^2$ [26].

Thus, it is essential to examine the formfactor of the liquid mirror and determine the parameters the formfactor depends on.

2.2.2.2   The bandwidth error

The bandwidth error is given by:

$$\sigma_{TR}^2 = \kappa \left(\frac{f_G}{f_S}\right)^{5/3} \tag{2.18}$$

with κ a constant depending on the frequency characteristic of the actuators, f_G the Greenwood frequency (equation 2.10), and f_S the actuator bandwidth [26].

Here also two parameters depend on the characteristics of the mirror, viz. the constant, κ, and the bandwidth, f_S. Similar to the number of actuators for the fitting error, the influence of the bandwidth of the actuators is quite obvious, while the dependence of κ is more complicated, viz. κ equals unity for simple resistor/capacitor frequency characteristics with a FWHM-value of f_S and $\kappa = 0.191$ when the frequency characteristic shows a sharp drop at the frequency f_S [26].

Here, it is necessary to examine the frequency characteristic of the liquid mirror to establish f_S and κ and on which parameters they depend.

2.2.2.3   The delay error

The delay error is given by:

$$\sigma_{TD}^2 = 28.4 \ (\tau_S \cdot f_G)^{5/3} \tag{2.19}$$

with τ_S the time between the measurement of the wavefront to be corrected and the actual correction and f_G the Greenwood frequency (equation 2.10) [26].

The delay time of the system, τ_S, can be expressed as the sum of the delay time introduced by the mirror, τ_M and the rest of the system, τ_R:

$$\tau_S = \tau_M + \tau_R \tag{2.20}$$

which means that the dependency of the delay time of the mirror, τ_M, on the properties of the mirror can directly be examined.

The formfactor, as well as the frequency characteristics, and the delay time, τ_M, of the liquid mirror will be examined in chapter 3 while the delay time of the liquid mirror used in an adaptive optical feedback system, $\tau_S = \tau_M + \tau_R$, will be examined in chapter 4.

Haru no umi
Hinemosu
Notari notari kana

In the spring sea
Waves undulating and undulating
All day long

Yosa Buson
Classic Haiku, translated by Yuzuru Miura,
Charles E. Tuttle Company, Inc. 1995.

Chapter 3

Development of Fluidic Adaptive Optics

While solid objects are fixed in their shape and restricted in their movement, fluids do not have a rigid structure or a permanently fixed form. This allows liquid volumes to adapt their shape to their surroundings, e.g. to a reservoir or container. A liquid body may be disturbed by an object moving through it or be excited at its interface such that the liquid motion results in surface waves, but eventually the perturbation energy will dissipate and the liquid body will return to its original state.

This ability of liquids to take any possible shape and have different volume elements move with respect to each other promises to be a very useful tool in Adaptive Optics when applied as a deformable mirror. Here, the shape that a deformable mirror may take is nor longer restricted by the inflexibility of its solid-state reflecting surface, but in principle allows any imaginable shape. Contrariwise however, the lack of rigidity may cause additional problems due to unwanted dynamics that may introduce larger errors to an optical system than the deformable mirror is able to correct in the first place.

This chapter examines the deliberate static deformation of the liquid surface for the reflection of an optical beam and the shaping of its wavefronts as well as the dynamics of the liquid volume that lead to unwanted oscillations of the surface. The application of the liquid mirror for Adaptive Optics is investigated in the next chapter.

Here, the theory describing the electrostatic deformation of the liquid is reviewed and the influence function of the mirror theoretically and experimentally determined. The characteristic open-loop frequency response and rise- and damping-times of the liquid mirror are investigated and the theory describing the oscillatory behavior and possible resonances of the liquid in a container is reviewed and applied to liquid mirror and compared to the measured dynamic behavior.

3.1   Liquid Mirrors in Adaptive Optics

Liquids have long been used in Astronomy and Adaptive Optics – from liquid mercury mirrors applying mechanical rotation [71–73] or the magnetic field of an applied current [74] to liquid mirrors applying magnetically deformable ferromagnetic liquids [75, 76] and electrocapillary actuation [77].

All these mirrors suffer from their dissipative nature, which leaves the shaped liquid surfaces unstable with time. Once the driving mechanism of the mercury mirrors is stopped, the liquid level will equalize and the parabolic shape will be lost, likewise, the liquid level of the mirror deformed by electrocapillary actuation will level with time. Furthermore, the magnetic liquid mirrors require a constant current through the coils to keep the desired shape.

Here, the deformation is effected by the application of a static electric field, the function of which has first been demonstrated in 2009 [21]. The use of an electrostatically deformed liquid surface for Adaptive Optics is in fact much older: Babcock envisioned this in his seminal paper in 1953 [63]. He thought of attaching a so-called *Eidophor* [78], where a charge was deposited onto a thin oil film on a flat mirror by means of a cathode ray, to a telescope. However, similar to the other dissipative methods described above, the localized charge deposited on the oil film will equalize with time and the shape of the surface will be lost.

3.2   The Liquid Mirror

The liquid mirror consists of a metal container of radius, R, with a transparent coupling prism mounted into the bottom of the container to allow the light to couple into and out of the liquid mirror device (figure 3.1). The light is reflected

by total internal reflection from the surface of the liquid with depth, h, which can be electrostatically deformed by applying a voltage to the electrodes positioned above the liquid surface. In our case the radius of the liquid container was about $R = 47.5$ mm and the depth of the liquid about $h = 4$ mm.
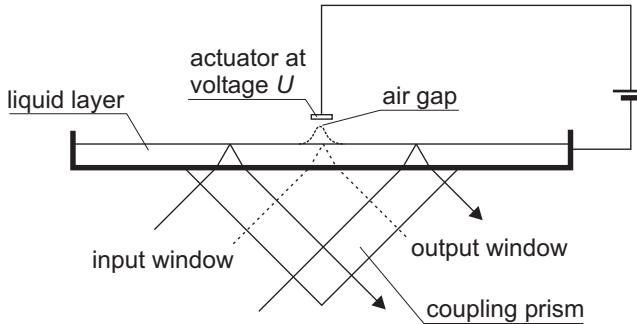
Figure 3.1: *The liquid mirror device.*

The shape of a liquid interface is defined by the forces acting on the liquid and can be deformed by an electrostatic force. Bodies of liquid or soft dielectric condensed matter tend to minimize the total surface energy and thus take on a shape that conforms to that condition. In connection with electric fields this means that the material moves to occupy space with a high electric field.

By placing a localized charge near such a surface a local electric field is created that modifies the shape of that surface. Thus, in principle it is possible to create a liquid surface with a desired shape by placing it in an appropriately designed electric field.

This is the principle for the application of the liquid mirror in Adaptive Optics: by creating an appropriate electric field near the surface of a liquid the shape of the surface can be formed in such a way that errors in the wavefronts of a beam of light that is bounced off the surface of the liquid by total internal reflection can be compensated.

The effect is not dissipative and once the field is set, the shape of the liquid mirror persists indefinitely. No constant source of energy is needed, since the electrodes act as capacitors that will keep their charge and thus the field shaping the liquid surface, even if the source to the electrodes is cut off. This allows for scaling this principle to be applied in very large scale adaptive optical applications, for example giant optical telescopes. Additionally, the use of this type of system is economically advantageous, since it is comparatively cheap to manufacture and the liquid offers a high quality optical surface at no additional cost.

3.3   Selection of the Liquid

In section 1.1 it was explicitly required that the liquid mirror be a low-cost device with a simple design and no need for sophisticated technology. These requirements include the fluid used for the liquid mirror device, which means that the ideal liquid should also be low-cost and should allow handling without special precautions or safety measures. Several household liquids that fulfill these requirements were available for use in the liquid mirror:

- water,

- an aqueous solution of 80% glycerol, and

- a white mineral oil.

The practicality of use of the different liquids is defined by their physical properties which were empirically determined. All three liquids have a low vapor pressure so that they do not evaporate easily and are clear and colorless so that wavelengths in the visible spectrum are transmitted unattenuated.

However, they differ in their viscosity and surface tension, which determine the dynamic behavior of the liquid. Preliminary measurements were performed to determine the most appropriate liquid for application in the liquid mirror using the setup described below in section 3.5.2.1.

3.3.1   Water

Water has a density of $\rho_{\text{water}} = 998.2$ kg/m^3, a viscosity of $\eta_{\text{water}} = 1.0$ mPa s, and a surface tension of $\gamma_{\text{water}} = 0.073$ N/m [79].
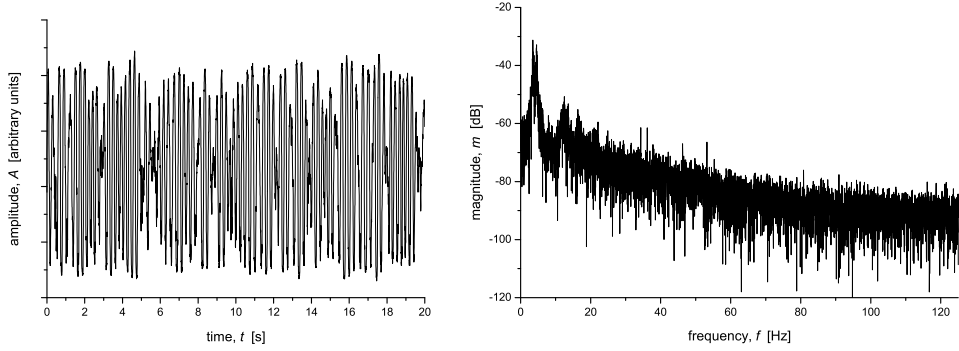
Ambient vibrations couple to the liquid container and generate waves on the liquid surface as shown in figure 3.2 (left). These surface oscillations have low frequencies around 4 Hz and relatively long wavelengths as shown in the Fourier spectrum in figure 3.2 (right). The damping time of these oscillations is about $\tau_{damp,\text{ water}} = 4$ s as shown in figure 3.3.

Due to the low viscosity of water ambient vibrations can couple easily to the liquid body and lead to large oscillations of the liquid surface that are hardly damped, so that the overall effect is a deflection of the beam that cannot be compensated by the Adaptive Optics system.
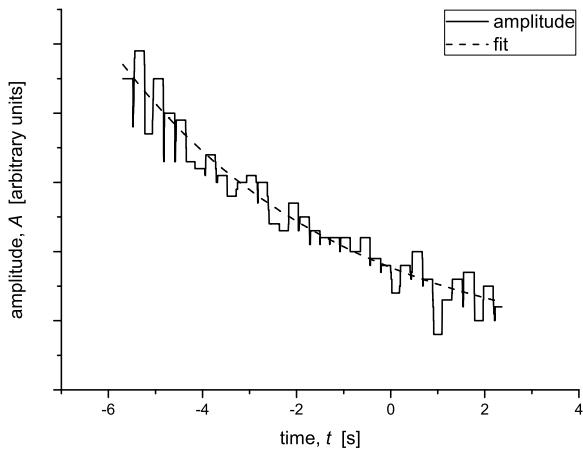
3.3.2   Glycerol

The aqueous solution of 80% glycerol has a density of $\rho_{\text{gly}} = 1208.5$ kg/m^3, a surface tension of $\gamma_{\text{gly}} = 0.0657$ N/m, and a viscosity of $\eta_{\text{gly}} = 59.9$ mPa s [79].
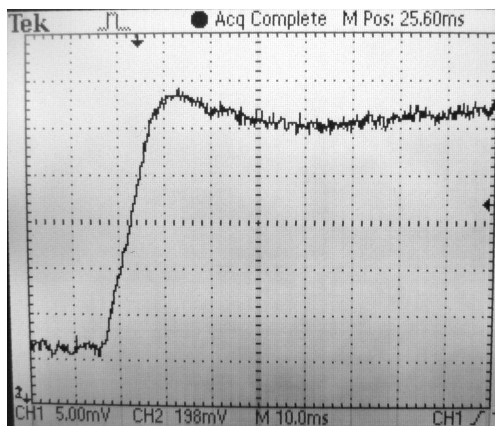
Figure 3.2: *Response of the water surface to ambient vibrations in the time domain (left) and the frequency domain (right). The Fourier spectrum shown that a lot of dynamic kinetic energy is coupled to the liquid surface at low frequencies of up to* 70 Hz.

Figure 3.3: *Damping of a wave on the water surface, the damping time is about* $\tau_{\mathrm{damp,\,water}} = 4$ s.

Figure 3.4: *Measurement of the rise-time of the aqueous solution of 80% glycerol: $\tau_{\text{rise, glycerol}} = 14$ ms. Similarly to water, the glycerol surface also exhibits surface oscillations caused by ambient vibrations as exemplified by the half wave to the right of the jump, the amplitude however is much lower in relation to the jump than for water.*

Due to the higher viscosity ambient vibrations do not couple as easily to the aqueous solution of 80% glycerol, so that the surface oscillations are much weaker. This makes it possible to measure the rise-time of the glycerol as a response to an electrostatic field as shown in figure 3.4. The response time of glycerol is $\tau_{\text{rise, glycerol}} = 14$ ms, which will make the operation of an Adaptive Optics system with the liquid mirror possible.

3.3.3 Oil

White mineral oil has a density of $\rho_{\text{oil}} = 860$ kg/m^3, a viscosity of $\eta_{\text{oil}} = 38.0$ mPa s, and a surface tension of $\gamma_{\text{oil}} = 0.03$ N/m [80–82].

The viscosity of the oil is also higher than that of water, so that ambient vibrations do not couple easily to the liquid surface, which makes a measurement of the rise-time possible. However, contrary to the short rise-time of glycerol, oil exhibits a dual behavior: in addition to a short rise-time of $\tau_{\text{rise, oil, fast}} = 44$ ms a very slow component of $\tau_{\text{rise, oil, slow}} = 55$ s was measured, as shown in figure 3.5. The quick time component allows the operation of the Adaptive Optics system. Since the time components are separated by three orders of magnitude operation of the system may still be possible, but a detrimental effect of the slow time component on the result cannot be ruled out completely.

Figure 3.6 shows a Bode-plot of the open-loop frequency response of the oil layer. The effective bandwidth is about 10 Hz, which will basically limit the Adaptive Optics system to the correction of static aberrations.
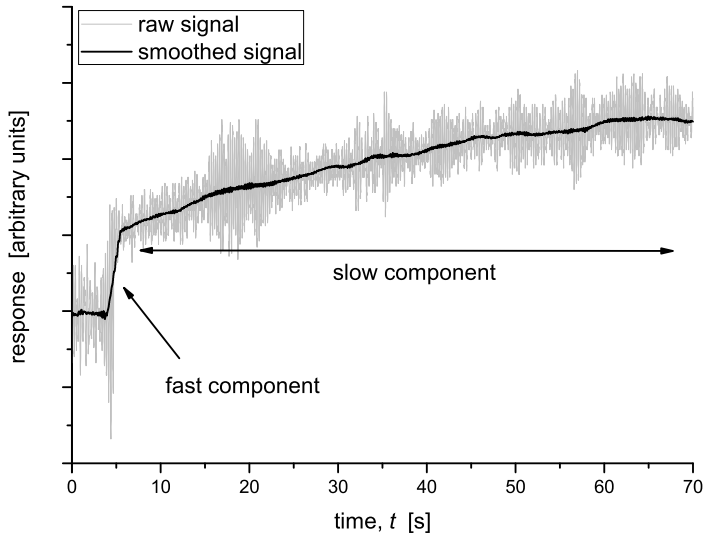
Figure 3.5: *Measurement of the rise-time of white mineral oil: the curve shows a behavior with a quick and a slow time component with $\tau_{\text{rise, oil, fast}} = 44$ ms and $\tau_{\text{rise, oil, slow}} = 55$ s.*
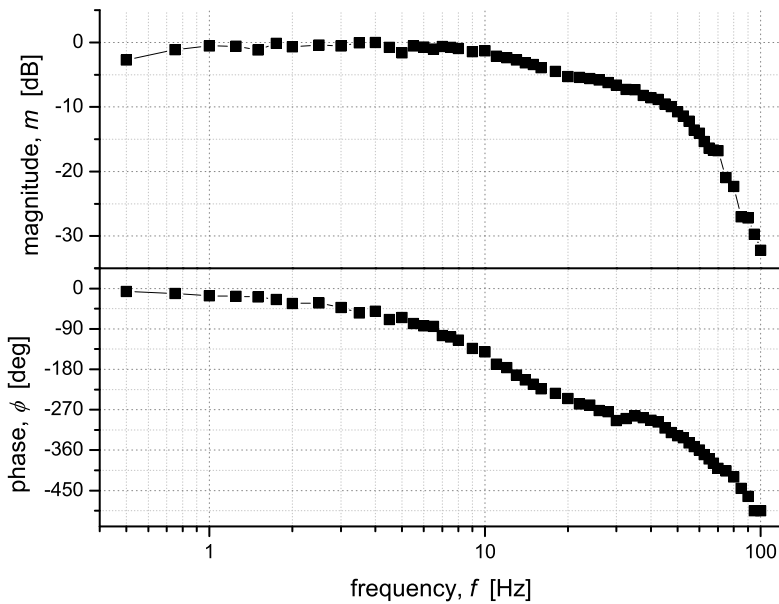
Figure 3.6: *Bode-plot of the open-loop frequency response of white mineral oil, the bandwidth is limited to about 10 Hz.*

3.3.4   Discussion

Three liquids, i.e. water, an aqueous solution of 80% glycerol, and white mineral oil, were evaluated for use with the liquid mirror, the results are summarized in table 3.1.

liquid	density, ρ [kg/m^3]	surface tension, γ [mN/m]	viscosity, η [mPa s]	suitability
water	998.2	73	1.0	✗
glycerol	1208.5	65.7	59.9	✓
oil	860	30	38.0	✗

Table 3.1: *Summary of the liquids evaluated for use in the liquid mirror [79–82].*

Water was eliminated due to the large coupling of ambient vibrations to the liquid surface. In this case the shape of the surface would be completely dominated by the surface oscillations instead of the electrostatic field.

The white mineral oil was also eliminated – here, the slow time component has a long lasting detrimental effect on the function of the Adaptive Optics system. Additionally, the limited bandwidth prevents the correction of dynamic aberrations.

Glycerol was chosen for use with the liquid mirror, since it prevents the strong coupling of ambient vibrations to the liquid mirror, but at the same time still exhibits quick rise-times.

A more detailed analysis of the dynamic behavior of glycerol can be found in section 3.5. While glycerol is well suited to be used with the liquid mirror, it is unlikely that it is the perfect liquid for this purpose, section 5.2.5.3 discusses possibilities for further improvement of the liquid properties.

3.4   Shaping the Liquid Surface by Static Electric Fields: the Influence Function of the liquid mirror

During electrostatic deformation of the liquid surface, three forces are acting on each element of the liquid surface:

- the electrostatic force,

- surface tension, and

- gravity.

The equilibrium situation in which all forces cancel each other is described by:

$$F_{elec} - F_{grav} - F_{surface} = 0. \tag{3.1}$$

The electrostatic deformation may be induced by a flat electrode positioned parallel to the liquid surface. The electric field at the surface of the liquid created by applying a voltage to an electrode above the liquid is oriented perpendicular to the surface. The gravitational force acts only in the vertical direction pulling the liquid down while the only force having a horizontal component is the surface tension which results in a smoothing of the surface deformation.

Without surface tension there is no horizontal component and the surface deformation would be a column of liquid with the footprint of the shape of the electrode rising out of the liquid. With infinite surface tension the electrostatic force would have to pull up the liquid over the entire surface of the liquid body. These two extremes show that the width of the induced surface deformation and thus the influence function of the actuators depend both on the geometry of the electrode and the surface tension of the liquid. Further analysis of the geometry indicates that a higher surface tension pulls up more liquid outside of the footprint of the electrode making the actual width of the deformation also dependent on the gravitational force, i.e. the density of the liquid.

From an analysis of the units it is expected that the width of the induced deformation, w, is given by the formula:

$$w = c_1 + c_2 \cdot r + c_3 \cdot \sqrt{\frac{\gamma}{\rho \cdot g}} + \text{higher orders}(r, \rho, \gamma), \tag{3.2}$$

with r the radius of the electrode, γ the surface tension, ρ the density of the fluid, g the gravitational constant, and c_1, c_2, and c_3 constants to be determined [83]. The constants themselves may be functions of r and ρ. The length

$$a = \sqrt{\frac{2\,\gamma}{\rho \cdot g}} \tag{3.3}$$

is called the capillary constant and indicates the length scale on which effects of surface tension will be comparable to effects of gravity [84]. This simplifies equation 3.2 to:

$$w = c_1 + c_2 \cdot r + c_3 \cdot \frac{a}{\sqrt{2}} + \text{higher orders}(r, \rho, \gamma). \tag{3.4}$$

The shape, u, of the deformation of the liquid surface, in the assumption of some nonzero conductivity of the liquid, is described by a differential equation:

$$\frac{\varepsilon\varepsilon_0\,U^2(x,y)}{2\,d^2} - (\rho g - k)u - \gamma\left(\frac{\partial^2 u}{\partial x^2} + \frac{\partial^2 u}{\partial y^2}\right) = 0, \tag{3.5}$$

with ε the dielectric constant of the gas filling the gap, U the electric potential, d the distance between the electrode and the liquid surface, ρ the density of the liquid, g the gravitational constant, k the electric constant ($k > 0$ for gels and $k = 0$ for liquids), and γ the surface tension of the liquid.

The geometry of the electrode defines the electric potential $U(x, y)$ and the distribution of the electric field [21]. This can be rewritten as:

$$U(x, y) = U \cdot S(x, y), \tag{3.6}$$

where U is the absolute value of the potential and $S(x, y) = [0, 1]$ a function describing the shape of the field. In an ideal case the potential and the field are both constant across the width of the electrode and negligible everywhere else.

3.4.0.1   The Tonks-Frenkel instability

Generally, the electrostatic force acting on the liquid surface will be constant across the size of the electrode (disregarding edge effects). However, small disturbances of the liquid surface, i.e. waves, may break the symmetry and lead to locally different effects, even if the electrostatic field is homogeneous: due to the smaller distance between the electrode and the wave crest a higher force acts on the crest than on the trough, which pulls the wave crest even closer to the electrode further increasing the force acting on it as shown in figure 3.7.

The condition for occurrence of the instability is given by:

$$E^2 > \frac{1}{\varepsilon_0} \left(\frac{1}{48} \rho g + \frac{\gamma}{\lambda^2} \right) d \equiv f(\lambda), \tag{3.7}$$

with E the electric field strength, ρ the density of the liquid, g the gravitational constant, λ the wavelength of the surface wave, and γ the surface tension of the liquid [85].

The qualitative shape of the neutral stability curve is shown in figure 3.8 where the parameter space below the curve corresponds to the stable regime.
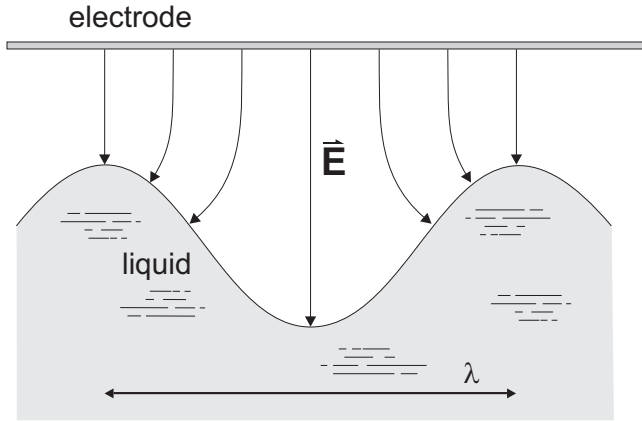
For small gaps with $d \ll \lambda$ the critical field strength, E_c, required for the occurrence of the Tonks-Frenkel instability is obtained for long wavelengths as $\lambda \to \infty$:

$$E_c^2 = \frac{d\rho g}{48\varepsilon_0}, \tag{3.8}$$

with the requirement that:

$$\lambda \gg \sqrt{\frac{48\gamma}{\rho g}} = \sqrt{24}\, a, \tag{3.9}$$

with a the capillary constant.

Figure 3.7: *Waves with a wavelength, λ, may disturb the liquid surface and lead to local differences in the distance between the liquid and the electrode. This leads to different forces caused by the electric field, $\vec{\mathbf{E}}$, acting on the liquid surface, which may cause the liquid mirror to become unstable.*

A more rigorous approach is followed in [86] and gives:

$$E_c^2 = \frac{d\rho g}{\varepsilon_0}. \tag{3.10}$$

The field is given by:

$$E = \frac{U}{d}, \tag{3.11}$$

where U is the voltage applied to the electrodes and d is the distance between electrode and the liquid surface, so that equation 3.10 can be rewritten as:

$$d_c = \sqrt[3]{\frac{\varepsilon_0 U^2}{\rho g}}. \tag{3.12}$$

The qualitative shape of the neutral stability curve as a function of voltage is shown in figure 3.9 where the parameter space above the curve corresponds to the stable regime.

For the aqueous solution of 80% glycerol with $\rho = 1208.5$ kg/m^3 and a maximum voltage of 400 V the critical distance is given by:

$$d_{c,\,\mathrm{gly}} \approx 490 \; \mu\mathrm{m}. \tag{3.13}$$
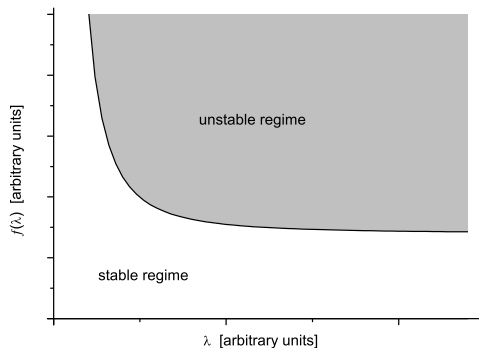
Figure 3.8: *Qualitative shape of the field strength neutral stability curve for the Tonks-Frenkel instability as a function of wavelength.*
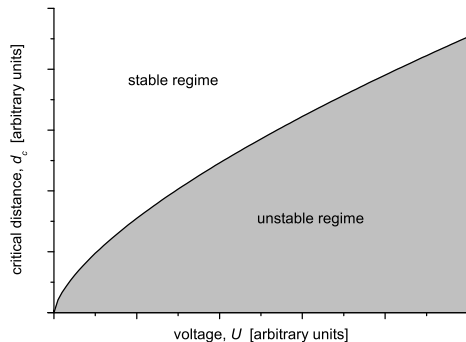
Figure 3.9: *Qualitative shape of the neutral stability curve in terms of the distance between electrode and liquid surface as a function of the voltage.*

3.4.1   The Electrode Structure

The geometry of the electrode structure is shown in figure 3.10. The electrode structure was obtained from a standard 37-channel MMDM ("OKO mirror") from OKO Technologies, which consists of 37 hexagonal electrodes with a center-to-center distance between electrodes of 1.8 mm arranged in a hexagonal geometry [2]. The electrodes have a via in the center with a sub-mm diameter that is not shown in the figure.
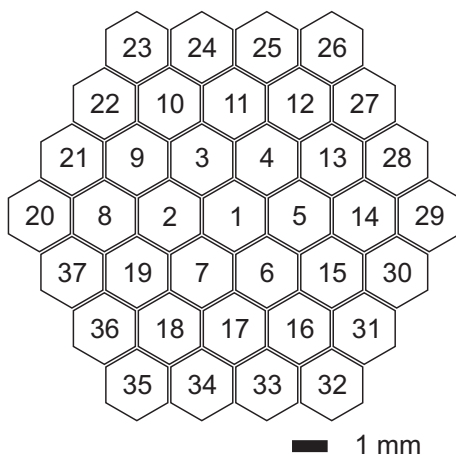
Figure 3.10: *The liquid mirror electrode structure.*

3.4.2   Simulations

For the calculation of the influence function the shape of the electrode was simplified to a circle with an effective radius of $r_{\text{eff}} = 0.87$ mm. The electric field of an electrode was calculated for different values of the gap between the electrode and the liquid surface. Figure 3.11 (top) shows the electric field created by the electrode structure (figure 3.10), while figure 3.11 (bottom) shows the electric field created by point-like electrodes with a radius of $r = 50$ μm. A voltage of $U = 300$ V was applied to the central electrode in each case, while all other electrodes and the liquid surface were at ground potential. The grid-spacing of the electrodes corresponded to the OKO electrode structure of 1.8 mm and was equivalent for both cases.

The corresponding potentials at the liquid surface are shown in figures 3.12 and 3.13.

Figures 3.14 and 3.15 show the change of the electric field shape as a function of the gap size: the peak values of the electric field, E_{max}, (figure 3.14) and the full width at half maximum (FWHM) of the electric field at the liquid surface relative to the size of the electrode, w_{rel} (figure 3.15). While there is only a small difference for large gap sizes between the peak values of the electric field for both geometries, the behavior of the width of the field at the liquid surface differs significantly. The results show that for the electrode structure shown in figure 3.10 with a single actuator at a potential U, the width of the electric field is almost independent of the distance between electrode and liquid surface, since the electrodes at ground potential surrounding the electrode prevent field fringing. The point electrode, where the surrounding electrodes at ground potential are much further away, induces an electric field strongly varying with the distance between the electrode and the liquid surface as the field strongly fringes.

The value of the electric field is given by:

$$E = \frac{\Delta\phi}{d}, \tag{3.14}$$

with E the value of the electric field, $\Delta\phi$ the potential difference, and d the gap size [87].

For the electrode structure the maximum value of the electric field, E_{max}, follows the theoretical curve of equation 3.14 almost perfectly, while the peak value of the electric field created by the point electrode drops below the expected values for large gap sizes caused by the fringing of the electric field, as shown in figure 3.16. The geometry of the electrode structure above the liquid surface strongly resembles the geometry of a parallel plate capacitor (illustrated in figure 3.17), for which the phenomenon of field fringing has been well documented [88–90]. As the
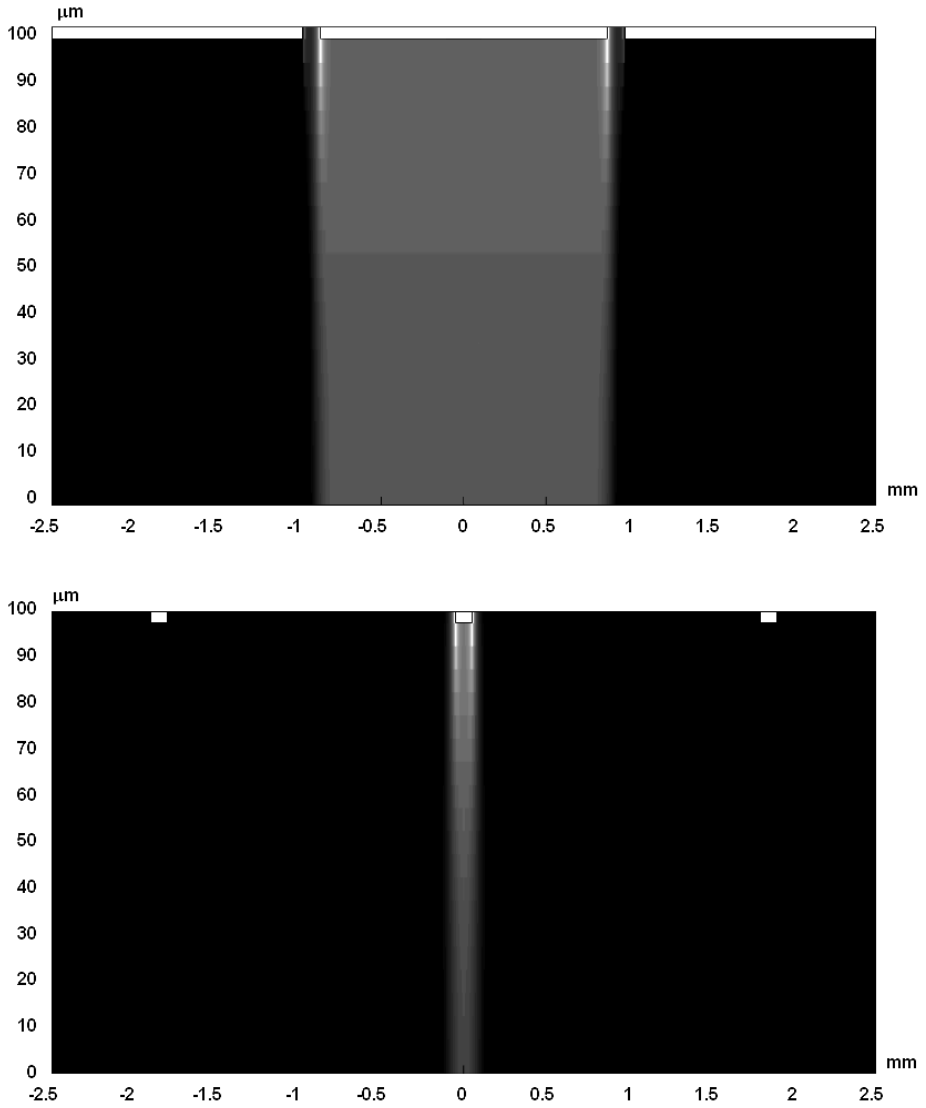
Figure 3.11: *Shape of the electric field created by an activated electrode of the electrode structure (figure 3.10) (top) and for a point-like electrode (bottom) at a voltage of $U = 300$ V with the surrounding electrodes and the liquid surface at ground potential. The electrodes are shown in white at the top, the distance between electrodes and liquid surface was $d = 100$ μm.*
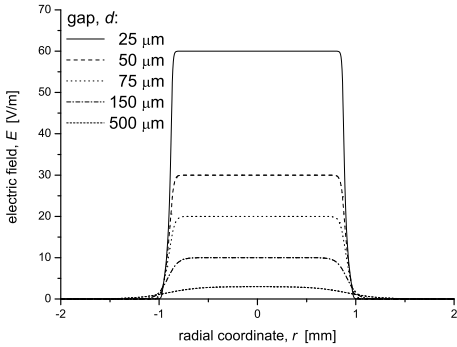
Figure 3.12: *Electric field strength at the liquid surface for a single activated electrode of the electrode structure (figure 3.10) for different gap sizes between the electrode and the liquid surface.*
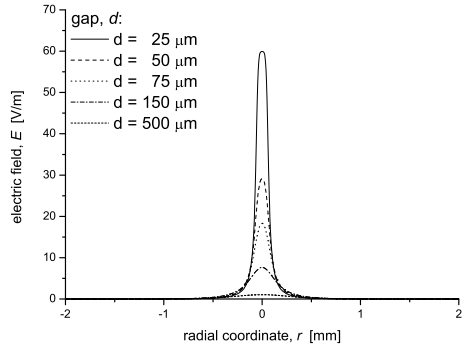
Figure 3.13: *Electric field strength at the liquid surface for a point-like electrode for different gap sizes.*

fringing occurs at the edges of the electrodes, the effect is much more pronounced for smaller electrodes than for larger electrodes and is reduced for electrodes that are closely surrounded by electrodes at ground potential. This is especially highlighted by the increase of the width of the field with larger gap sizes for the point electrode in figures 3.13 and 3.15. As the distance between electrode and liquid surface increases, the confinement of the electric field weakens and the field increasingly fans out to the sides.

This shows that the electric field for the electrode structure is practically constant across the area of the electrode and thus allows the shape function of the field, $S(x, y)$ of equation 3.6, to be simplified to a step function of unity inside the electrode radius, r_e, and zero outside:

$$S(r) = \left\{ \begin{array}{ll} 1 & \text{if } r \leq r_e \\ 0 & \text{if } r > r_e \end{array} \right. . \tag{3.15}$$

With this shape function equation (3.5) was numerically solved. A typical result is shown in figure 3.18 for a potential of $U = 300\,\text{V}$, an actuator radius of $r = 0.87\,\text{mm}$, and a gap size of $d = 75\,\mu\text{m}$.

Extensive simulations of the shape of the liquid deformation with different parameters were performed. The variable parameters of equation 3.5 are: the potential, U, the gap size, d, the density of the liquid, ρ, and the surface tension of the liquid, γ. Through equations 3.6 and 3.15 the shape of the deformation also depends on the radius of the electrode, r_e. Since the solution depends only on the ratio of
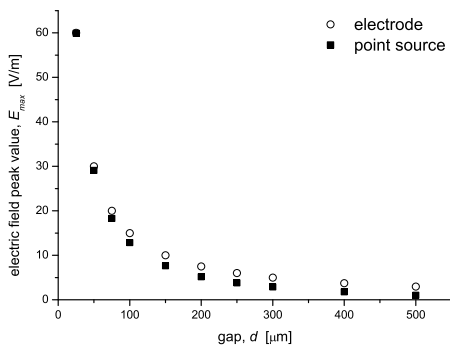
Figure 3.14: *Peak value of the electric field at the liquid surface as a function of the the gap size for the different electrode geometries.*
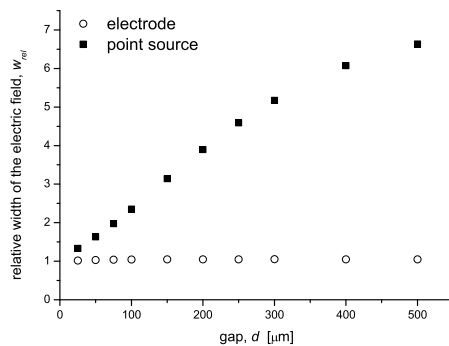
**Figure 3.15:** *FWHM of the field at the liquid surface as a function of the gap size for the different electrode geometries.*
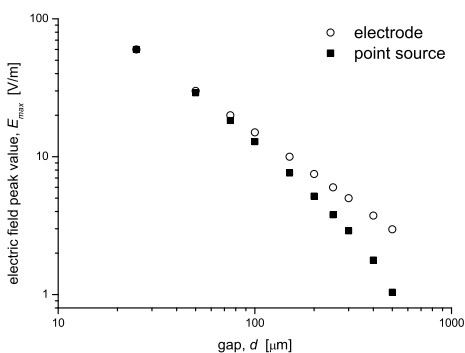
Figure 3.16: *Comparison of the influence of the gap size on the peak value of the electric field at the liquid surface for the different electrode geometries.*
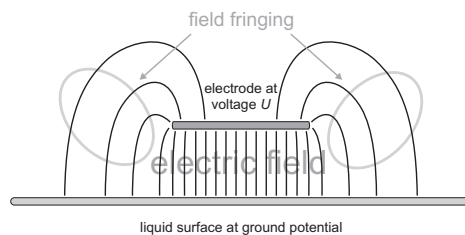
Figure 3.17: *Field fringing occurs at the edges of the parallel plates of a capacitor, or in this case, an electrode.*
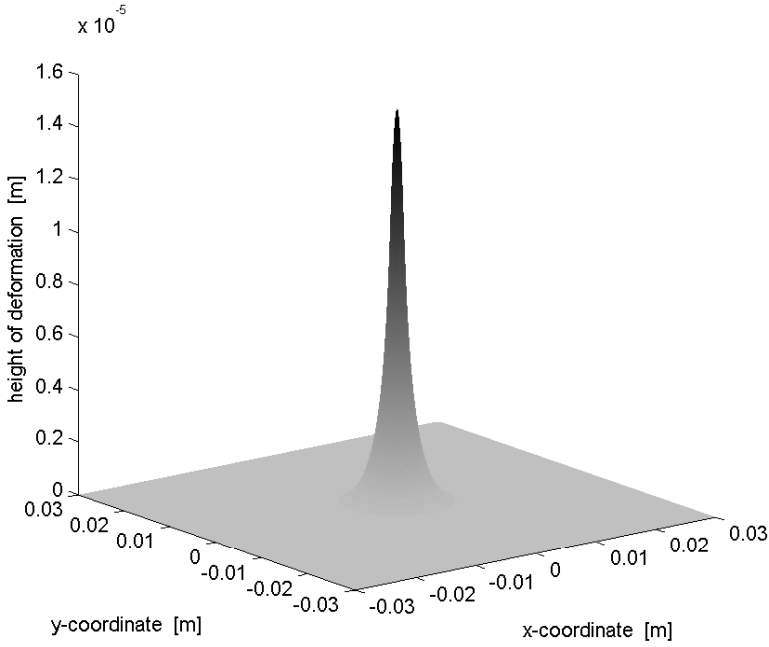
Figure 3.18: *Example of a simulated shape of the deformation of the liquid surface induced by the electrode structure at a distance of 75 μm.*

potential and gap size, the value of the potential was kept constant and only the distance was varied without loss of generality.

In order to verify the influence of the shape of the electric field on the shape of the liquid deformation the influence function was computed for the electrode and point source geometries. Equation 3.15 was used for the shape of the electric field of the electrode while the field of the point source was approximated with a third order function of the field radius. Figure 3.19 shows the width of the liquid deformation as a function of the gap size for both the electrode structure and the point source while all other parameters were kept constant. The result shows clearly that for a constant width of the electric field the width of the liquid deformation is also constant (as for the electrode structure), while when the width of the electric field varies, the width of the liquid deformation varies also (as for the point source).

This implies that for the simulation of the width of the liquid deformation, the gap size could be kept constant.

Thus, for the simulations the potential and the gap size were kept constant at $U = 300$ V and $d = 100\,\mu$m, while all other parameters were varied around the physical properties of the electrode structure and liquid, viz. an aqueous solution of 80 % glycerol, used in the experiments. The values of the parameters are summarized in table 3.2.

The results of the simulations are summarized in figures 3.20 to 3.23 and show the dependency of the influence function of the liquid mirror, i.e. the width of the liquid deformation, on the physical properties of the liquid and the setup (the fitting error of the system depends on the influence function, see section 2.2.2.1). The gradients of the width with respect to the different parameters are summarized in table 3.3. The results show that the radius of the electrode has the largest influence on the width of the liquid deformation as each increase in the electrode radius leads to an almost equal increase in the radius of the liquid deformation. The change in the width of the liquid deformation depends almost linearly on the changes of the electrode radius and the density of the liquid while the gradient with respect to the surface tension is only an average value due to the nonlinear connection between liquid deformation width and surface tension, which is already indicated by equation 3.5.

The deformation of the liquid, u, is mainly determined by the magnitude of the electric field at the liquid surface, which is dominated by the values of the applied potential, U, and the gap size, d. As the amplitude is a function of the ratio of potential and gap size, the potential was kept constant while the gap size was modified.

The maximum deformation can be derived from equation 3.5 by setting the partial derivatives to zero, so that:

$$u_{\max} = \frac{\varepsilon\varepsilon_0\,U^2}{2\,d^2\,(\rho g - k)}, \qquad (3.16)$$

with ε the dielectric constant of the gas filling the gap, U the electric potential, d the distance between the electrode and the liquid surface, ρ the density of the liquid, g the gravitational constant, and k the elastic constant [21].

The shape and maximum deformation of the liquid as a function of the gap size are shown in figures 3.24 and 3.25, with $U = 300$ V, $\rho = 1208.5\,\text{kg/m}^3$, $r = 0.87$ mm, and $\gamma = 65.7\,\text{mN/m}$.

Of course, the maximum deformation of about 1.5 mm shown in figure 3.25 can never be realized, since in that case the gap size is $d = 50\,\mu$m and most of the liquid deformation would be well inside the electrode. While the precise value of the maximum deformation also depends on the properties of the liquid and

| parameter	minimum	value from experiment	maximum	units
density, ρ	800	1208.5	1600	[kg/m^3]
surface tension, γ	1	65.7	100	[mN/m]
electrode radius, r_e	0.6	0.87	1.2	[mm]

Table 3.2: *Parameter space of the performed simulations for the variables liquid density, ρ, liquid surface tension, γ, and electrode radius, r_e.*
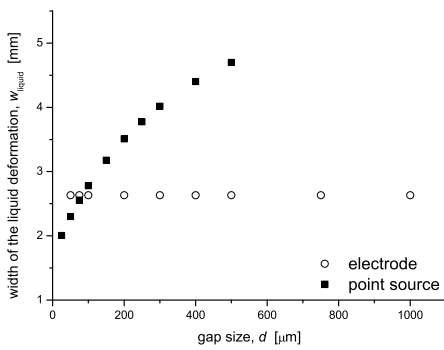
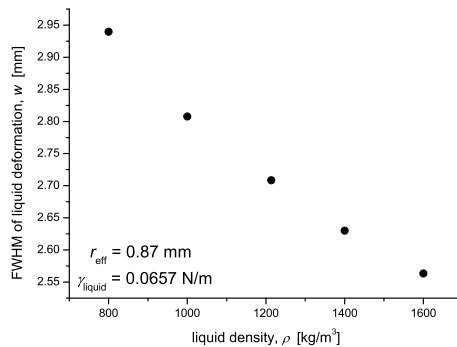**Figure 3.19:** *The width of the liquid deformation (FWHM) as a function of the gap size for the different electrode geometries.*
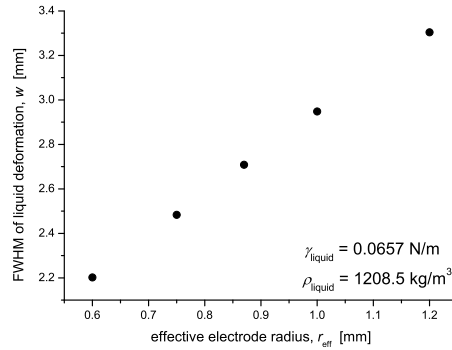
Figure 3.20: *Width of the liquid deformation as a function of the actuator radius.*
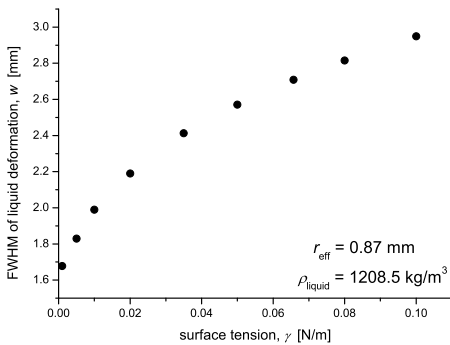
Figure 3.21: *Width of the liquid deformation as a function of the surface tension of the liquid.*

Figure 3.22: *Width of the liquid deformation as a function of the density of the liquid.*
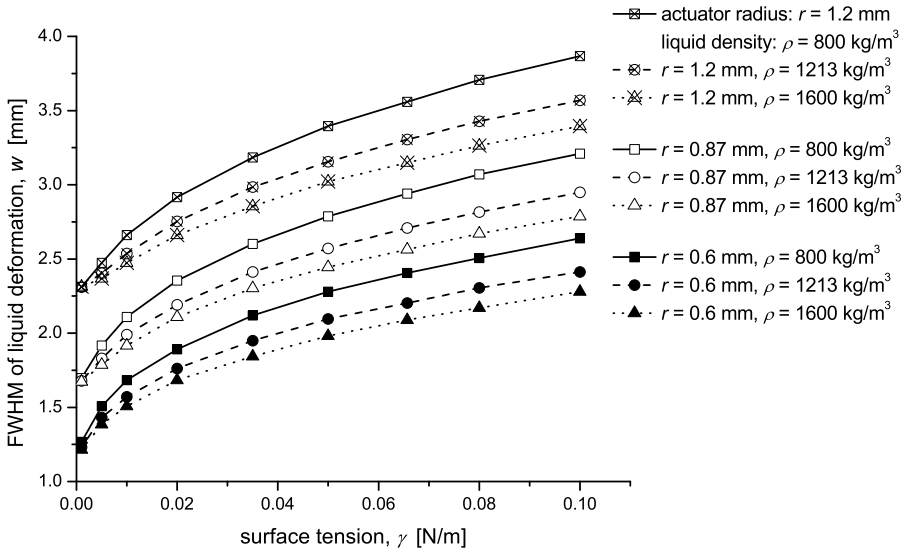
Figure 3.23: *Simulation of the width of the deformation of the liquid surface as a function of the physical properties of liquid and electrode.*
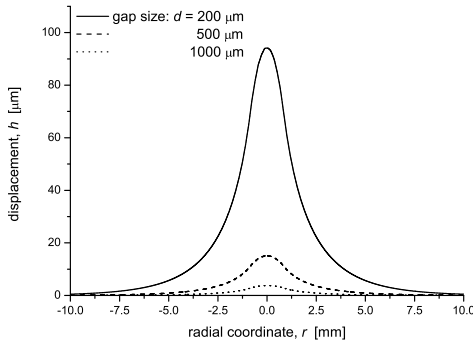
Figure 3.24: *Calculated shape of the liquid deformation for different gap sizes.*
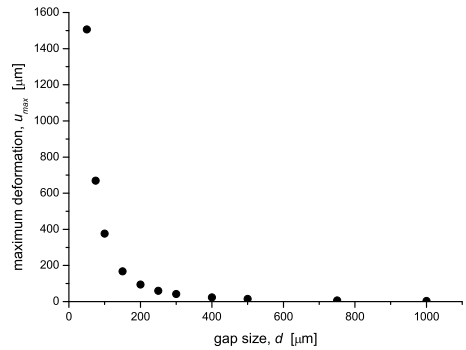
Figure 3.25: *Simulation of the amplitude of the deformation of the liquid surface as a function of the gap size – the curve shows a perfect $1/d^2$ behavior.*

parameter	gradient	value	units
density, ρ	$\partial w/\partial \rho$	$-4.66 \cdot 10^{-4}$	$\left[\frac{\text{mm}}{\text{kg/m}^3}\right]$
surface tension, γ	$\partial w/\partial \gamma$	$1.24 \cdot 10^{-2}$	$\left[\frac{\text{mm}}{\text{mN/m}}\right]$
electrode radius, r_e	$\partial w/\partial r_\text{e}$	1.84	$\left[\frac{\text{mm}}{\text{mm}}\right]$

Table 3.3: *Gradients of the width of the liquid deformation with respect to the parameters of the setup.*

the potential, it is dominated by the inverse function of the gap size, so that the maximum deformation of figure 3.25 can be fitted with the function:

$$u_\text{max} = 3.77 \cdot 10^{-12} \cdot d^{-2}, \tag{3.17}$$

where the constant has the units of $[m^3]$, so that both the amplitude, u_{max}, and the gap size, d, are given in meters.

The maximum possible deformation of the liquid, u_{max}, is thus given when the deformation is equal to the gap size:

$$u_\text{max} = \sqrt[3]{3.77 \cdot 10^{-12}}, \tag{3.18}$$

so that $u_{max} \approx 155\,\mu$m as shown in figure 3.26.

By equating the right sides of equations 3.16 and 3.17 the effective voltage at the liquid surface can be computed: $U_\text{eff} \approx 100\,\text{V}$, which is only about a third of the nominal value.
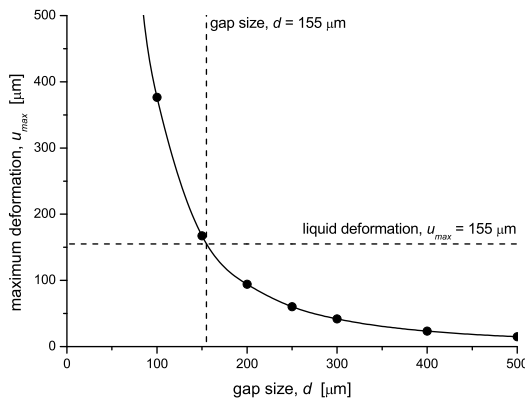
Figure 3.26: *The maximum amplitude is given when the amplitude equals the gap size.*

3.4.3 Measurements

The shape of the liquid deformation was measured by positioning the electrode structure shown in figure 3.10 above the liquid mirror of figure 3.1 and applying a voltage of $U = 300\,\mathrm{V}$ to a single electrode while the metal container remained at ground potential. The electrode structure was mounted on a manual linear stage in such a way that the electrode was oriented in parallel to the liquid surface and the distance between the electrode and the liquid surface could be adjusted with micrometer precision. The shape of the deformation was measured interferometrically with high accuracy.

3.4.3.1 Setup

Figure 3.27 shows the interferometer used to observe the deformation of the liquid surface. It includes the liquid mirror based on total internal reflection with the electrode structure positioned above the liquid surface (figures 3.1 and 3.10). A collimated laser beam is split into two paths, one of which is coupled into the liquid container. The light enters the metal container through the coupling prism in the bottom of the container and is subsequently reflected by the liquid surface by total internal reflection and coupled out of the container by way of the same coupling prism. The beams are then recombined to form an interferogram displaying the shape of the liquid surface.

The setup was simulated with the optical design software Zemax. Figure 3.28 shows the setup in the non-sequential mode of Zemax. A simulation of the interference pattern of the beam for different tilts of the liquid mirror is shown in figure 3.29.

The liquid surface is flat when the electrodes are at ground potential (figures 3.30 and 3.31, left), while an applied voltage induces an electrostatic field and a surface deformation (figure 3.30 and 3.31, right). A simulation of a deformed liquid surface is shown in figure 3.32.
The amplitude and width of the deformation can be determined with high resolution from the interferograms.

3.4.3.2 The Profile of the Liquid Deformation

Figure 3.33 shows the measured and calculated profiles of the liquid deformation for different values of the gap size. Except for variations in the amplitude (see also figure 3.36) the curves show a good agreement. However, figure 3.34 shows curves that were normalized in order to eliminate the variations in amplitude and reveals that the curves do not exactly match: while the widths of the simulation and the measurement correspond at about half the maximum (FWHM), the width of the measured deformation is smaller at both the peak and the foot of the deformation. This may be a result of the vias in the electrodes that effect the shape of the static electric field.
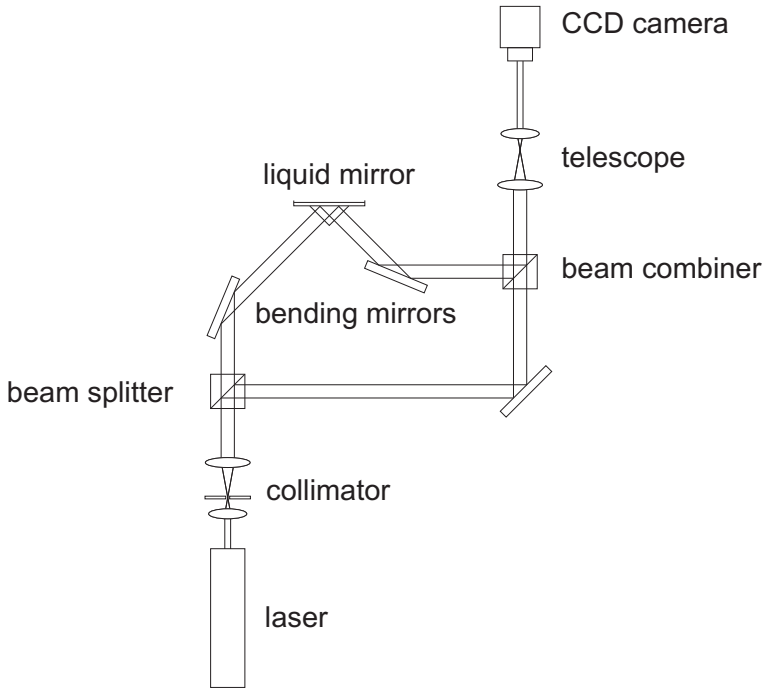
Figure 3.27: *Experimental setup for measuring the deformation of the electrostatically deformed liquid surface.*
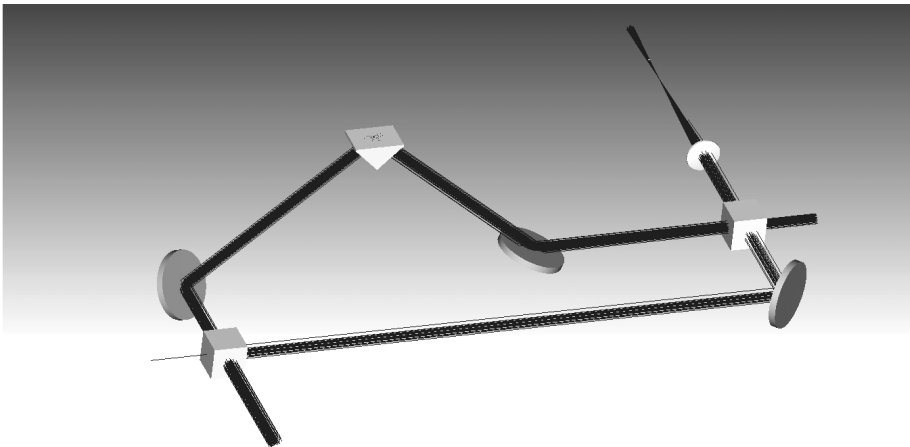
Figure 3.28: *Non-sequential mode Zemax model of the liquid mirror interferometer setup.*
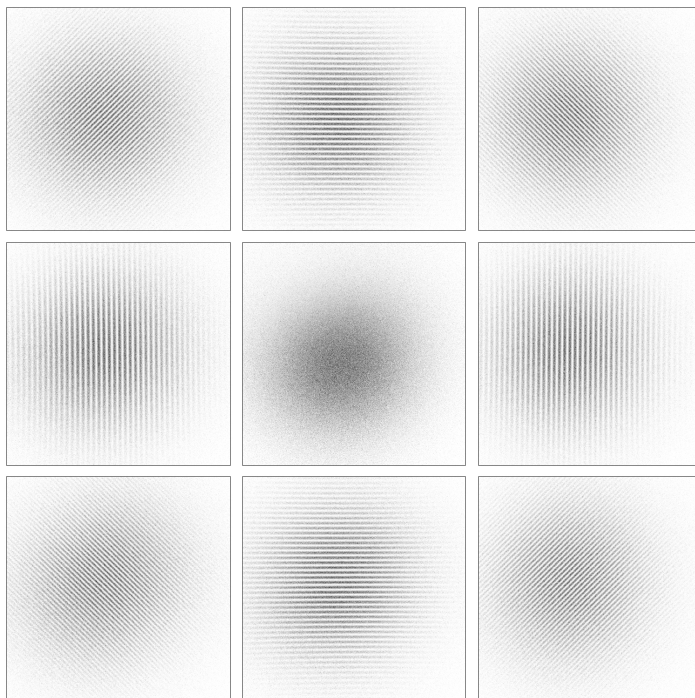
Figure 3.29: *Simulated interference patterns for different tilts of the liquid mirror: no tilt for the center beam, 0.7 mrad for the up, down, left, and right displaced beams, and 1 mrad for the corner beams.*

The measured deformation profiles were fitted with a Lorentzian curve to calculate the width of the deformation. Figure 3.35 shows the width of the deformation (FWHM) as a function of the gap size. Although the measured values are relatively constant, the average value differs from the result of the simulation.

The maximum value of the measured deformation as a function of the gap size is shown in figure 3.36. For the freshly applied glycerol ($t = 0\,\mathrm{h}$) the measurement shows a good correspondence to the simulation, while the measured maxima decrease with time ($t = 1\,\mathrm{h}15$ and $3\,\mathrm{h}$).
Fitting the different curves with a $1/d^2-$function allows to calculate the effective voltage drops for the different curves, which are summarized in table 3.4.

This leads to the supposition that the surface tension of the liquid changes with time, as the system was not changed between measurements. It is known that the contamination of the liquid surface with dust and other surfactants may reduce the surface tension by an amount that increases with the concentration of the
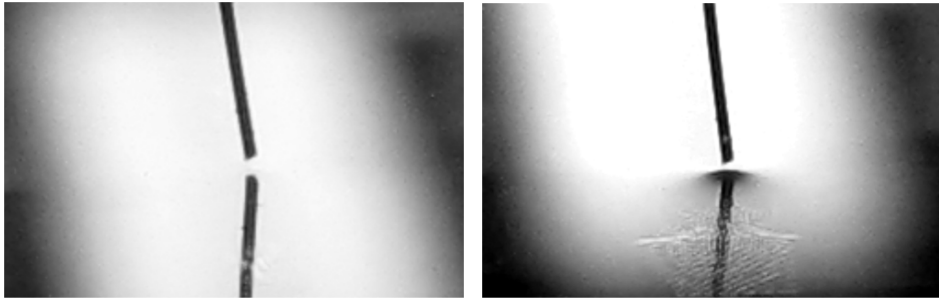
Figure 3.30: *A wire functioning as electrode positioned above the liquid surface without applied voltage (left) and with an applied electrostatic field (right). The wire has a diameter of about* $200\,\mu$m *and induces a deformation with a diameter of* $>\;2\,$mm.
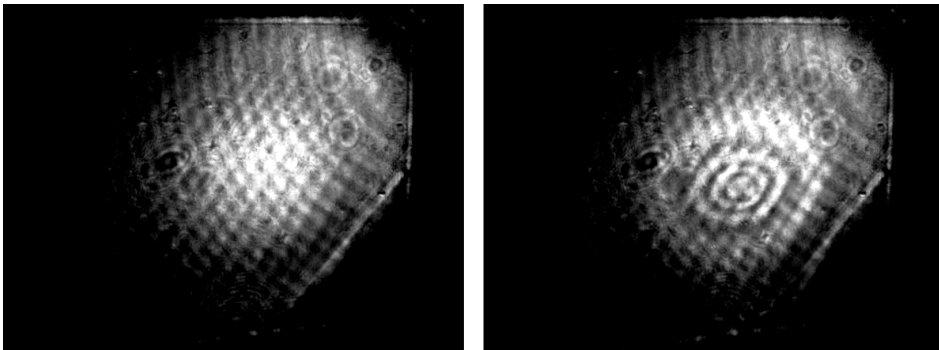
Figure 3.31: *Interferogram of the undisturbed liquid surface (left) and with an electrostatically induced deformation (right).*
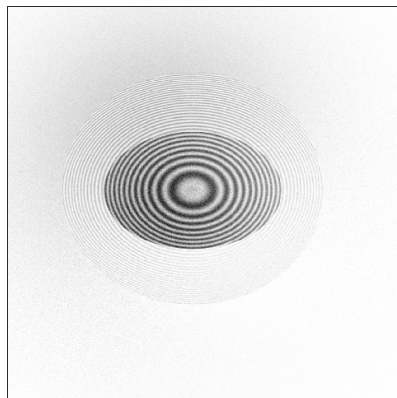
Figure 3.32: *Simulated far-field beam and interference pattern for an electrostatically deformed liquid surface. The deformation had a diameter of* $4\,mm$ *and an amplitude of* $10\,\mu m$.
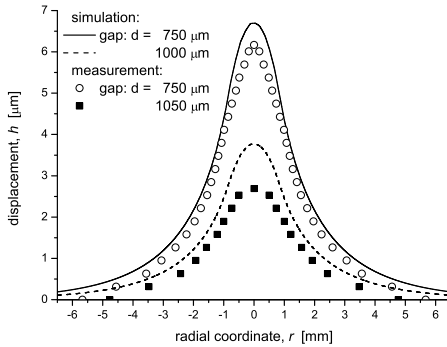
Figure 3.33: *Comparison of the calculated and measured shapes of the liquid deformation for different gap sizes.*
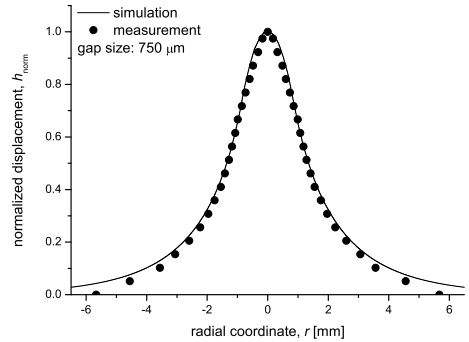
Figure 3.34: *Comparison of normalized simulated and measured shapes of the liquid deformation.*
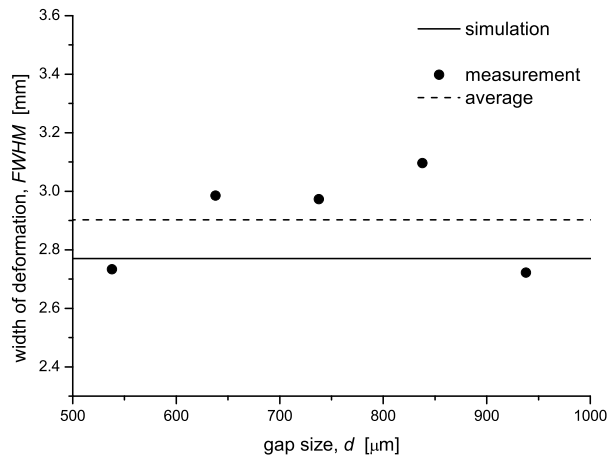
Figure 3.35: *Comparison of the simulated and measured width (FWHM) of the deformation of the liquid surface as a function of gap size.*

time	effective voltage, U_{eff} [V]	surface tension, γ [N/m]
0 h	97.0	0.0652
1 h 15	80.1	0.0497
3 h	70.2	0.0286

Table 3.4: *Effective voltage drops over the liquid surface derived from fitted curves to the data shown in figure 3.36; the surface tension values were taken from [83].*
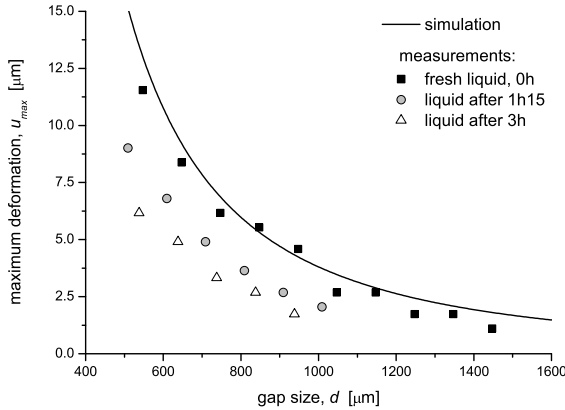
Figure 3.36: *Comparison of the simulated and measured amplitudes of the deformation of the liquid surface as a function of gap size and the age of the liquid.*

contamination. When the liquid surface is formed with fresh liquid, the surface tension may be close to the nominal value, but it can drop quickly to about half that value [91], as indicated by figure 3.36. This may also effect the shape of the liquid deformation as shown in figure 3.33, so that the difference between measurement and simulation is a result of the interaction of both the via in the electrode and the change in surface tension.

This effect implicates that contrary to equation 3.16, $u_{\max}$ is also dependent on the surface tension, which again implies that both equations 3.5 and 3.16 are not complete and need to be modified to incorporate the effect described above.

3.4.4 Discussion

In this section the deformation of a liquid surface through an electrostatic field was investigated. The different forces acting on the liquid surface were described in equation 3.1 and the effect of the shape of the electrode on the static electric field was investigated and shown in figures 3.11 to 3.16. The partial differential equation 3.5 describing the shape of the liquid deformation as a function of the electrostatic field was solved for different physical properties of the liquid and compared to measured values. The width of the deformation, which is linked to the formfactor of section 2.2.2.1, on which the fitting error of an Adaptive Optics system depends, was found to be about 3 mm. Furthermore, the maximum of the liquid deformation was investigated: it was shown that the theoretical and experimental values are in good agreement for the fresh liquid, but that the maximum values decrease with time. This can be attributed to a decrease of the surface tension due to contamination of the liquid surface with surfactants.

This effect implies that both equations 3.5 and 3.16 are incomplete and need to be modified to incorporate the described effect.

These findings also have implications for the results presented earlier [83] as the same imperfect partial differential equation was used for the derivation of a novel method to measure surface tension. It was shown that the experimentally measured values for the full width at half maximum (FWHM) are independent of the gap size, which was the basis of the method in [83]. However, a calibration of the measured results was needed to compute the correct surface tension, since the derivation was based on a numerical solution of equation 3.5 in its current form. It is expected that the calibration is no longer necessary when the corrected equation 3.5 is used for the derivation. Furthermore, the work presented here also confirms the observed decrease in surface tension through the contamination of the liquid surface through surfactants and thus confirms the findings presented in [83].

3.5   Liquid Dynamics

The flexibility of a liquid allows to locally shape its surface in such a way that it performs a certain function, i.e. in this case to correct a distorted wavefront. At the same time this flexibility implies that the liquid surface may be shaped by other influences that are not controlled by the system. Even though the overall movement of the liquid is limited by the container, macroscopic surface motion may be excited.

The phenomenon of a liquid in motion in a closed container is called "sloshing" and ranges from the motion of a beverage in a cup or glass carried by a person to the large scale oscillatory movement of water in a harbor or lake. The term "sloshing" itself refers to the motion of the liquid in the closed container and implicitly presumes the existence of a free liquid surface in the container, although the research field "sloshing" also includes the influence of spinning fuel in completely filled tanks that may effect the motion of for example rockets or tanker trucks.

Large scale research interest in this topic was initiated by the increase in size of the liquid fuel containers of spacecraft in the early sixties (see for example [92–94]). Generally, it is assumed that the motion of the liquid is induced by the movement of the container - however, the theory is no less applicable when the container is at rest and the free surface of the liquid is excited directly by a changing electrostatic field or indirectly by ambient vibrations as in the case of the liquid mirror.

The shape and properties of container and liquid determine the characteristics of the allowed dynamics, i.e. the allowed normal modes of the system.

The characteristic modes form a spectrum that exhibits resonances at certain frequencies that may be excited by ambient vibrations or by the working system itself. For an application with the stated goal of reducing distortions – in this case of an optical wavefront – it is thus essential to know about the position and strength of these resonances in order to avoid interference with the regular operation of the device.

3.5.1   Theory of the Liquid Surface in Motion

Here, the container consists of an open cylinder with smooth walls, for which the normal modes are given by:

$$\omega_{ij}^2 = \frac{g\,\xi_{ij}}{R}\left(1 + \frac{\gamma\,\xi_{ij}^2}{\rho\,g\,R^2}\right)\tanh\left(\frac{\xi_{ij}\,h}{R}\right),\tag{3.19}$$

with R the radius of the liquid container, g the gravitational constant, γ the surface tension, ρ the density of the liquid, h the fluid depth, and ξ_{ij}/R the roots of the Bessel function $\partial J_i(\xi_{ij}\,r/R)/\partial r|_{r=R} = 0$ [95]. The values of these roots can be found in the literature [96].

The corresponding wavelengths, λ_{ij}, of the modes with frequency ω_{ij} can be derived from the dispersion relation:

$$\omega_{ij}^2 = g\,k_{ij} + \frac{\gamma\,k_{ij}^3}{\rho},\tag{3.20}$$

with g the gravitational constant, k_{ij} the wavenumber, γ the surface tension, and ρ the density of the liquid [84]. With $\lambda_{ij} = 2\,\pi/k_{ij}$ this can be rewritten as:

$$\omega_{ij}^2\,\lambda_{ij}^3 - 2\,\pi\,g\,\lambda_{ij}^2 = \frac{8\,\pi^3\,\gamma}{\rho}.\tag{3.21}$$

This is a cubic equation that can be shown to have one real root that corresponds to the wavelength, λ_{ij}, and two nonreal complex conjugate roots that will be ignored.

The wave-velocity of the modes is given by:

$$c = \frac{\omega \cdot \lambda}{2\,\pi},\tag{3.22}$$

with c the wave-velocity, ω the frequency, and λ the wavelength of the respective modes.

The frequency, wavelength, and wave-velocity of the first ten modes are summarized in table 3.5.

i j	frequency f [Hz]	wavelength λ [m]	wave-velocity c [m/s]
1 0	1. 207	1. 072	1. 294
0 0	2. 515	0. 248	0. 623
1 1	3. 505	0. 129	0. 451
0 1	4. 624	0. 075	0. 349
1 2	5. 643	0. 052	0. 296
0 2	6. 754	0. 039	0. 261
1 3	7. 808	0. 031	0. 240
0 3	8. 939	0. 025	0. 226
1 4	10. 036	0. 022	0. 218
0 4	11. 206	0. 019	0. 212

Table 3.5: *Frequency, f, wavelength, λ, and wave-velocity, c, of the first ten normal modes.*

After excitation these modes will be damped by a variety of effects, e.g. viscous dissipation and capillary hysteresis, at the surface and the container walls. The theory and description of this cannot always be matched very well to observations [97, 98]. Because of the complexity of the topic, certain assumptions have to be made, one of which requires the surface boundary layer, δ, to be much smaller than the liquid depth, h:

$$\delta = \sqrt{\frac{2\,\upsilon}{\omega}} \ll h, \tag{3.23}$$

with υ the kinematic viscosity of the liquid and ω the frequency of the wave [98]. In the case of the liquid mirror the boundary layer thickness for the strongest mode, ω_{01}, calculates with a kinematic viscosity of $\upsilon = 4.957 \cdot 10^{-5}$ m^2/s to $\delta_{01} = 1.8$ mm while the liquid depth is about $h = 4$ mm. This means the requirement is not met and applicability of the theory is limited. A more detailed analysis of this topic is beyond the scope of this thesis, for a detailed discussion see for example [95, 98–101] and references therein. A simple calculation for the damping time constant, τ, of an unbounded surface is given here as a first estimate:

$$\tau = \frac{\lambda^2}{8\,\pi^2\,\upsilon}, \tag{3.24}$$

with λ the wavelength and υ the kinematic viscosity of the liquid [99].

3.5.2   Open-loop Characterization of the Liquid Mirror Response

In the open-loop state no feedback is provided to the liquid mirror system, so that the response of the system to different input signals can be measured. From this response may be determined if and under which conditions the liquid mirror is a stable closed-loop control system.

3.5.2.1   Setup

Figure 3.37 shows the setup used to measure the open-loop frequency response and the time constants of the liquid mirror. The radius of the liquid container is about $R = 47.5$ mm and the depth about $d = 10$ mm with a liquid depth of about $h = 4$ mm. The liquid was an aqueous solution of 80% glycerin with a density of $\rho = 1208.5$ kg/m^3 and a surface tension of about $\gamma = 65.7$ mN/m for the fresh liquid. The electrode structure used to apply a voltage and generate a static electric field to control the shape of the surface is a standard OKO electrode for a 37-ch 15 mm MMDM mirror consisting of 37 hexagonally arranged electrodes with a diameter of 1.9 mm each and an overall diameter of 15 mm, one of which was controlled by a signal generator. The voltage applied was $U = 380$ V and the distance between the actuators and the liquid surface was about $L = 700\ \mu$m, which resulted in a maximum stroke of about 15 μm.

The light reflected from the liquid mirror was focused onto a knife-edge and subsequently detected by a fast photodiode. The signals from the photodiode and the signal generator were recorded with an oscilloscope.

From theory the frequency response is expected to follow the characteristic given by equation 3.19, i.e. a relatively flat response with peaks at the positions of the resonances $\omega_{i,j}$. However, imperfections in the shape of the liquid container, i.e. irregularities in the geometry of the wall and flatness of the bottom, may cause aberrations in the spectrum. The size of these imperfections is on the order of a few 100 μm leading to a broadening of the resonances of low frequency modes (large wavelengths) and to a shift of the resonances of higher frequency modes (short wavelengths).

A Bode plot and Nichol's chart showing the open-loop frequency response of the mirror are shown in figure 3.38. The measured voltages were normalized such that the DC gain of the system equals unity, i.e. $G_{\mathrm{DC}} = 1 = 0$ dB. It shows that the response of the glycerin solution is relatively flat up to a frequency of about 100 Hz, after which the amplitude drops rapidly. However, the resonances of table 3.5 cannot be distinguished. While the high frequency asymptote has a slope of about -40 dB/decade and thus suggests a second order system, there are a number of low-frequency peaks indicating an even higher order system (compare also figure 3.39). The bandwidth of the liquid mirror is about 80 Hz, which implies through equation 2.11 that the liquid mirror system will function
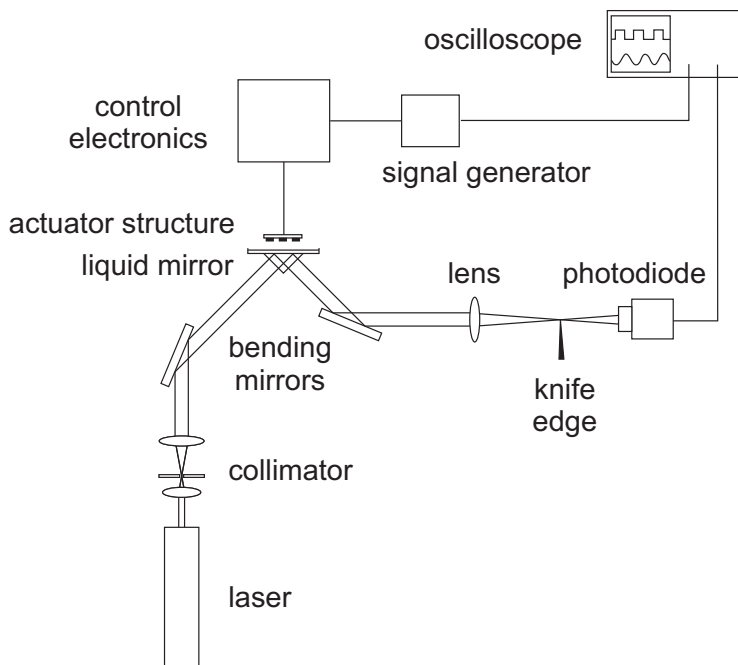
Figure 3.37: *Setup for the measurement of the frequency response and the time constants.*

reasonably up to a Greenwood frequency of about 14 Hz. The gain crossover frequency and the phase crossover frequency of the system are given by $f_{gc} = 27$ Hz and $f_{pc} = 115$ Hz, respectively, which leads to a gain margin of $GM = 11.4$ dB and a phase margin of $PM = 140°$. Thus, the stability criteria, $f_{gc} < f_{pc}$ and $G < 0$ at f_{pc}, are fulfilled and the system is stable [102]. The critical delay, for which the system becomes unstable is given by $\tau_c = 180/f_{pc} = 1.57$ s.

The open-loop response of the liquid mirror excited by ambient vibrations and a Fourier spectrum of the response are shown in figure 3.39. In the Fourier spectrum there are two wide peaks between 2.4 and 5.4 Hz and around 12 Hz each containing multiple broadened modes and a number of narrow peaks, most notably at 8.92 Hz, 21.7 Hz, and 42.5 Hz that can be attributed to excited modes. The corresponding measured and calculated frequencies are shown in table 3.6.

Here, the resonant behavior of the liquid system is clearly visible: ambient vibrations couple to the liquid layer and excite the liquid surface. The main part of the mechanical energy is coupled to the lowest modes between 2.5 and 5 Hz where $\omega_{01} = 4.62$ Hz is the main excited mode as its wavelength of $\lambda_{01} = 7.5$ cm matches the diameter of the liquid container the most closely.
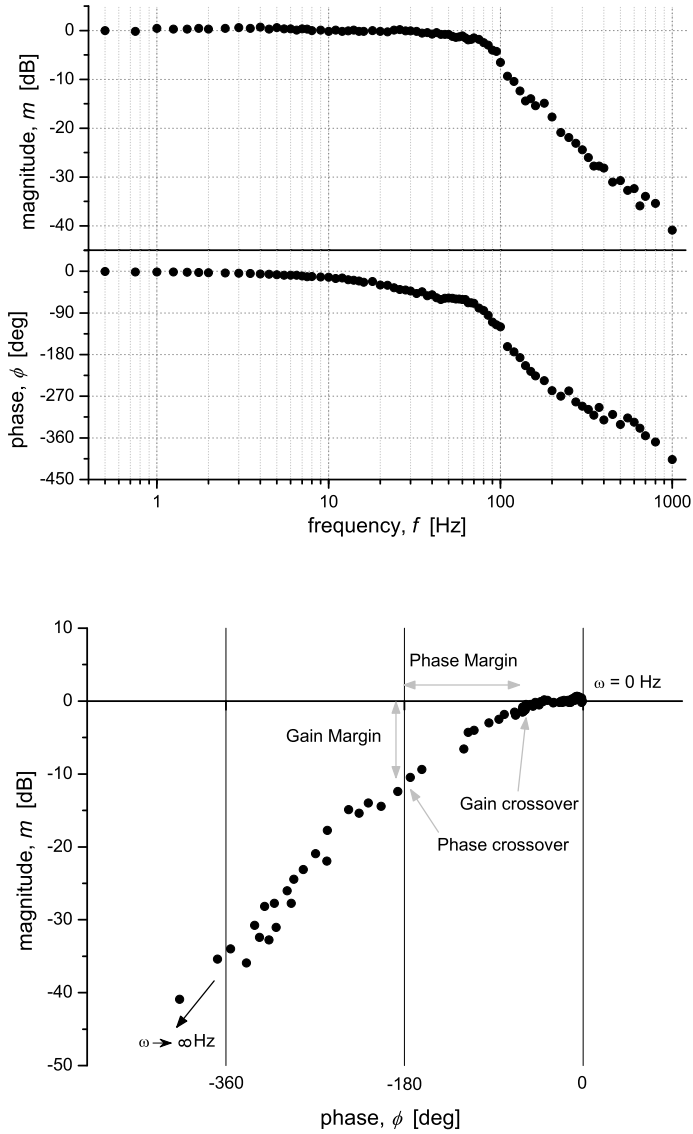
Figure 3.38: *Frequency response of the liquid mirror device, top: Bode plot, bottom: Nichol's chart.*
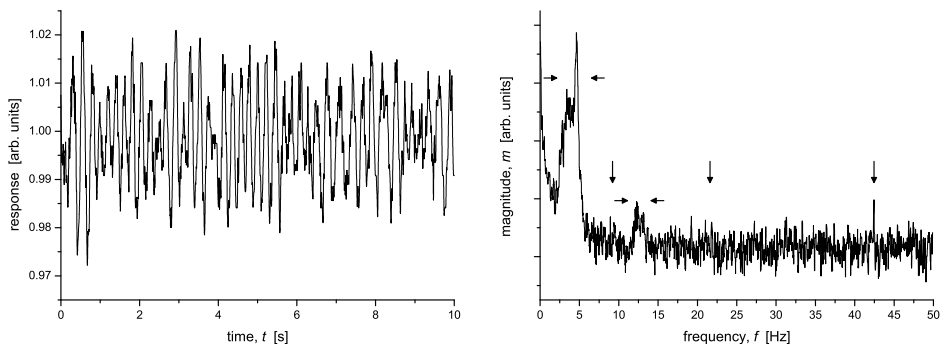
Figure 3.39: *Open-loop response of the liquid mirror to ambient excitations in the time domain (left) and as a Fourier spectrum in the frequency domain (right). The arrows point out the frequencies of the excited modes summarized in table 3.6.*

| measured frequency f_{meas} [Hz]	i j	calculated frequency f_{calc} [Hz]
2. 4		
	0 0	2. 52
	1 1	3. 51
	0 1	4. 62
5. 4		
8. 9	0 3	8. 94
11. 5		
	1 5	12. 02
	0 5	13. 58
13. 4		
21. 7	0 8	21. 42
42. 5	1 15	42. 56

Table 3.6: *Comparison of the measured, f_{meas}, and calculated, f_{calc}, resonances of the open-loop response of the liquid mirror system. The measured resonances are exhibited by the Fourier spectrum of the open-loop frequency response (figures 3.39 and 3.42).*

3.5.2.2   Time constants

The rise and relaxation times were defined as the times for the signal of the photo-diode to go from 10% to 90% of its final value. The rise- and relaxation-times for different numbers of actuators are shown in figure 3.40 (left). With the exception of the time constants for a single actuator the evolution of the time constants as a function of the number of actuators can be described by a function in the form of:

$$\tau = a * n^b, \tag{3.25}$$

with τ the rise- or relaxation-time constant of the liquid and n the number of actuators. For the pulling action the constants are $a_{\mathrm{pull}} = 4.22$ and $b_{\mathrm{pull}} = 1.13$ and for the release action of the liquid $a_{\mathrm{relax}} = 1.18$ and $b_{\mathrm{relax}} = 1.67$, respectively.
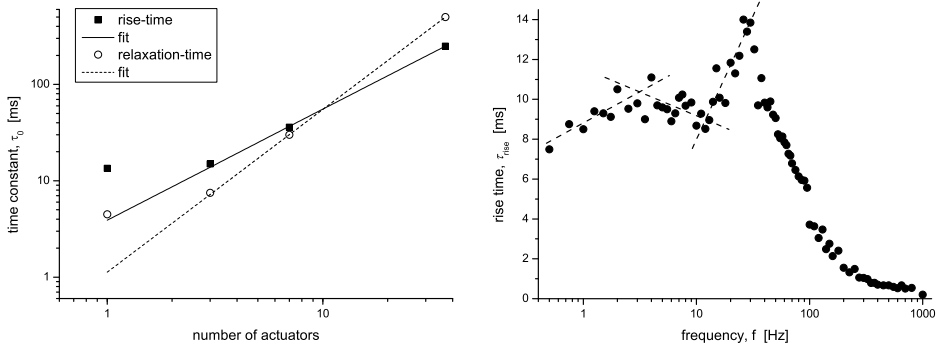
Figure 3.40: *Rise- and relaxation-time constants of the liquid mirror device as a function of the number of actuators (left) and the frequency (right).*

The rise-time as a function of the frequency is shown in figure 3.40 (right): the rise-time first increases to the main resonance of the system at 5 Hz (see figure 3.39), then decreases again to the point that the phase lag of the system starts to increase significantly at about 15 Hz (see figure 3.38), and finally increases again to the maximum rise time at about 30 Hz, after which the accumulated phase lag prevents the signal from reaching its maximum value.

3.5.3   Damping and Closed-Loop Mirror Characterization

The damping of the excited liquid layer as response to a mechanical impulse is shown in figure 3.41.

The shape of the envelope following the decay of the amplitude as a consequence of the damping can be described by an exponential function where the damping time, τ, is defined as the time needed for the amplitude to drop to half of its original value. For an aqueous solution of glycerol with a kinematic viscosity of about $\nu = 5.23 \cdot 10^{-5}$ m^2/s [103] equation 3.24 predicts for the prominent 01-mode with a wavelength of $\lambda = 0.075$ m a damping time of $\tau_{\text{theory}} = 1.36$ s.

The damping times for the system were measured for the free surface as $\tau_{\text{free}} = 1.27 \pm 0.11$ s and for the closed-loop system as $\tau_{\text{fb}} = 1.10 \pm 0.11$ s.

The reduction of the excited modes through the damping of the system is also evident through comparison of the Fourier spectra of the open-loop and the closed-loop response of the system to ambient excitation: figure 3.42 shows the open-loop spectrum of figure 3.39 overlaid with the closed-loop spectrum up to 15 Hz together with the excited modes from table 3.6. The magnitude of the excitation is reduced over the entire spectrum and the excited modes, especially the symmetric modes ω_{0i}, are significantly damped.

The difference between the theoretical and experimental damping times is most

likely due to the flaws of the liquid container that lead to additional damping. Moreover, the surfactants that have been observed to influence the surface tension of the liquid (see section 3.4.3) may also effect the damping. Nonetheless, the feedback system was able to reduce the damping time by an additional 14%. However, the possibility of external excitation of the liquid surface is still substantial and has to be considered together with the large damping time when the liquid mirror is used in an adaptive optical setup (see chapter 4).

One possibility to eliminate outside disturbances and reduce the noise in the measurements is to mechanically decouple the setup from its surroundings, e.g. by using a vibration isolation optical table. However, a more promising method is to design the system in such a way that it is insensitive to ambient vibrations or at least increase the damping such that excitations die out very quickly. This can be realized by scaling the dimensions of the liquid system in such a way that the coupling to the normal modes is reduced and the damping is increased; the implementation of such a liquid micro mirror is described in chapter 5.

3.5.4 Discussion

The open-loop frequency response and the time constants of the liquid mirror were measured. The Bode plot and Fourier spectrum of the open-loop liquid mirror response show that the liquid mirror system is a higher order transfer function with the symmetric 01-mode at 4.6 Hz as the main resonance in accordance with the prediction by sloshing theory. Both the gain margin, $GM = 11.4$ dB, and the phase margin, $PM = 140\,^\circ$, predict that the system is stable, thus allowing the use of the liquid mirror in a closed-loop AO system (see chapter 4).
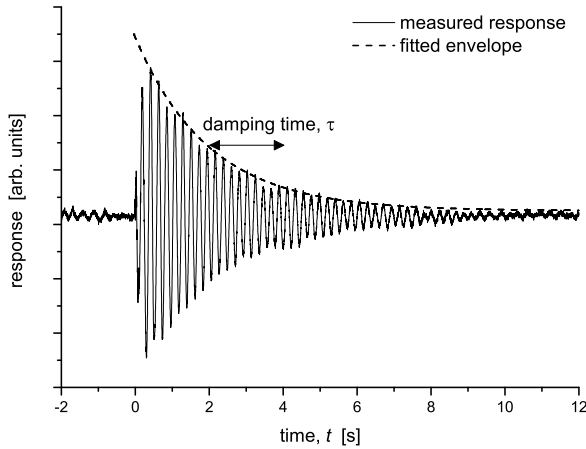
Figure 3.41: *Response of the free liquid surface to a mechanical impulse to the setup.*
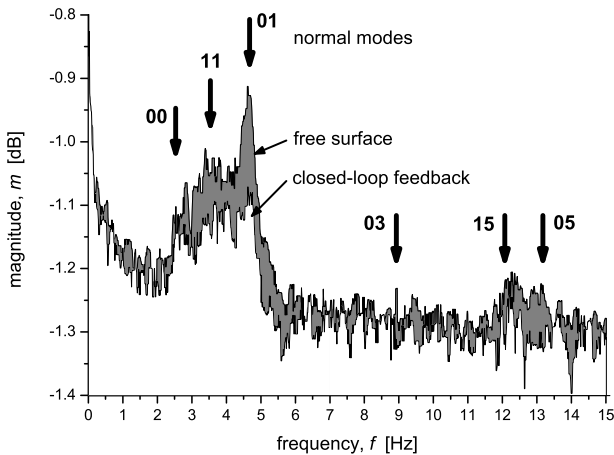
Figure 3.42: *Fourier spectra of the liquid mirror response with a free surface (open-loop) and with closed-loop operation of the system. The arrows show the positions of the normal modes of the liquid container (compare table 3.6).*

The time constants of the liquid mirror increase with the number of actuators, n, since increasingly more liquid has to be displaced.
Excitations of the liquid surface mainly couple to main mode and then decay with a characteristic damping time of $\tau_{\text{free}} = 1.27$ s, which agrees well with the predicted value of $\tau_{\text{theory}} = 1.36$ s. Activating the feedback of the system increases the damping, so that the characteristic damping time is reduced to $\tau_{\text{fb}} = 1.10$ s.

Since both the frequency response and the time constants depend both on the geometry of the liquid container and the material properties of the liquid, it is possible to tune the characteristics of the system in order to optimize the performance of the mirror (see also chapter 5). The resonant behavior of the system is mainly determined by the radius of the dish and the depth of the liquid. Here, a smaller dish will increase the resonant frequencies (equation 3.19), which will make it more difficult for the low frequency ambient vibrations (e.g. building vibrations) to couple to the liquid mirror. Also, a smaller liquid depth will increase the damping (equation 3.23) and thus enhance the dissipation of the energy coupled to the liquid. The time constants and the maximum possible stroke of the system on the other hand are mainly determined by the properties of the liquid and may be tuned by choosing a liquid with an optimal combination of density, surface tension, and viscosity.

Robert A. Heinlein
Time Enough for Love, Ace Books 1987.

Chapter 4

Performance of the Liquid Mirror Device in Adaptive Optics

In this chapter the liquid mirror is operated and characterized in a number of different functions and setups - in first instance as a deformable mirror with the function to correct an aberrated wavefront in a classical adaptive optical setup. In a second setup the suitability of the liquid mirror for an application in fine imaging is explored. Finally, the liquid mirror device is applied as a spatial light modulator in order to manipulate the intensity distribution of an optical beam.

The most important function of a deformable mirror is its fundamental application as a device for the correction of aberrated wavefronts. All other functions, i.e. imaging and modulation, can be derived from it and consequently the main part of this chapter is dedicated to the characterization of this application mode. It includes the correction performance of the liquid mirror for static and dynamic aberrations as a function of various system parameters and the influence of liquid surface motion in the absence of external optical aberrations. The latter is demonstrated by means of a detailed comparative analysis of the tip and tilt modes.

Subsequently the analysis of the performance of the liquid mirror is expanded to the imaging application of the device. Image improvement as a function of different system parameters is summarily described and characterized. Finally, a brief demonstration of the function of the liquid mirror as a spatial modulator is given.

4.1   Wavefront Correction

An assessment of the quality of a deformable mirror not only depends on the specification of its separate parameters, e.g. the number of actuators or its maximum stroke, but ultimately on its performance as a part of a larger system. While in the last chapter the main focus was on the characterization of the different parameters, here the performance of the mirror inside an adaptive optical setup is characterized.

In a first step the static performance of the system was observed where a number of different wavefronts with constant aberrations produced by a stationary phase disk were corrected. Because the wavefronts were static, this measurement gives an impression of the ability of the mirror to assume a required arbitrary shape independent of any timing constraints. In a second step the dynamic performance of the mirror was measured where the wavefronts were aberrated by a rotating phase disk. Due to the element of change, now also timing is added to the evaluation of the quality of the deformable mirror. These results are then compared to the influence of the liquid surface when excited by ambient vibrations in the absence of external optical aberrations. This includes a detailed analysis of the distribution of Zernike modes present in the wavefront aberrated by the phase disk as well as the disturbances by ambient vibrations.

4.1.1   Measurement Procedure

In a first step, the control software, *Frontsurfer*, from Flexible Optical B.V. was used to calibrate the liquid mirror and to optimize the unaberrated far field image of the beam. Wavefront errors introduced by the setup (e.g. components or alignment) were compensated for by applying an offset in the form of Zernike modes to the liquid mirror. Once the optimized far field, i.e. a clear point source (see figure 4.1), was realized, the obtained values were defined as the reference wavefront.
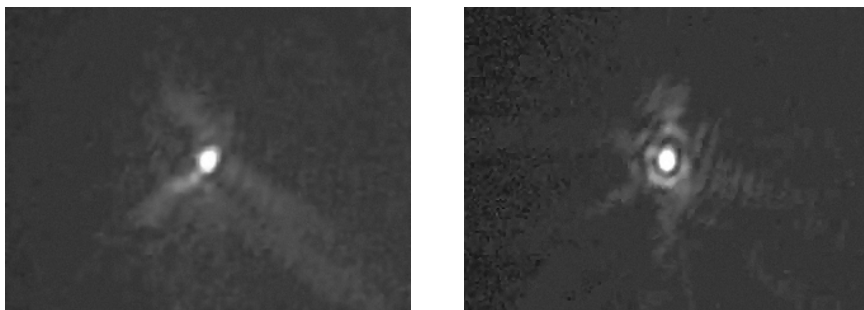
Figure 4.1: *Unaberrated far field of the beam – left: with wavefront errors introduced by the setup; right: optimized far field distribution with applied offset.*

All measurements were performed relative to this reference wavefront. It was used to compute the shape of the measured wavefronts and the derived data, e.g. rms-error, Strehl ratio, or the far-field wavefront.

The static measurements consisted of snapshots of the wavefronts and contained the state of the mirror and wavefront sensor, the shape of the wavefront, and a simulation of the far-field.

During the dynamic measurements the shape of the wavefronts was continuously monitored and logged in the form of the decomposed Zernike modes and the rms-error. Additionally, the state of the feedback (on or off) was monitored and recorded.

While the feedback was switched on, the system constantly monitored the wavefront with the wavefront sensor and compared the measured data to the reference wavefront to compute the signals to control the liquid mirror. When the feedback was switched off, the liquid mirror remained frozen its current shape unless it was set to zero. In this state the system continued to monitor the wavefront sensor and compare the current wavefront to the reference, but did not send any control signals to the mirror.

The performance of the mirror is evaluated in terms of the improvement, I, of the aberrated wavefront on the basis of the residual error expressed in μm. The improvement is defined as the ratio of the residual error without correction and with correction of the wavefront. Because the residual error with correction should be smaller than without correction, the improvement is a positive quantity larger than unity: $I > 1$.

4.1.2   Setup

Figure 4.2 shows the setup used for the correction of aberrated wavefronts. The light of a HeNe-laser was spatially filtered by a pin hole and recollimated to obtain a clean Gaussian beam that was aberrated by a rotating phase disk before it was directed to the liquid mirror to be corrected (figure 4.3). Behind the liquid mirror a part of the beam was directed onto a Shack-Hartmann type wavefront sensor with 127 subapertures. The remainder of the beam was imaged onto a CCD camera with a microscope objective to observe the far field intensity distribution of the beam. Photographs of the actual setup and liquid mirror device are shown in figures 4.5 and 4.6.

The liquid used in the liquid mirror was an aqueous solution of 80% glycerol with a density of $\rho = 1208.5 \, \text{kg/m}^3$ and a surface tension of about $\gamma = 56.7 \, \text{mN/m}$. The electrode structure used to apply a voltage and generate a static electric field to control the shape of the surface was a standard Flexible Optical B.V. electrode for a 37-ch 15 mm MMDM mirror consisting of 37 hexagonally arranged electrodes (figure 4.4) with a diameter of 1.9 mm each and an overall diameter of 15 mm. The maximum voltage was $U = 380 \, \text{V}$ and the distance between the
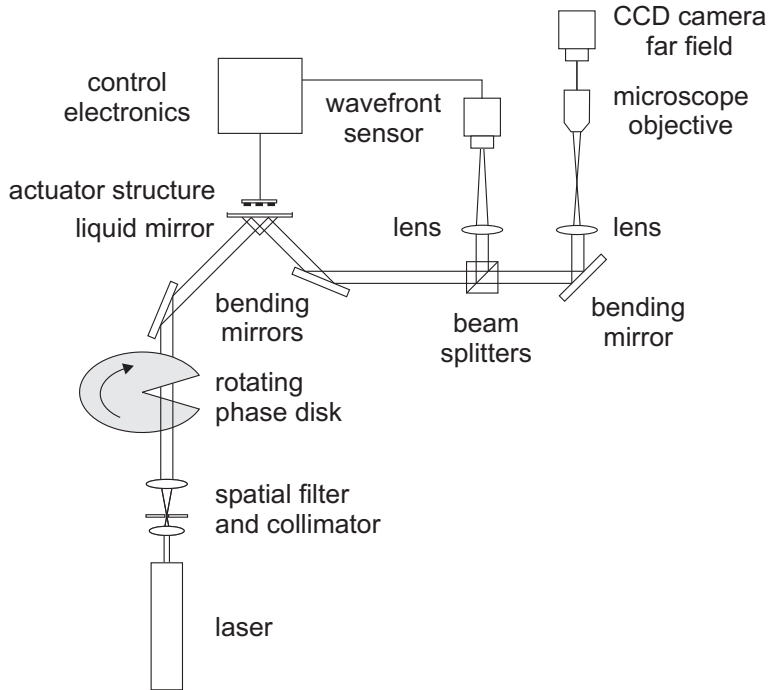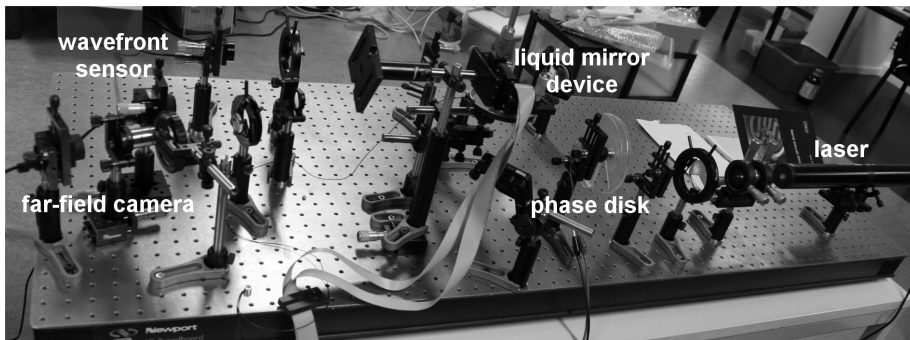
Figure 4.2: *Schematic image of the measurement setup for the correction of aberrated wavefronts.*
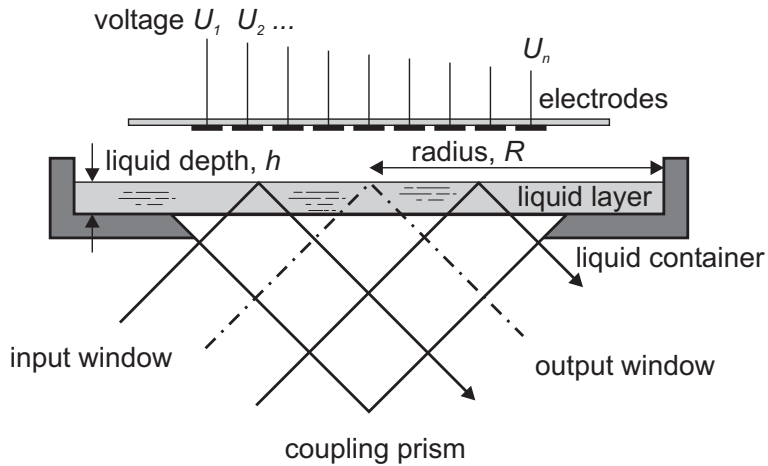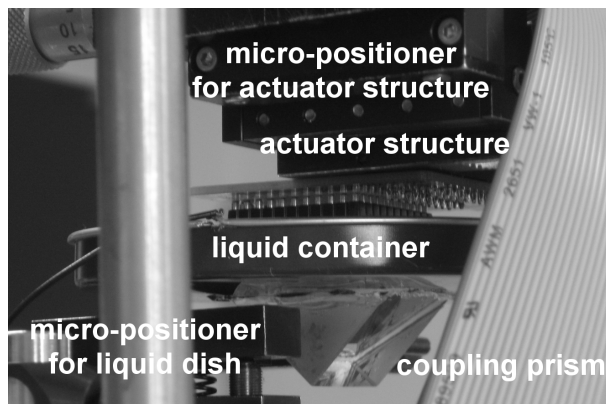

Figure 4.3: *The liquid mirror device.*
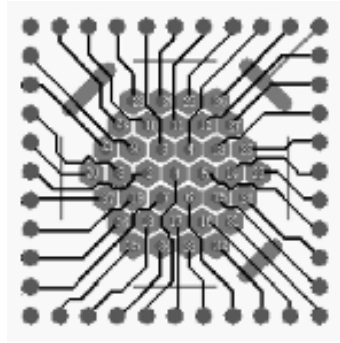
Figure 4.4: *Actuator structure of the 37-ch MMDM mirror manufactured by Flexible Optical B.V. [2]*

**Figure 4.5:** *Photograph of the measurement setup.*

Figure 4.6: *Realization of the liquid mirror device.*

actuators and the liquid surface was about $L = 550\,\mu$m, which resulted in a maximum stroke of about 13 μm (see also figure 3.36 in section 3.4.3.2 of the previous chapter).
The system was controlled by the software *Frontsurfer* by Flexible Optical B.V. The maximum correction frequency was about 37 Hz and the system delay was on the order of a few ms.

The setup was simulated with the optical design software Zemax. Figure 4.7 shows the setup in the non-sequential mode of Zemax. Figure 4.8 shows a simulation of the unaberrated and with 0.7 mrad tilted spots in the sequential mode, while a far-field pattern of the beam for different tilts of the liquid mirror is shown in figure 4.9. A simulation of the interference pattern and the deformed liquid surface are shown in figures 3.29 and 3.32 in section 3.4.3.1 of the previous chapter.
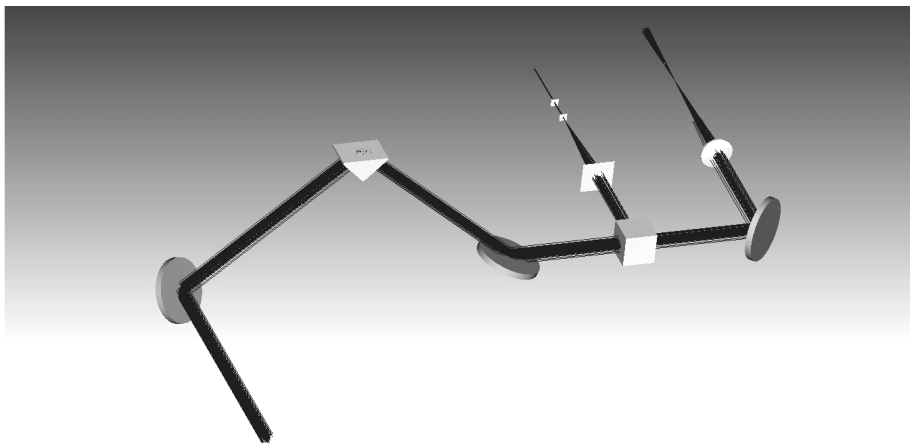

Figure 4.7: *Non-sequential mode Zemax model of the liquid mirror AO setup.*

4.1.3 Static Performance of the Liquid Mirror

For the static measurement of the performance of the liquid mirror wavefronts of the undisturbed, aberrated, and corrected beam were recorded for different positions of the phase disk. The undisturbed reference beam was recorded without the phase disk, while both the aberrated and the corrected beam were recorded for fixed positions of the phase disk in the beam with the mirror being flat for the aberration and the feedback engaged for the correction, respectively.
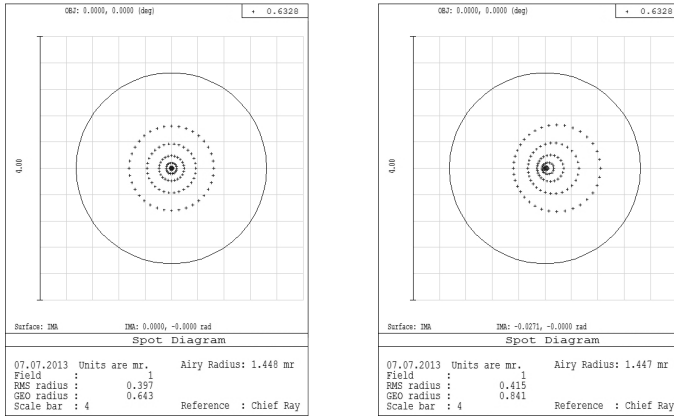
Figure 4.8: *Zemax spot diagram (sequential mode) of a beam without aberrations (left) and with 0.7* mrad *of tilt introduced by the liquid mirror (right). The solid circle corresponds to the Airy disk, i.e. the diffraction limited beam size, of the system.*
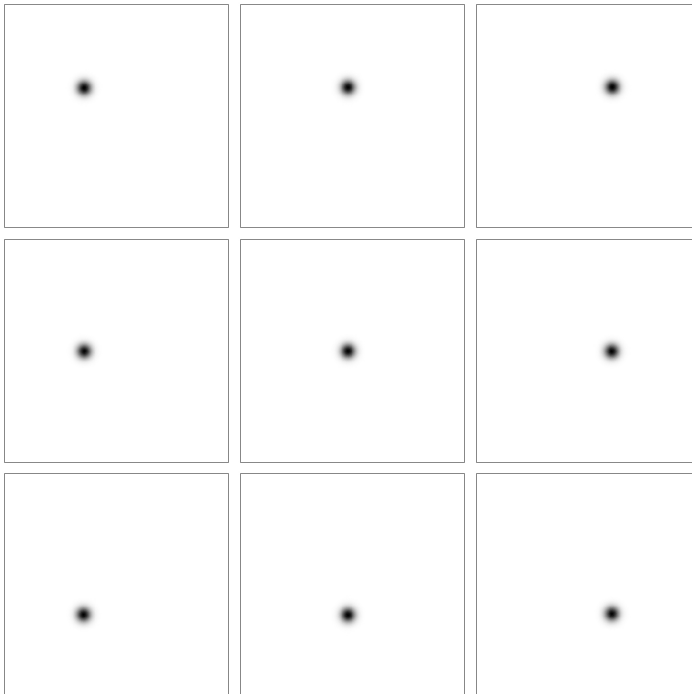
**Figure 4.9:** *Simulated far-field beams for different tilts of the liquid mirror (non-sequential mode): no tilt for the center beam, 0.7* mrad *for the up, down, left, and right displaced beams, and 1* mrad *for the corner beams; the area of the images is 6* mm *by 6* mm. *This corresponded to a displacement of 0.76* mm *of the up, down, left, and right displaced beams, and 1.08* mm *for the corner beams.*

For the analysis of the wavefronts at different positions on the phase disk the measurements included the position of the disk, φ, the peak-to-valley difference, ε_{PV}, the rms-error, ε_{rms}, and the Strehl ratio, S.

The amount of aberration was measured as the ratio of the Strehl ratios of the aberrated and the reference beams, $\Phi_a = S_a/S_r$, while the quality of the correction was correspondingly defined as the ratio of the Strehl ratios of the corrected and reference beams, $\Phi_q = S_c/S_r$, with the subscripts a, c, and r denoting the aberrated, corrected, and reference measurements, respectively. The performance of the mirror was measured as the improvement in terms of rms-error, the ratio of the rms-errors of the aberrated and corrected beams, $I_{rms} = \varepsilon_{rms,a}/\varepsilon_{rms,c}$, and Strehl ratio, $I_S = S_c/S_a$.

Two reference measurements were made, followed by the measurements of the performance of the liquid mirror in static mode. The results are summarized in table 4.1.
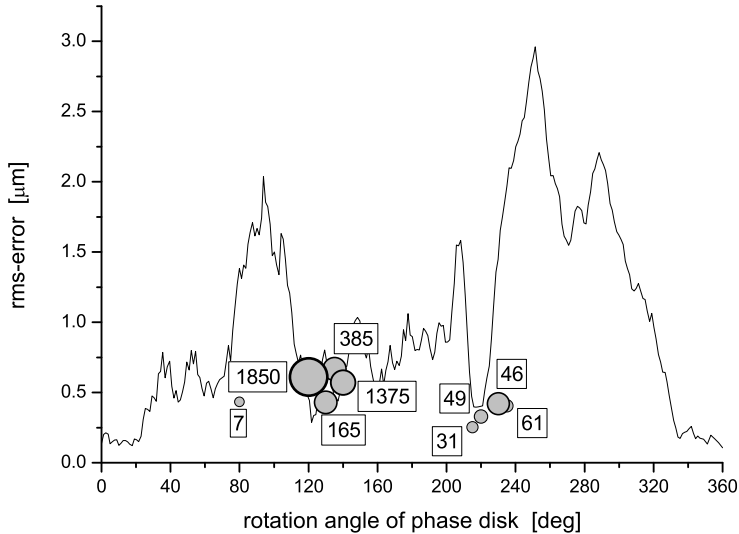
The definition of the position of the phase disk is shown in figure 4.10, while figure 4.11 shows the rms-error of the phase disk. The phase disk was built from a clear plastic disk that had a wedge cut out to let the laser beam pass undisturbed. The disk was treated with hair spray to produce locally diverse phase differences with approximately Kolmogorov statistics to replicate the effects of atmospheric turbulence [104, 105]. The graph shows the dynamically measured rms-error of the aberrated beam as a function of disk position for a full rotation of the phase disk. The circles show the positions and rms-error of the static measurements. The size of the circles corresponds to the improvement in terms of rms-error, I_{rms}, while the boxes note the corresponding improvement in terms of the Strehl ratio, I_S.
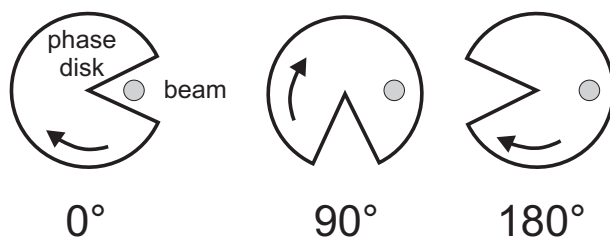
Figure 4.10: *Definition of the position of the phase disk.*

position	aberrated beam				corrected beam				improvement	
φ [deg]	$\varepsilon_{PV,a}$ [μm]	$\varepsilon_{rms,a}$ [μm]	S_a [-]	Φ_a [-]	$\varepsilon_{PV,c}$ [μm]	$\varepsilon_{rms,c}$ [μm]	S_c [-]	Φ_q [-]	I_{rms} [-]	I_S [-]
0	reference beam				0.297	0.042	0.794	-	-	-
80	2.424	0.433	0.012	0.015	0.793	0.137	0.079	0.100	3.16	7
120	3.190	0.611	0.0004	0.0004	0.377	0.050	0.740	0.778	12.44	1850
130	1.989	0.430	0.004	0.005	0.413	0.057	0.658	0.829	7.49	165
135	3.600	0.668	0.001	0.001	0.570	0.088	0.358	0.451	7.63	358
140	2.570	0.571	0.0004	0.0005	0.433	0.071	0.550	0.693	8.10	1375
215	1.240	0.253	0.017	0.021	0.445	0.071	0.528	0.665	3.59	31
220	1.650	0.329	0.01	0.013	0.622	0.075	0.487	0.613	4.39	49
230	2.910	0.421	0.014	0.015	0.396	0.058	0.649	0.682	7.27	46
235	2.306	0.405	0.004	0.005	0.767	0.104	0.245	0.309	3.90	61
0	reference beam				0.163	0.020	0.951	-	-	-

**Table 4.1:** *Results of the static correction measurements.*

Figure 4.11: *Dynamically measured rms-error of the phase disk as a function of disk position (solid line). The circles show position and rms-error of the static measurement. The size of the circles corresponds to the rms-improvement, I_{rms}, while the box gives the corresponding Strehl-improvement, I_S.*

Figures 4.12 and 4.13 exemplify results of the static wavefront correction: the images show the wavefronts (figure 4.12), the simulated far field (figure 4.13 top row), and the measured far field (figure 4.13 bottom row) for the aberrated (left), corrected (middle), and undisturbed beam (right) at disk position 140°.

Figure 4.11 shows that the rms-errors of the aberrated beam measured statically and dynamically roughly correspond to each other with the dynamically measured error being somewhat larger due to the additional contribution from the rotation of the phase disk.

Table 4.1 shows that both the improvement in terms of rms-error, I_{rms}, and in terms of Strehl ratio, I_S, are useful measures of the amount of wavefront correction that the liquid mirror is able to provide. Generally, it can be observed that the amount of improvement of both measures correlates well with an average improvement of $I_{rms} = 6.44$ and $I_S = 438$. However, the variation between the different values is much larger for the measurements based on the Strehl ratio as can be seen from a comparison of the standard deviations: $\sigma_S = 685$ and $\sigma_{rms} = 2.99$, which corresponds to 1.56 and 0.46 times the average values, respectively.
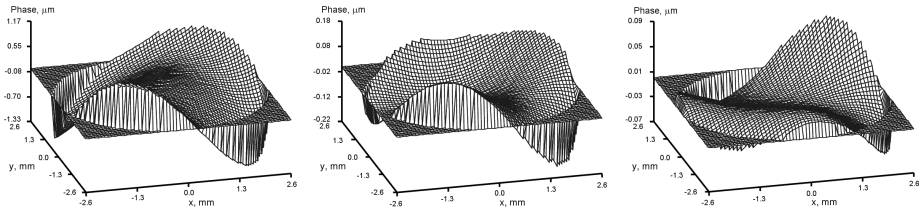
Figure 4.12: *Wavefronts of the aberrated (left), corrected (middle), and undisturbed beam (right) of the measurement at position $140°$. The image diameter is 5.2 mm and the peak-to-valley phase differences are 2.57 μm, 0.43 μm, and 0.30 μm, respectively.*
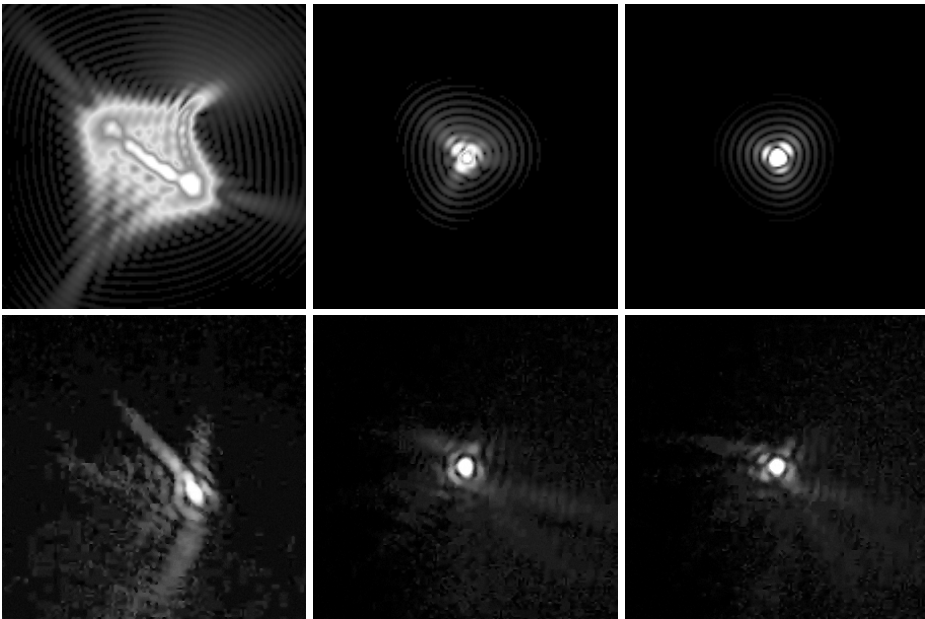
Figure 4.13: *Far field images of the beam - top row: reconstruction from the wavefront sensor data, bottom row: measurement with the CCD camera behind the microscope objective. The images show the aberrated (left), corrected (middle), and undisturbed beams (right).*

The higher variability of I_S as compared to I_{rms} can be explained by the way the values are calculated: while the rms-error is calculated over the entire surface of the wavefront the Strehl ratio is defined as the ratios of the intensity of the aberrated beam compared to an ideal beam on the optical axis. This leads to a very large dependence of the Strehl ratio on the specific type of aberration that is present in the distorted wavefront: theoretically, an otherwise perfectly flat wavefront with a large amount of tip and/or tilt would lead to a minute Strehl ratio, since the maximum intensity would be shifted from the optical axis, while the rms-error would not be significantly higher than the undisturbed beam. This is illustrated by figure 4.13 (bottom row, left), where the main contribution to the high improvement in terms of Strehl ratio is obtained by the shift of the maximum intensity away from the optical axis.

This means the improvement in terms of rms-error, I_{rms}, is less dependent on the specific composition of the aberration than the Strehl based improvement and thus the more objective measure of the amount of wavefront correction.

## 4.1.4   Dynamic Performance of the Liquid Mirror

In a second step the dynamic performance of the liquid mirror was measured with the rotating phase disk for different sets of parameters.
During the rotation of the phase disk the residual error of the wavefront was recorded with the feedback engaged and switched off. The feedback was switched on or off during the passage of the cut out part of the phase disk so that the static aberrations of the setup were corrected for even while the feedback was switched off. The residual rms-error of the wavefront was averaged for multiple rotations of the disk separately for active and inactive feedback and used to compute the improvement factor. Data recorded during the passage of the cut out part of the disk was excluded from analysis, since the beam is not distorted and the rms-error is very low independent of state of the feedback. A sample trace of such a measurement is shown in figure 4.14.

After a short discussion regarding the accuracy of the measurements, the improvement as a function of the system parameters feedback gain, g, feedback frequency, f, rotation speed of the phase disk, v, and the number of modes used for the correction, n, is described in detail in the following sections.

4.1.4.1   Estimate of measurement error

The accuracy of the measurement of the residual wavefront error depends on a large number of factors, e.g., the quality and alignment of the optical setup, the software (calibration and calculation), or noise. Therefore, it is impossible to derive an analytical expression for a reliable error estimate.
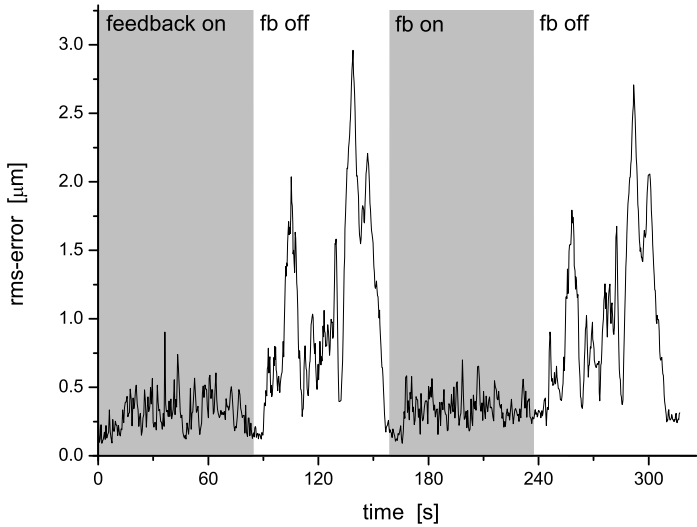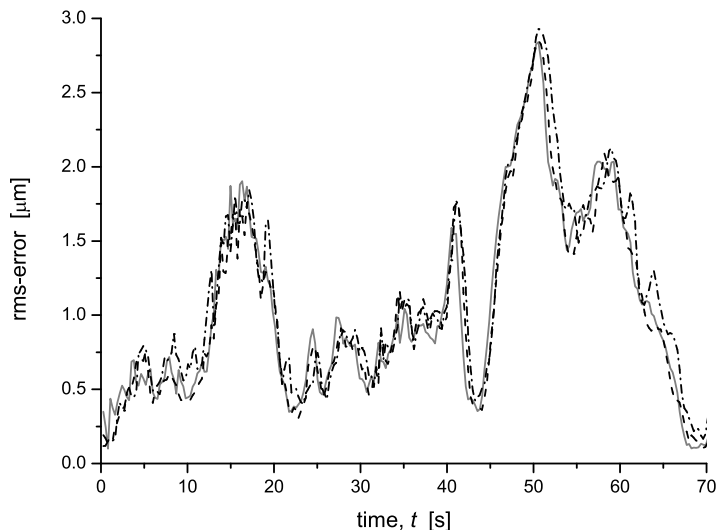
Figure 4.14: *Measurement of the wavefront rms-error with the rotating phase disk; the passages with the activated feedback are shown with grey background color. The feedback was switched on and off during the passage of the cut out part when the rms-error was especially low.*

Here, the error will be estimated through statistical methods from the measurements themselves: the same phase disk was used for all measurements, which means that the residual rms-error signal should be identical for all measurements that did not use the liquid mirror for correction. This implies that also the averaged error signal for the different passes that were used as data should be identical. Figure 4.15 shows uncorrected (feedback off) passages of the phase disk where the residual error signals are similar, but not exactly identical. The variation of the averaged error signal between the different passes encompasses all sources of noise and uncertainty and can thus be used as a measure for the accuracy of the measurement method.

The analysis of 65 uncorrected passes of the phase disk resulted in an average rms-error of $\bar{\varepsilon}_{\mathrm{rms, uncor}} = 1.00$ μm and a standard deviation of $\sigma_{\varepsilon, \mathrm{uncor}} = 0.060$ μm, so that the relative error for a measurement without adaptive optical correction was $\delta_{\varepsilon, \mathrm{uncor}} = 6\%$.

Analysis of the relative error of 52 corrected passes of the phase disk resulted in a relative error of $\delta_{\varepsilon, cor} = 8.1\%$.

Figure 4.15: *Different measurements of the wavefront rms-error for a single rotation of the phase-disk with the feedback switched off; the error signals are similar, but not identical.*

According to Gaussian error propagation the error of the improvement factor is then given by: $\delta_I = \sqrt{\delta_{\varepsilon,\,\text{uncor}}^2 + \delta_{\varepsilon,\,cor}^2} = 10.0\%$.

4.1.4.2   Gain

A feedback system compares the current state of the system to the desired state of the system and, should the current state differ from the desired state, applies a drive signal to the system in order to change the current state to the desired state. The gain of the system determines with which amount of the difference signal the system is driven. Depending on the details of the system the amount of gain determines whether a system is stable or not [106].

For an Adaptive Optics system the desired state is a chosen target wavefront while the current state of the system is the actually measured wavefront. From the current wavefront the system calculates signals that shape the deformable mirror in such a way that the target wavefront will be attained. The higher the gain factor the closer the system will follow the desired wavefront. However, with the rotating phase disk the wavefront that the sensor measured and that the control signals are based on will have changed by the time the deformable mirror reacts to the control signals. This means that in principle the system is unable to ever reach the desired state, which could lead to oscillatory behavior and thus an unstable system, if the gain factor is too large.

The improvement of the liquid mirror as a function of the gain factor is shown in figure 4.16.

Figure 4.16 confirms the expected result and shows that the measured improvement increases with increasing gain factor, thus showing that the mirror is formed more closely to the desired shape to reduce the rms-error. The improvement depends linearly on the gain with a slope of 3.68 up to a gain of 0.5 without showing signs of instable behavior.
Systems applying piezoelectric deformable mirrors have typically critical gain factors of 0.25, above which the systems become unstable.

4.1.4.3　Frequency

The bandwidth of a feedback system determines the range of frequencies of the input signal that a given system can still be operated with. The bandwidth is determined to a large extend by the frequency of the feedback system where a higher feedback frequency normally implies a higher bandwidth, so that the system can tolerate a higher rate of change of the input signal.
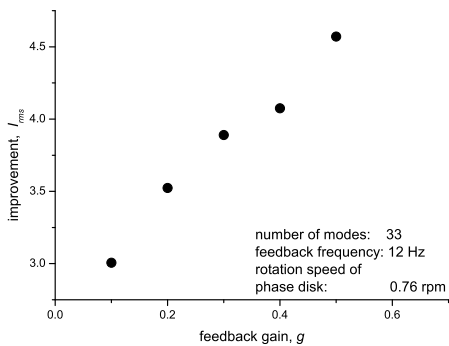The frequency dependency of the improvement of the liquid mirror is shown in figure 4.17.
The performance as a function of feedback frequency shows a rapid drop of the improvement factor at a low boundary frequency of about 12 Hz and a high boundary frequency of 32 Hz. The lower boundary shows the effect of the maximum possible delay at which a correlation between the actual error introduced by the phase disk and the correction applied to the mirror based on the delayed error signal still exists and the influence of the resonance of the system around 12 Hz (compare table 3.6). At the upper boundary of about 30 Hz the liquid mirror reaches the maximum rise-time after which the phase lag of the system prevents the liquid mirror from attaining the full amplitude of the required stroke (compare figures 3.38 (top) and 3.40 (right) of the last chapter), so that the aberration can no longer be fully corrected.
While the lower limit in this case is determined by the rate of change of the error introduced by the phase disk, the upper limit at 30 Hz is determined by the physical properties of the liquid and cannot be improved by changing the parameters of the feedback system.

4.1.4.4　Number of modes

The precision with which a given wavefront can be approximated by a deformable mirror is limited by the number and geometrical arrangement of the actuators. Generally, the more actuators a deformable mirror has the closer a required wavefront can be shaped. In every design of deformable mirror certain tradeoffs have to be made with respect to the density of actuators and the overlapping of influence functions (see section 3.4) or the obtainable stroke.
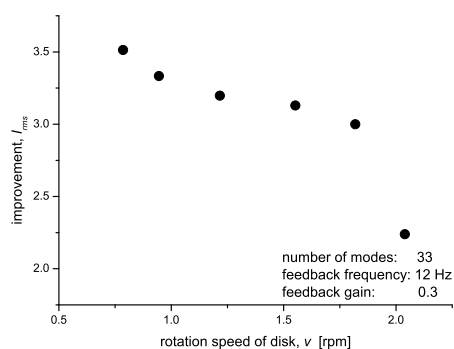
Figure 4.16: *Dynamic wavefront correction performance of the liquid mirror in terms of the improvement of the rms-error as a function of the feedback gain.*
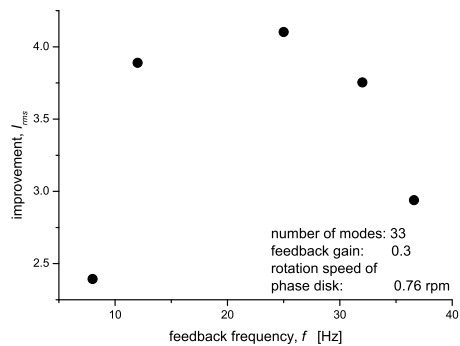
Figure 4.17: *Correction performance as a function of the control frequency.*
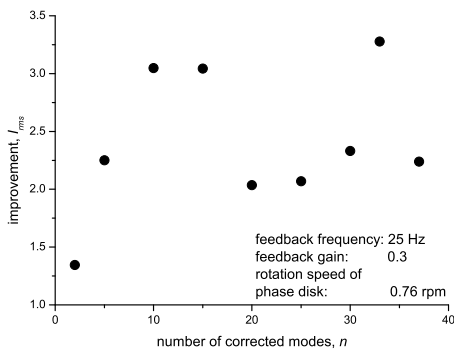
Figure 4.18: *Correction performance as a function of the number of correction modes.*

Figure 4.19: *Correction performance as a function of the rotational velocity of the phase disk.*

Here, the system is calibrated through measuring the influence matrix, $\mathbf{A}$, from which a matrix of system modes, $\mathbf{U}$, and a matrix of gains, $\mathbf{S}$, for these modes are calculated by singular value decomposition (SVD) [2, 107]. The system modes, $\mathbf{U}$, form an orthogonal set of modes that are used to decompose the measured wavefronts and calculate the necessary control signals for the mirror. This set of modes is determined by the properties of the deformable mirror and differs from the Zernike modes from section 2.2.1, although they may share certain properties, viz. the existence of the tip, tilt, and focus modes. The number of actuators and available modes is closely related – generally, there are as many system modes as there are actuators. However, due to the properties of the deformable mirror there might be modes that have very low gain and so little or no influence on the shaping of a wavefront and are best ignored [2, 108]. For practical reasons it is easier to ignore a mode than a single actuator, since all modes are defined across the entire pupil and thus all actuators are used by more than a single mode while modes should not mutually influence each other because of their orthogonality.
The improvement of the liquid mirror as a function of the number of correction modes is shown in figure 4.18.

Initially, the expected behavior is confirmed as the improvement rises by more than a factor of 2 from 2 modes to 15 modes. After that however there is a sharp drop by about $^1/_3$ for any number of higher modes with the exception of 33 modes.
In Adaptive Optics it has been observed that the lowest rms-error and thus the best correction is often not realized with the most number of modes – measurements using the electrode structure of the liquid mirror with a standard membrane mirror found that the lowest error was obtained for 14 modes [109, 110].
A comparison of the residual rms-errors of the aberrated and corrected beams is shown in figure 4.20, which shows that rms-error of the aberrated beam is independent of the number of modes used for the correction. Although the calculation of the improvement does not correct for changes in the rms-error of the aberrated beam, the main part of the calculated improvement is a function of the number of modes, since the change in the rms-error of corrected beam does not completely correlate with the change of the rms-error of the aberrated beam.

4.1.4.5 Velocity of the Phase Disk

Similar to the correction frequency the dependency of the correction quality on the velocity of the phase disk gives an indication of the temporal behavior of the liquid mirror and the feedback system. This depends both on the frequency with which the system is operated and the lag between the measurement of the input signal and the actuating of the deformable mirror where a slower rate of change of the input signal should result in a higher improvement. The result is shown in figure 4.19.
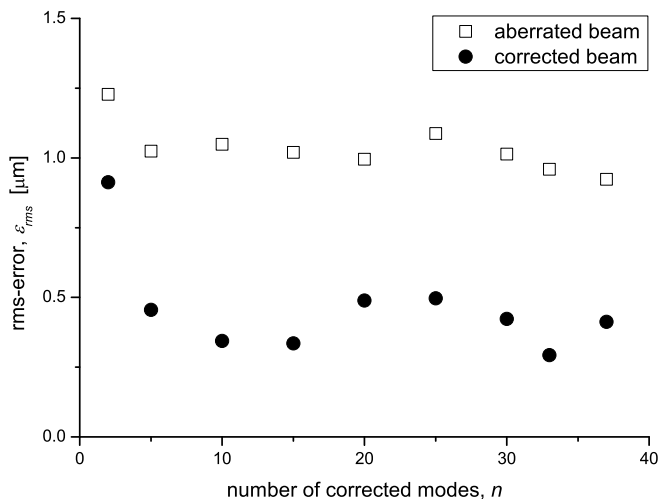
Figure 4.20: *Residual rms-errors of the aberrated and corrected beam as a function of the number of correction modes.*

An increasing velocity of the phase disk leads to slow drop in the measured improvement up to about 1.8 revolutions per minute after which there is a sharp drop of about 30% in improvement. The measurements show the slow decay of correlation between the correction and the actual aberration as the relative delay slowly increases due to the increased velocity of the phase disk while the correction frequency remains constant. Finally, at a velocity of 1.8 revolutions per minute the correlation between correction and aberration starts to break down completely and the improvement drops dramatically.

4.1.4.6   Modal Analysis

During the closed-loop operation of the liquid mirror the error signal of the wavefront sensor was deconstructed into a superposition of Zernike modes, whose coefficients were separately recorded in real time. Figure 4.21 shows an exemplary measurement of the average mode composition and strength of an aberrated and corrected beam (left) and the corresponding measurement of the rms-error (right). The parameters for this measurement were:

number of modes: 33,
feedback frequency: 12 Hz,
feedback gain: 0.4, and
speed of disk: 0.08 rad/s.

The modal composition of the aberrated and corrected beams show that the deflection of the beam (the tip and tilt modes, Z[1,1] and Z[1,-1]) constitutes the main contribution of the error while the higher modes are considerably smaller with decreasing contributions for the higher modes. The correction performance of the liquid mirror is reflected in both the much lower coefficients in the modal decomposition and the greatly decreased rms-error in the time trace of the rotating phase disk.

A more detailed analysis of the tip and tilt modes is shown in figures 4.22 to 4.25. From the coefficients of the tip and tilt modes an effective amplitude and direction of the deflection of the beam from the optical axis can be calculated: figure 4.22 shows the deflection of the beam without feedback and figure 4.23 the deflection with the feedback engaged. Clearly, the deflection introduced by the phase disk is reduced significantly. Figure 4.24 compares the histograms of the amplitude of the deflection with and without feedback, while figure 4.25 compares the angular distribution of the deflection. By activating the feedback the amplitude of the deflection is reduced by 80 % while the variability of the angular distribution is reduced by 18 %.

Analysis of multiple measurements shows a consistent reduction of the amplitude by over 70 %, while the variability of the direction is reduced between about 20 % and 50 %.

### 4.1.5   Correction of Ambient Vibrations

In the previous chapter it was shown (compare section 3.5.2) that the liquid surface can be excited by ambient vibrations. The details of that behavior depend on the shape and size of the container and the physical properties of the liquid itself.

Figure 4.26 shows the rms-error of a beam aberrated by a noisy liquid surface that was only excited by ambient vibrations without introducing wavefront errors with the phase disk (left) and the corresponding average modal composition of the aberrated and corrected beams (right). The parameters for this measurement were:

> 30 correction modes,
> 25 Hz feedback frequency, and
> 0.3 feedback gain.

Similar to the beam aberrated by the rotating phase disk the modal composition (figure 4.26, right) shows that the main effect of the ambient vibrations is the deflection of the beam off the optical axis.

The polar distribution plots, figure 4.27 without feedback and figure 4.28 with feedback, show the direction of movement to be oriented along the axis $15° - 195°$. Similar to the measurement with the phase disk, closing the feedback loop reduces the amplitude of the deflection by 22 % (figure 4.29) and the standard deviation of the angular distribution by 33 %.
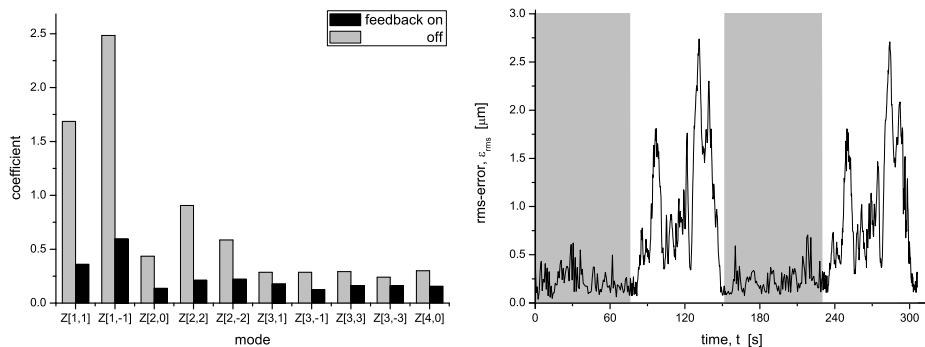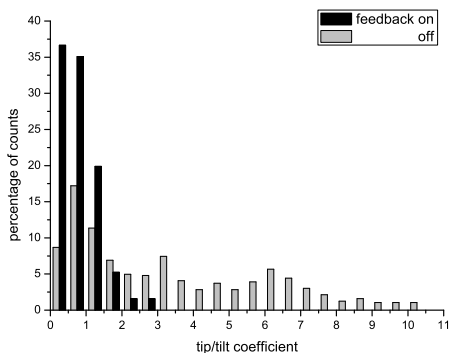
Figure 4.21: *Averaged modal composition of a beam aberrated by the phase disk and the corrected beam (left) and the corresponding rms-error where the passages with the activated feedback are shown with grey background color (right).*
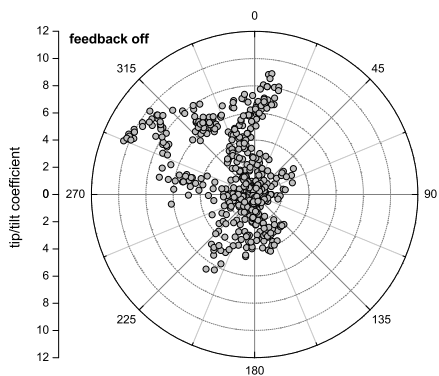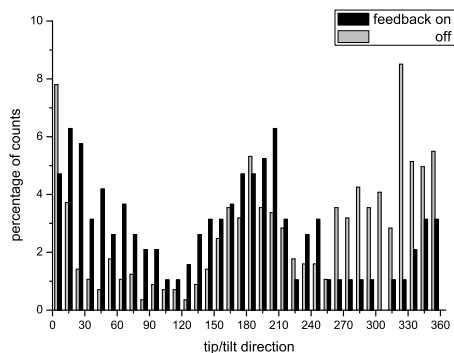

Figure 4.22: *Measured beam deflection of the phase disk without feedback.*
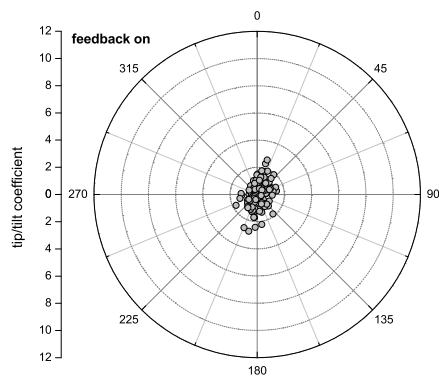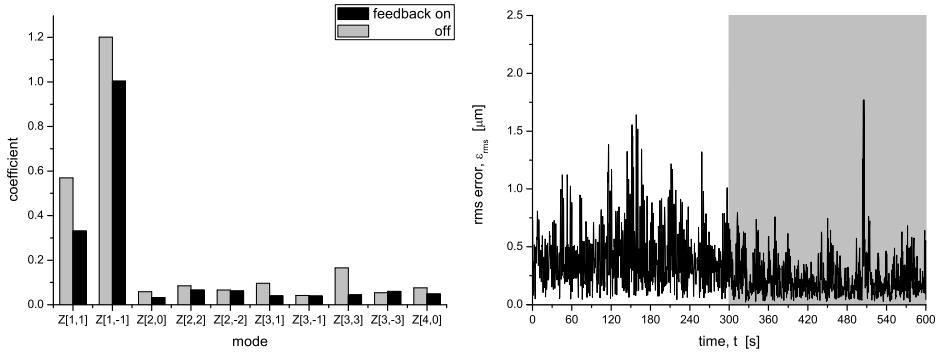
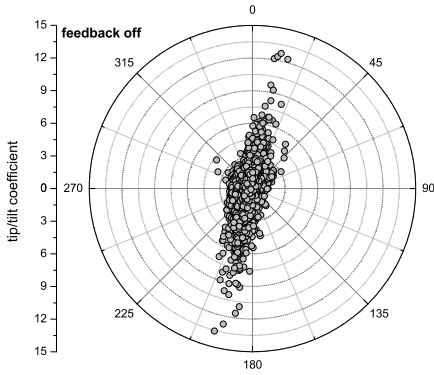**Figure 4.23:** *Beam deflection of the phase disk with feedback.*

Figure 4.24: *Comparison of the histograms of the amplitude of the deflection of the phase disk with and without feedback.*
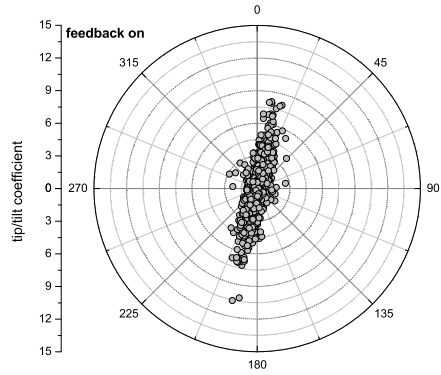
Figure 4.25: *Angular distribution of the deflection of the phase disk with and without feedback.*

Figure 4.26: *Averaged modal composition of a beam aberrated by ambient vibrations and the corrected beam (left) and the corresponding wavefront rms-error where the passage with the activated feedback is shown with grey background color (right).*

Figure 4.27: *Beam deflection induced by ambient vibrations without feedback.*

Figure 4.28: *Beam deflection of the ambient vibrations with feedback.*
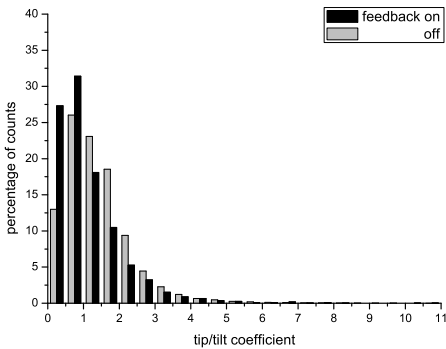
Figure 4.29: *Comparison of the histograms of the amplitude of the deflection induced by ambient vibrations with and without feedback.*

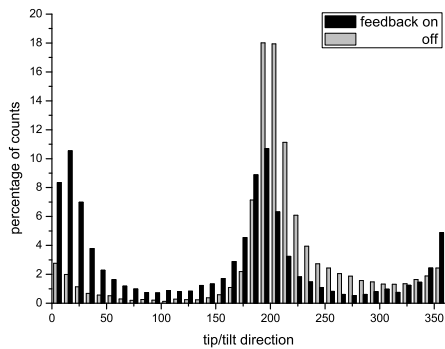**Figure 4.30:** *Angular distribution of the deflection induced by ambient vibrations with and without feedback.*

Typical results for the reduction of the strength of the tip/tilt modes show a consistent reduction of greater than 20 %, while the variability of the direction is reduced between about 30 % and 40 %. However, since the vibrations couple to a resonant mode of the system the movement of the surface cannot be suppressed completely, so that the main result is the symmetrical distribution of the deflections around the origin (figure 4.30).

Comparing the results for the phase disk and the ambient vibrations shows that the absolute strength of the tip/tilt modes induced by the ambient vibrations is about half of the effect caused by the phase disk, while the contribution of the higher modes is considerably smaller in relation (figure 4.31, left). This is supported by the corresponding measurement of the rms-errors (figures 4.21 (right) and 4.26(left)) where the uncorrected rms-error induced by the ambient vibrations is only a fraction of the uncorrected rms-error introduced by the phase disk.
By subtracting the contribution of the ambient vibrations the actual effect of the phase disk and correction by the liquid mirror can be observed. Figure 4.31 (right) shows the effective mode strengths of the uncorrected and corrected beam when aberrated by ambient vibrations. The largest contributions to the error are due to the low order modes with the largest contributions by tip and tilt, Z[1,1] and Z[1,-1], followed by the two astigmatism modes, Z[2,2] and Z[2,-2]. When the feedback is switched on the tip and tilt error introduced by the phase disk is almost completely corrected while all other modes show small residuals.
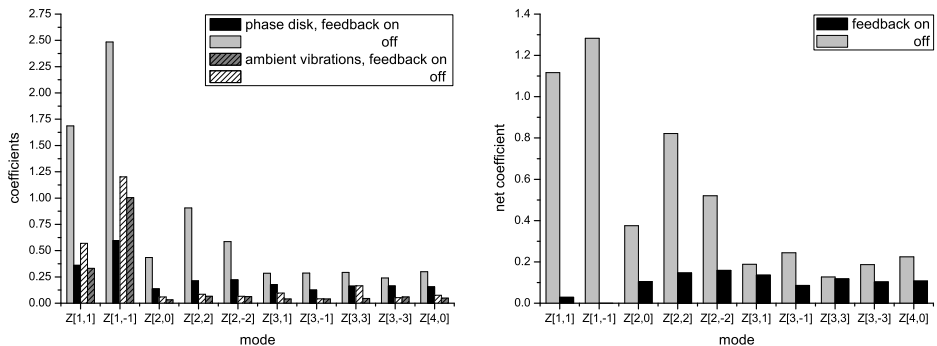
Figure 4.31: *Comparison of the averaged modal compositions of a beam aberrated by a phase disk and ambient vibrations with and without feedback (left) and the effective mode strength introduced by the phase disk with and without correction (right).*

The reason for this can be seen in figure 4.32 where the spectra of the measured rms-error of the phase disk (figure 4.21, right) and the ambient vibrations (figure 4.26, left) are shown.
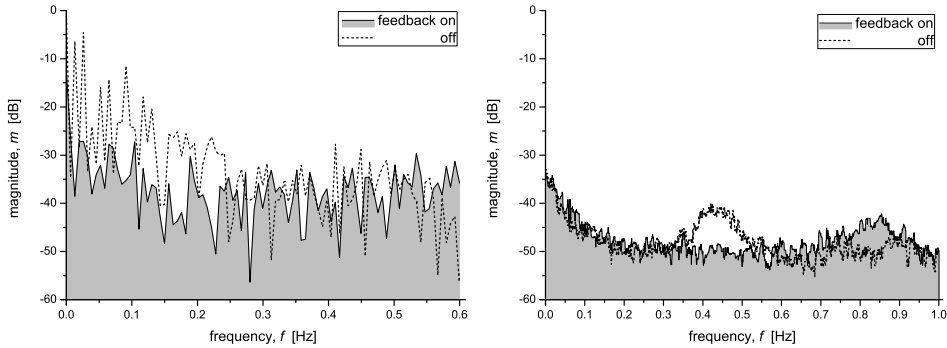
Figure 4.32: *Fourier spectra of the rms-error introduced by the rotating phase disk (left) and the ambient vibrations (right).*

The error spectrum of the uncorrected phase disk starts with a magnitude as high as -5 dB at low frequencies and drops to about -40 dB at about 0.3 Hz, after which there is a slight rise to about -35 dB at 0.45 Hz before it drops again to -50 dB at 0.6 Hz. The spectrum of the corrected phase disk resembles a v-shape with magnitudes of -30 dB at the low end of the spectrum, -45 dB at the minimum, and -35 dB at 0.6 Hz. This means that the main effect of the correction provided by the liquid mirror operates on the very low end of the error spectrum. For the uncorrected phase disk the low frequency peaks between 0 Hz and about 1.5 Hz form the main contribution to the measured error of figure 4.21 and are removed almost completely by the liquid mirror as is shown by figures 4.22 to 4.24.

The error spectrum of the uncorrected ambient vibrations drops from -35 dB at low frequencies to about -50 dB at 0.25 Hz after which it shows peaks with magnitudes of -40 dB at 0.44 Hz and -45 dB at 0.9 Hz, respectively. The first peak corresponds to the slight rise in the spectrum of the uncorrected phase disk and shows again that the measurements with the phase disk are always a superposition of the contributions of the ambient vibrations and the phase disk itself. The shape of the spectrum of the corrected vibrations corresponds to the uncorrected spectrum, but shifts the first peak to 0.85 Hz with a slightly reduced amplitude. This confirms that the operation of the liquid mirror on the ambient vibrations merely results in a reduction of the amplitude of the aberrations but not in a full correction (see also figure 4.29).

The shift of the peak due to the correction confirms a change in the dynamics of the liquid system similar to the change in damping times that was discussed in the previous chapter (see section 3.5.3) rather than a full correction of the ambient vibrations.

4.1.6   Discussion

In the wavefront correction setup the liquid mirror is able to correct static and dynamic wavefront aberrations (figures 4.13 and 4.14). In agreement with expectations in the static case a higher improvement, I, was measured than in the dynamic case with values of up to $I_{rms,\,\text{static}} = 12$ and $I_{rms,\,\text{dynamic}} = 4.5$ in the static and dynamic cases, respectively. The amount of improvement that can be obtained depends on the strength of the aberrations to be corrected and the parameters of the Adaptive Optics system (figures 4.16 – 4.19). The performance of the mirror is coupled to the disturbance of the liquid surface by ambient vibrations, which can be compensated partially by the liquid mirror during operation (figures 4.27 – 4.30).

Analysis of the modal composition shows that the ambient vibrations are basically limited to the first two modes, tip and tilt, while the aberrations of the phase disk also include higher modes (figure 4.31). While the liquid mirror reduces the strength of all error modes, it is most effective for the lower order modes, which is especially visible up to about five modes. Beyond the first five modes the effectiveness is reduced (up to about 15 modes) and for a higher number of modes the residual errors may increase again (figure 4.20). This is due to the influence function of the actuators (see section 3.4.3.2) and the mutual influence through the surface tension of the liquid. These issues my be addressed by tuning the geometry of the actuator structure and the properties of the liquid used.

In the given configuration the performance of the liquid mirror is optimal for the correction of lower order aberrations up to second order, astigmatism (figure 4.21), and low frequencies of up to a few Hz (figure 4.32).

Overall, the liquid mirror is well suited for correcting aberrated wavefronts – however, application of the liquid mirror implies a number of particular features that have to be observed, e.g. the horizontal orientation of the liquid or the sensitivity to ambient vibrations.

4.2   Imaging

The functionality of an adaptive optical setup to correct wavefront aberrations of a laser beam can also be used to correct an optical beam that carries an image. An image of a scene distorted by turbulence in the atmosphere or similar effects can be corrected by the deformable mirror when the phase errors that caused the distortions are known. A number of methods to enhance aberrated images directly or estimate the errors from the image have been proposed [111–117]. Here, the most direct method of measuring the wavefront of a laser beam propagating collinearly with the observed view is used. In principle, both the laser beam and the optical beam carrying the image propagate along the same path and pick up the same aberrations, so that identical corrections have to be applied to remove the aberrations.

While there is a universally agreed upon metric to quantify the amount of error of an aberrated wavefront, viz. the rms-error of the wavefront, no such clear measure exists for the quality of an image (for a review of image quality in vision science see for example [118, 119]). In a first step several methods to quantify image sharpness will be reviewed, after which the measurements and results of the image correction will be presented.

4.2.1   Image Quality

There exists no clear definition for the quality of an image, much less a quantitative measure for image quality. In the case of the correction of image distortion the most important parameter is sharpness, but even here no standard measure for quantification exists [120]. Thus, the first step for the evaluation of the performance of a system for image improvement is to find an objective measure for image quality.
Several methods for the evaluation of image sharpness have been proposed [121–127], four of which will be applied to the imaging data:

1. Image Contrast

   This sharpness metric is based on the sum over a nonlinear point transformation of the image intensity [120], which basically measures the contrast of the image, where a higher contrast implies a higher image sharpness, $\mathcal{S}$. The sharpness function is given by

   $$\mathcal{S} = \int dx dy \, I^n(x, y), \tag{4.1}$$

   where x and y are the coordinates in the image plane, I is the image intensity, and n is an integer [126]. In this case $n = 2$ is used.

2. Spatial Frequencies

This metric evaluates image sharpness based on the amount of high spatial frequencies contained in the image, where a large amount of high spatial frequencies implies a high image sharpness. The amount of high spatial frequencies is estimated by processing the image with a high-pass Fourier filter and generating a map of the high frequency distribution [122]. The sharpness metric is then given by the ratio of the total image intensities of the high frequency map and the original image.

3. Global Information

This metric bases its evaluation of image sharpness on the amount of information contained in the image as regarded by information theory. Here, a map of the global information content of the image is obtained by designating each pixel of the image its global information content based on its radiometrical properties, i.e. its intensity [124]. According to Shannon's information theory this can be expressed as [128, 129]:

$$I_N(x_i) = ln(N) - ln(n_i), \tag{4.2}$$

where I_N is global information content of pixel x_i, N is the total number of pixels and n_i is the number of pixels with the same intensity as pixel x_i.
In short, this metric assigns the highest information content to pixels that have a unique intensity while a pixel that shares its intensity with many other pixels has a low information content. The sharpness metric for an image is given by integration of the entire global information map where a higher value corresponds to a higher diversity of pixel intensities implying a higher image sharpness.

4. Local Information

This metric is also based on information theory - however, unlike the former metric the information content of a pixel is not viewed in relation to the entire image, but with respect to the direct environment of the pixel under consideration [124]. Based on this concept a map of the local information content of the image is generated where the sharpness metric is again given by integrating the local information map.

For an indication of the effect of the different sharpness metrics a reference image (4.33, top left) was convoluted with a Gaussian filter with increasing standard deviation, sigma. The image had dimensions of 320 x 240 pixels corresponding to the size of the data images. The Gaussian filter had a size of 15 and standard deviations of 1 to 5. The results are shown in figure 4.33.

Figure 4.33: *Images used for the reference measurements with different amounts of Gaussian blur. Top row: left: no blur, middle:* `sigma = 1`*, right:* `sigma = 2`*; bottom row: left:* `sigma = 3`*, middle:* `sigma = 4`*, and right:* `sigma = 5`*.*

Figure 4.35 shows the different sharpness metrics mapped to the original reference image, figure 4.34, while figure 4.37 shows the corresponding sharpness maps for a blurred reference image, figure 4.36, for comparison.

The sharpness, $\mathcal{S}$, was calculated for all images of figure 4.33 with each of the different methods. In order to be able to better compare the characteristics of the different metrics a normalized sharpness metric, $\mathcal{S}'$ was computed for which the sharpness values of the blurred images were normalized to a range of $[0, 1]$ where the sharpness of the unblurred image corresponds to 1 and the sharpness of the image blurred with `sigma = 5` to 0. The result is shown on the left in figure 4.38.

The above normalization does not show the absolute behavior of the different metrics, so that additionally the relative improvement, R, was calculated. The relative improvement relates the sharpness of a sharp image to a blurred image and is defined as:

$$R = \frac{\mathcal{S}_{\mathrm{sharp}}}{\mathcal{S}_{\mathrm{blurred}}} - 1, \tag{4.3}$$

with $\mathcal{S}_{\mathrm{sharp}}$ and $\mathcal{S}_{\mathrm{blurred}}$ the image sharpness of the sharp and blurred images, respectively. In the case of adaptive imaging the sharp and blurred images correspond to corrected and uncorrected images, respectively.

**Figure 4.34:** *The original reference image.*

Figure 4.35: *Sharpness maps of the original reference image for the different sharpness metrics. Top left: image contrast, top right: spatial frequencies, bottom left: global information, and bottom right: local information.*
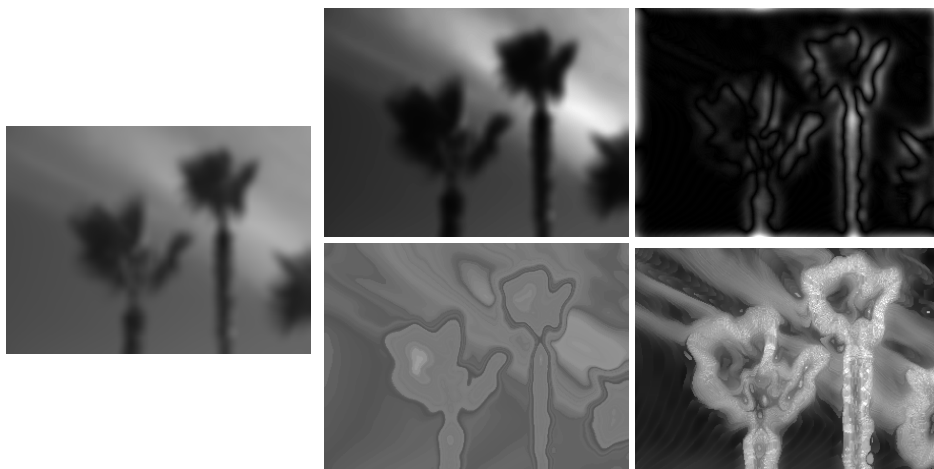
Figure 4.36: *Reference image with added Gaussian blur of* `size = 15` *and* `sigma = 5`.

Figure 4.37: *Sharpness maps of the blurred reference image for the different sharpness metrics. Top left: image contrast, top right: spatial frequencies, bottom left: global information, and bottom right: local information.*

Here, the blurred image with `sigma = 5` corresponds to the uncorrected image
and all other images are adaptively imaged with different degrees of correction.
The results are shown on the right in figure 4.38. It is noteworthy that the cal-
culated relative improvement increase of the spatial frequencies metric is so large
that all other metrics had to be multiplied by a factor of ten to still be easily
distinguishable.
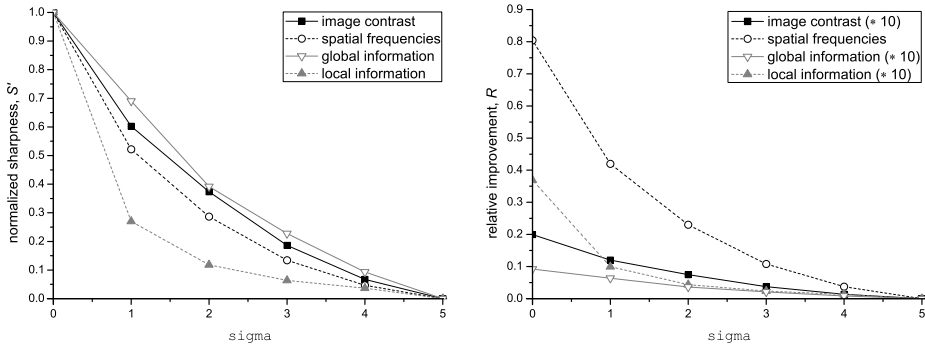
Figure 4.38: *Left: Sharpness of the images shown in figure 4.33 calculated according
to the different sharpness metrics normalized to the interval [0,1]; right: relative
improvement, R of the different images of figure 4.33 calculated for all metrics relative
to the image blurred with* `sigma = 5`*, the results of the image contrast, global and
local information metrics have been magnified by a factor of ten for better distinction.*

Figure 4.38 (left) shows a decrease in the calculated sharpness for increased sever-
ity of the image blur for all metrics.
The local information metric shows a steep initial loss of sharpness from the orig-
inal image to the blurred image with `sigma = 1` and a progressively decreasing
rate of the decline of image sharpness after that. All other metrics show a more
constant rate of sharpness loss and thus correlate better to the human perception
of image sharpness.
The relative improvement (figure 4.38 right) shows the absolute increase in im-
age sharpness calculated from the data for the different images compared to the
image blurred with `sigma = 5` ($R = 0$). The change of the spatial frequen-
cies metrics is more than an order of magnitude larger than any of the other
metrics, viz. $R_{\text{spatial frequencies}} = 80\,\%$ as compared to $R_{\text{image contrast}} = 2\,\%$,
$R_{\text{global information}} = 1\,\%$, and $R_{\text{local information}} = 3.7\,\%$, which implies that it should
be able to detect small improvements in image sharpness. This makes the spatial
frequencies method the most promising method for the evaluation of the perfor-
mance of the liquid mirror in imaging applications.

4.2.2 Setup

The imaging setup is shown in figure 4.39. The beam of a HeNe-laser and an optical beam carrying the image of the filament of an incandescent light bulb were superimposed collinearly and distorted by a rotating phase disk. After correction with the liquid mirror the beam was split with part of the beam being directed to the Shack-Hartmann wavefront sensor and part of the beam being directed to an imaging CCD camera.

The control signals for the liquid mirror were solely based on the measurement of the aberrations of the beam of the HeNe-laser which was accomplished by placing a bandpass filter for 633 nm in front of the wavefront sensor. A bandpass filter for 532 nm was placed in the beam directed to the imaging CCD camera to prevent the laser from saturating the CCD camera.

The remainder of the beam was used to form an interferogram of the surface of the liquid mirror that could be used as an additional diagnostic tool for the state of the system; however, this was not recorded. All other parameters of the system were unchanged from the wavefront correction measurements (see section 4.1.2).
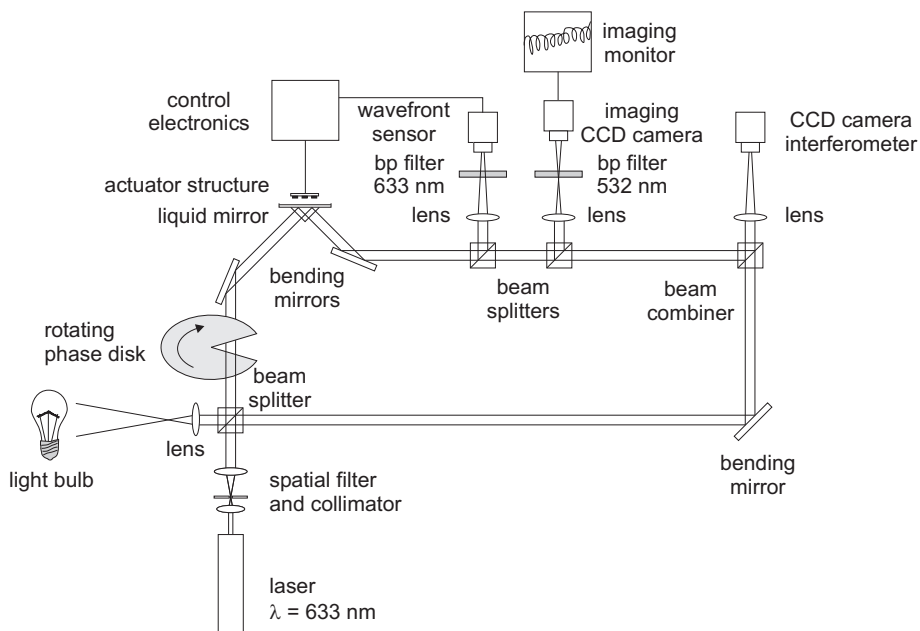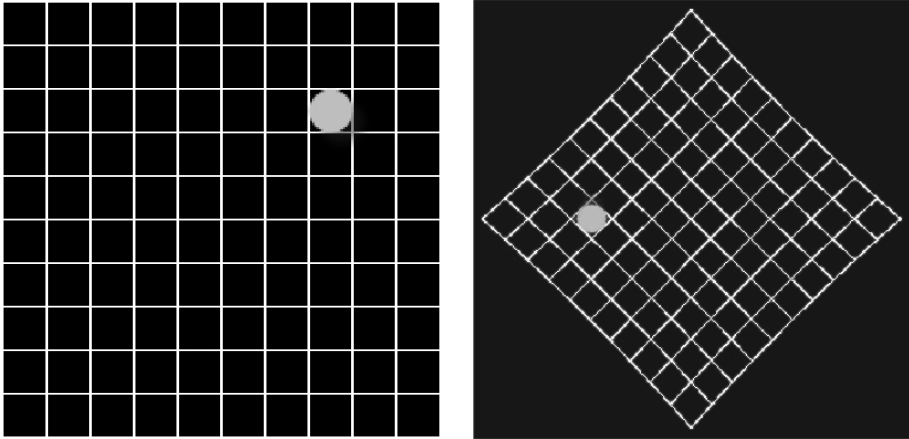

Figure 4.39: *Imaging setup for the correction of distorted images.*

The setup was simulated with the optical design software Zemax. Figure 4.40 shows the setup in the non-sequential mode of Zemax. A simulation of an image propagated through the setup is shown in figure 4.41.
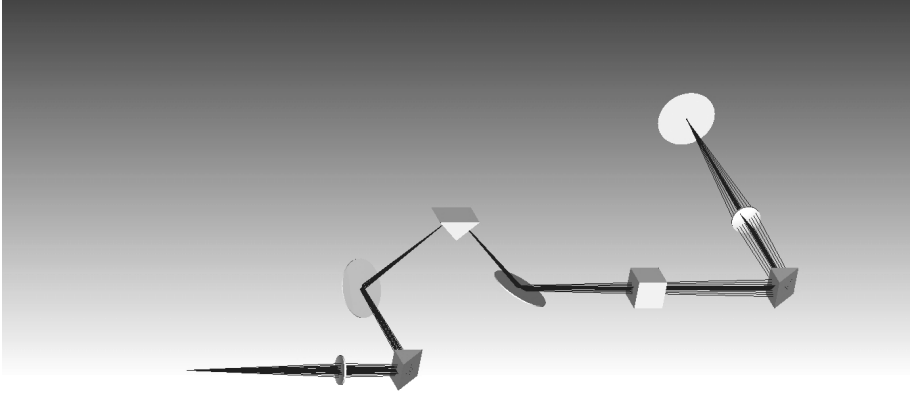
Figure 4.40: *Non-sequential mode Zemax model of the liquid mirror imaging setup.*


Figure 4.41: *Simulated propagation of an image through the setup from the object plane via the liquid mirror to the image plane: original image in the object plane (left) and propagated image in the image plane (right).*

4.2.3 Measurements and Results

Similar to the measurements for the correction of wavefronts (see section 4.1.4) the optical beam was distorted by a rotating phase disk with the feedback of the system switched on and off while the filament of an incandescent light bulb was imaged through the system (figure 4.42).

The transmitted images were recorded by a camera as movies with different system parameters. The recorded movies were separated into their constituting frames and cropped from their original dimensions of 640 x 480 pixels to a size of 320 x 240 pixels (see figure 4.42) in order to reduce the computing time and improve the signal to noise ratio by removing a large part of the background. The images of reduced size were processed according to the different methods set forth in section 4.2.1 to quantify the sharpness of each separate frame.

For each method the obtained sharpness results were averaged separately over all frames with the feedback switched on and off. From the two resulting values an improvement ratio was calculated as an indication of the effect of the image correction by the liquid mirror as measured by the different methods.
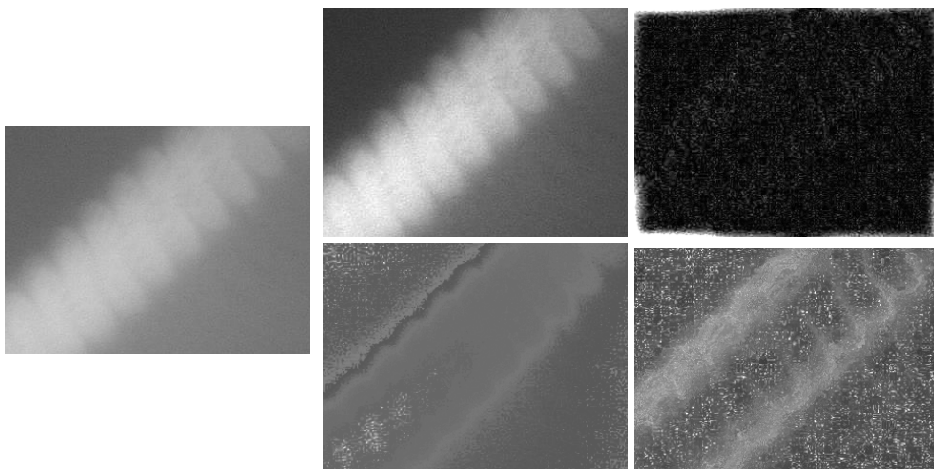
Figure 4.42: *Exemplary undistorted image of the filament of an incandescent light bulb imaged through the liquid mirror imaging system.*

Figure 4.43: *Sharpness maps of the filament image for the different sharpness metrics. Top left: image contrast, top right: spatial frequencies, bottom left: global information, and bottom right: local information.*

Comparing figures 4.43 and 4.37 shows that the image used for the processing suffers from two drawbacks with respect to the reference image, i.e. a lack of

high spatial frequencies and a high noise level. These effects are especially visible in the maps of the spatial frequencies and local information metrics. This first impression indicates that in contrast to the expectation of section 4.2.1 the best results may be obtained from the sharpness and global information metrics.

An example of the performance of the liquid mirror is shown in figures 4.44 and 4.45. The imaging setup was operated with different sets of parameters while using the rotating phase disk. As during the wavefront correction (see section 4.1.4 the imaging was performed for multiple rotations of the phase disk with and without closing the feedback loop, where the feedback was switched during the passage of the cut-out part of the phase disk. The residual rms-wavefront error was monitored during the imaging measurements and is shown as the dashed line while the grey background color indicates when the feedback was activated for both images. For a more discernable presentation of the evaluation of the results by the different metrics the data is shown in two separate diagrams, viz. figure 4.44 shows the sharpness as a function of the rotating phase disk as evaluated with the image contrast and the spatial frequencies metrics and 4.45 as evaluated with the global and local information metrics.

The qualitative pattern of the different sharpness metrics shown in figures 4.44 and 4.45 represent typical results across all measurements with different parameters. They show that in contrast to the measurement of the rms-error no obvious difference between the image sharpness with and without operation of the liquid mirror can be observed. Furthermore, figure 4.45 shows a strong similarity of the pattern for the global and local information metrics, while the pattern of the image contrast and spatial frequencies metrics strongly fluctuate (figure 4.44).
Both the global and local information as well as the spatial frequencies metrics show an increase in image sharpness for the passages of the cut out part of the rotating phase disk when the rms-error was especially low and the feedback was switched on or off while the image contrast metric does not. While these passages were specifically excluded from the analysis when evaluating the performance of the liquid mirror, the occurrence of said passages raises questions as to the applicability of the image contrast metric for this type of data.

The different sharpness metrics were averaged for multiple rotations of the disk separately for active and inactive feedback and used to compute a relative improvement factor, R, according to equation 4.3:

$$R = \frac{\overline{\mathcal{S}}_{\text{fb on}}}{\overline{\mathcal{S}}_{\text{fb off}}} - 1, \tag{4.4}$$

with $\overline{\mathcal{S}}_{\text{fb on}}$ and $\overline{\mathcal{S}}_{\text{fb off}}$ the averaged image sharpness with the feedback switched on and off, respectively.
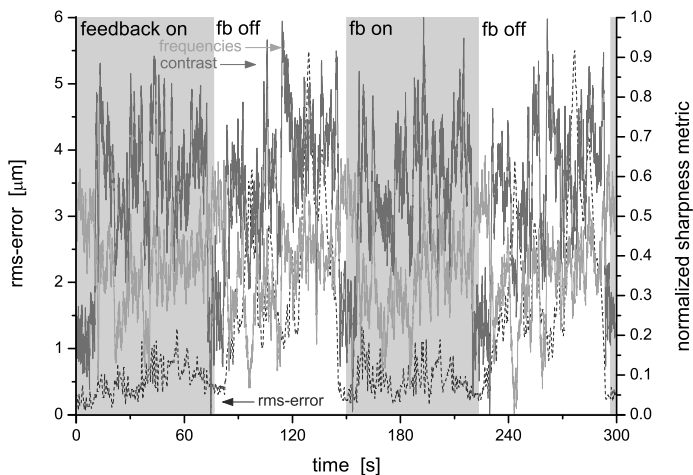
Figure 4.44: *Evaluation of the image correction with the rotating phase disk; the sharpness of the light bulb filament imaged with the liquid mirror device is evaluated by different metrics - here, the image contrast and the spatial frequencies metrics, the other metrics are shown in figure 4.45. The passages with the activated feedback are shown with a grey background color. For comparison the simultaneously measured rms-error is also displayed, the feedback was switched on and off during the passage of the cut out part of the phase disk when the rms-error was especially low.*
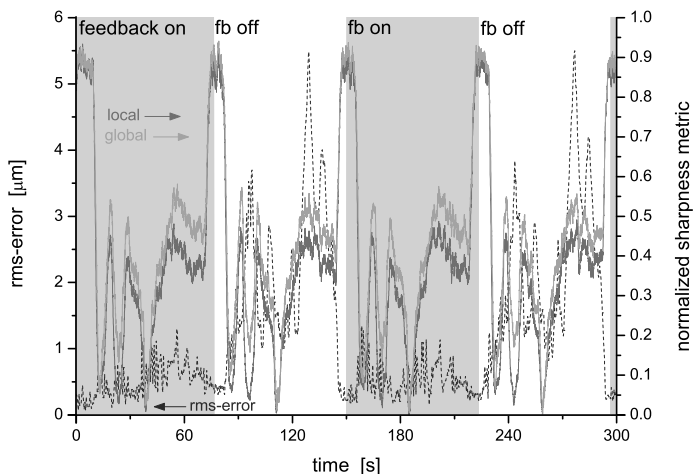

Figure 4.45: *Evaluation of the image correction with the rotating phase disk; here, the normalized sharpness calculated with the local and global information metrics are displayed, the other metrics are shown in figure 4.44.*
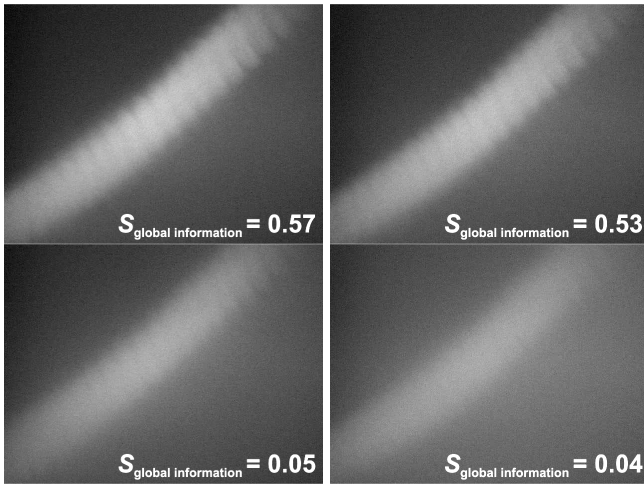
Figure 4.46: *Imaging results with the liquid mirror; top row: images with relatively high measured sharpness, bottom row: low measured image sharpness, left column: images with correction, and right column: images without correction. The images correspond to the data points shown in figure 4.47.*

During the imaging experiments the liquid mirror was operated with a feedback gain of $g = 0.2$ and a feedback frequency of $f = 25\,\text{Hz}$ while the number of modes and the speed of the rotating phase disk were varied.

Figure 4.46 shows exemplary frames taken from the data representing different states of the system, viz. feedback on/off in the left and right columns, respectively, and high and low measured image sharpness using the global information metric in the top and bottom rows, respectively. The points of highest measured sharpness corresponding to the passage of the cut out part of the rotating phase disk were not considered, since without aberration no effect of correction can be measured. The positions where the frames were measured are shown in figure 4.47. Here the global information metric is shown along with the residual rms-error. Superficially, the difference in sharpness between the images of figure 4.46 with and without feedback is negligible while the difference between the low and high measured image sharpness is easily observed. This is confirmed by the traces of figure 4.47: while the measured rms-error shows a distinct difference with and without feedback the shape of the sharpness metric does not differ by much. Without correction the curves of the rms-error and the sharpness metric exhibit a certain degree of anti-correlation, especially in the first half of the rotation of the phase disk – the image sharpness being lowest when the error is greatest. During the second half of the rotation both rms-error and the image sharpness are high, indicating that the main contribution to the rms-error comes from the tip- and tilt-modes that are disregarded in the sharpness evaluation.
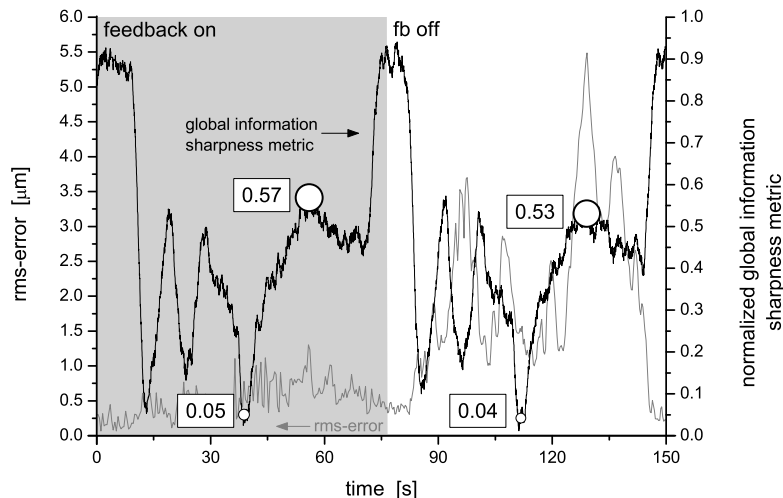
Figure 4.47: *Measurement of the global information sharpness metric (black line) and the rms-error of the phase disk (grey line). The circles show the positions of the images shown in figure 4.46, the size of the circles corresponds to the measured sharpness given in the box.*

These measurements have been repeated for different velocities of the phase disk and numbers of correction modes of the liquid mirror. The results are shown in figure 4.48.

Here, as in figures 4.44 and 4.45 the difference between the two groups of sharpness metrics, viz. local and global information on one hand and image contrast and spatial frequencies on the other, is easily observed. Interestingly, the latter group exhibits a number of negative values, i.e. the image sharpness actually was worse with correction than without, while the former group consistently shows an improvement of the image sharpness.

However, figure 4.48 shows that while the spatial frequencies metric shows the expected characteristic, i.e. increasing sharpness with increasing number of correction modes and decreasing sharpness with increasing velocity of the phase disk, the absolute values of both the image contrast and spatial frequencies metrics for the relative improvement, R, are only on the order of a fraction of a percent. Additionally, figure 4.44 shows both the metrics to fluctuate strongly, which leads to the suggestion that these metrics do not represent an optimal sharpness metric for this type of data.
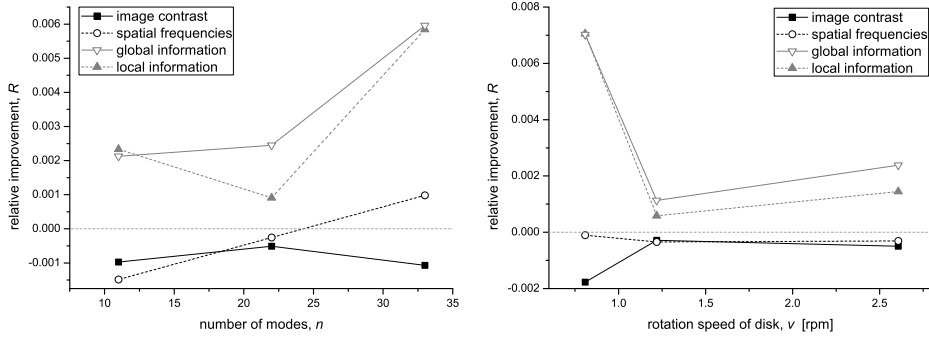
Figure 4.48: *Left: the relative improvement for the different metrics as a function of the number of correction modes; right: the relative improvement as a function of the velocity of the phase disk.*

On the other hand, however, both the local and global information metrics show overall trends that fit the expectations and their absolute values of R span a range of about $0.5\,\%$ which corresponds to the expected values as shown in figure 4.38. While the individual errors of the separate values might be estimated to be as high as $0.3\,\%$ the overall trend is significant and shows an improvement of the image sharpness as a result of the correction by the liquid mirror.

4.2.4   Discussion

For the evaluation of the recorded images several quality metrics with different sensitivities for changes in image sharpness have been used (figure 4.38). It has been found that the algorithms can be grouped according to the results of the evaluation, i.e. the results of the local and global information metrics correlate strongly while both the image contrast and the spatial frequency metrics strongly fluctuate (figures 4.44 and 4.45).

While the quantitative improvement of the image quality is limited, it can be easily observed (figure 4.46). However, there is no clear correlation between the measured image quality either between the different metrics or between the sharpness metrics and the measured wavefront error. The cause for both of these is the fact that the main contribution to the measured wavefront error originates from the tip and tilt modes, i.e. the deflection of the beam. These two modes, however, have no influence on the image sharpness, and thus this error is not evaluated or quantified by the sharpness metrics. The latter is also aggravated by the fact that

systematic wavefront errors introduced by the setup are not removed through a calibration step, unlike for the setup for wavefront correction in section 4.1.1. This applies in particular to the effect of the orientation of the liquid mirror at an angle of 45 deg with respect to the direction of beam propagation and thus to the conjugate plane that is imaged onto the wavefront sensor. The effect of this is indicated by the simulated propagation of an image in figure 4.41 and may be compensated by a proper calibration and optimization of the optical system.
The performance of the liquid mirror is optimal for the correction of low order aberrations at low frequencies, while the image sharpness is equally degraded by high error modes and fast aberrations. As a consequence, a significant amount of aberrations are not removed by the liquid mirror.

The liquid mirror was successfully used in a fine-imaging setup – although it was shown not to be well suited for the correction of images aberrated by a rotating phase disk. However, the liquid mirror can still be used for the correction of images in astronomical telescopes, since the atmospheric conditions mainly lead to a smearing of the optical intensity caused by image wander, i.e. the main contribution of the image aberration can be corrected with the tip and tilt modes.

4.3   Spatial Modulation

A spatial light modulator (SLM) is a device that modulates properties of an optical wavefront [130]. While many spatial light modulators based on different concepts have been realized [130–132], this implies that in principle every deformable mirror is, and can be used as, a spatial light modulator.

In the following section it will briefly be shown that the liquid mirror can indeed be used as a spatial light modulator to manipulate the wavefronts of the beam of a HeNe-laser and shape the far-field intensity distribution.

4.3.1   Method

The deformable mirror locally manipulates the phase of a beam by modulating the path lengths traveled across the wavefront, so that an originally flat wavefront can be given any shape the deformable mirror is able to form. However, in order to function as a spatial light modulator, these phase changes have to be converted into amplitude changes. Different methods can be used for that, e.g. the central dark ground method of observation, the Schlieren method, or the phase contrast method [66]. Here, we will use the Schlieren method, where a knife edge is placed in the focus of a lens masking the center and one half of the spatial spectrum. For a flat liquid surface there are no higher spatial frequencies, so that all the intensity is at the center of the Fourier spectrum and no light is passed beyond the knife edge. Modulation of the liquid surface broadens the spatial spectrum of the beam in the focus and the light containing this information passes the knife edge and is converted by a second lens into an image containing the local intensity information. This method was already applied in section 3.5.2 of the previous chapter.

4.3.2   Setup

Figure 4.49 shows the setup used to realize the SLM with the liquid mirror. The light of a HeNe-laser was spatially filtered by a pin hole and recollimated to obtain a clean Gaussian beam that was subsequently split into two beams. Part of the beam was directed to the liquid mirror for manipulation, while the remainder was recombined with the modulated beam to form an interferometer. After modulation by the liquid mirror a part of the beam was focussed on a knife edge and imaged onto a CCD camera to observe the far field intensity distribution. The remainder of the beam was used to form the interferogram of the surface of the liquid mirror that was also recorded with a CCD camera. The control signals were set by hand from the control software, *Frontsurfer*, from Flexible Optical B.V.

All other parameters of the system were unchanged from the wavefront correction measurements (see section 4.1.2).
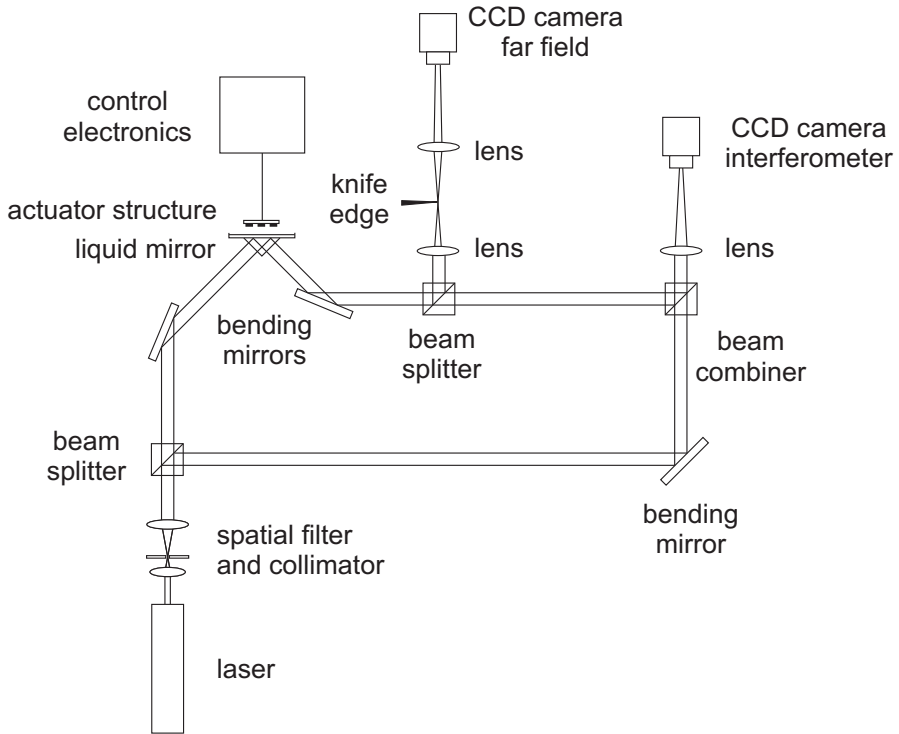
Figure 4.49: *Setup with the liquid mirror configured as a spatial light modulator.*

4.3.3   Measurements and results

Results of the spatial modulation are shown in figure 4.50. The left columns shows the actuator structure as it would be seen from above with the activated actuators shown in black. The central column shows the recorded far-field image and the right column shows the interferogram of the liquid surface.
Because of the grazing incidence of the light on the liquid mirror, the proportions of the right two columns are elongated in the direction of incidence, so that the measurements do not exactly match the actuator structure.

These results show that the liquid mirror in the Schlieren configuration can be used as spatial light modulator where the activation of single actuators results in the creation of a light spot in the observed far-field similar to a pixelated screen where individual pixels might be turned on and off. The center column of figure 4.50 nicely shows the effect of using the Schlieren method – obstruction of half of the spatial spectrum results in an elongation and a flaring of an ideally round spot in the direction perpendicular to the knife edge. In this particular
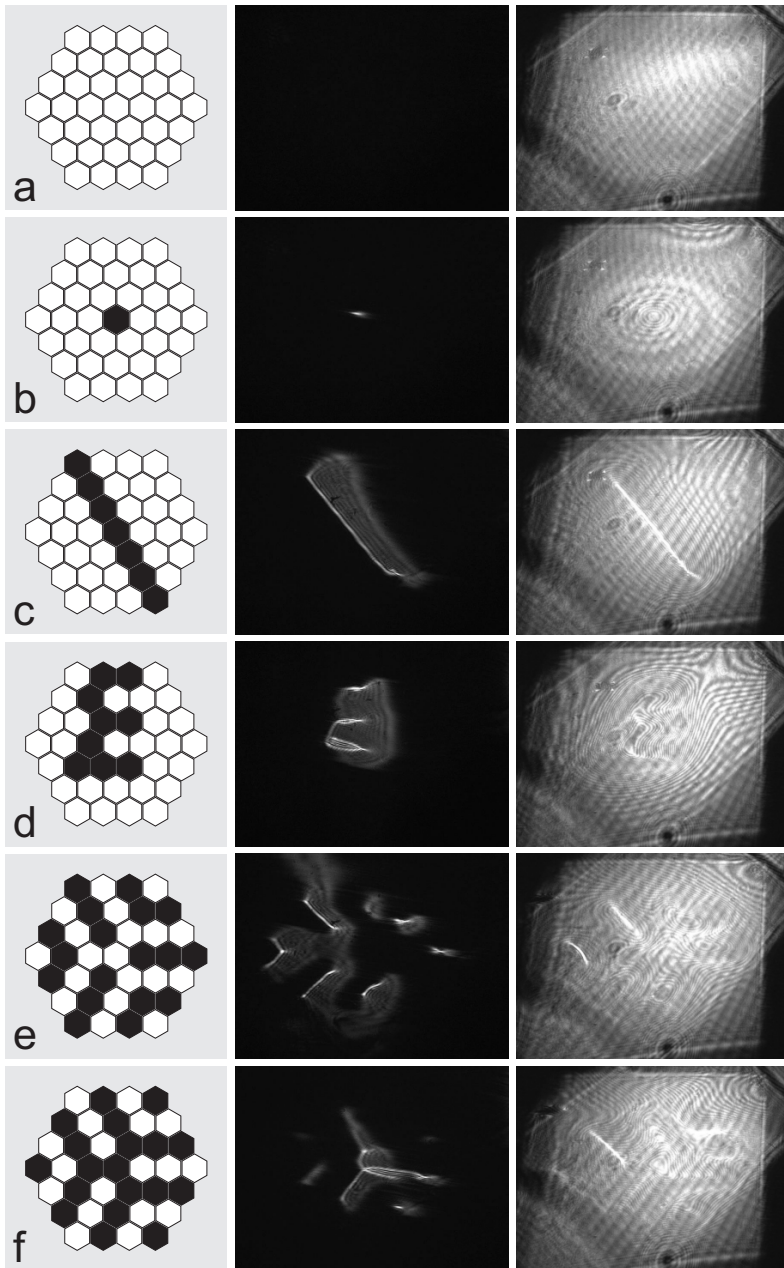
Figure 4.50: *Results of the spatial modulation with the liquid mirror: the left column shows the actuator structure with the activated actuators in black, the middle column shows the far field result, and the right column shows the interferogram of the liquid surface. The patterns shown here are: no actuators (a), a single actuator (b), a line (c), the letter "E" (d), all even numbered actuators (e), and all odd numbered actuators (f).*

configuration the direction corresponds to the direction of elongation caused by the grazing incidence of the beam on the mirror. Additionally, the diffraction caused by the knife edge can be observed in the flare, especially for the larger structures in rows c to f.

However, the use of the liquid mirror in this configuration implies certain differences as compared to a pixelated screen: row c in figure 4.50 shows that the line formed by the activated actuators does not consist of separate pixels, but is a continuous line. Also, row f shows three separate dots and three lines emanating from the center, while on the actuator structure double lines of actuators are activated.

These discrepancies stem from the properties of the liquid, i.e. here, the surface tension of the liquid prohibits the formation of fine structures smaller than the influence function of a single actuator (see also section 3.4.3.2 of the last chapter).

4.3.4 Discussion

Application of the liquid mirror as a spatial light modulator was demonstrated using the Schlieren method. It was shown that the liquid mirror can be used to create points, lines, and arbitrary patterns in the far field.

However, due to surface tension single adjacent points will form a continuous line, which will decrease the effective resolution of the liquid mirror.

> "Well, I should like to be a *little* larger, sir, if you wouldn't mind,"
> said Alice: "three inches is such a wretched height to be."
> "It's a very good height indeed!" said the Caterpillar angrily,
> rearing itself upright as it spoke (it was exactly three inches high).
>
> Lewis Carroll,
> *Alice's Adventures in Wonderland*, Penguin Books 1994.

Chapter 5

Scaling of the Liquid Mirror Device

One of the goals of this work was the verification of the claim that the dynamics and the influence function of the liquid mirror could be tuned through modification of the properties of the liquid (section 1.1) and in section 3.5.3 it was found that the characteristics of the liquid dynamics of the mirror depend on the geometry of the mirror and could be tuned by varying its design. In particular, it was believed that a shrinking of the thickness of the liquid layer would improve the frequency characteristic of the liquid mirror, i.e. decreasing the coupling of ambient vibrations to the liquid mirror and increasing the damping and so improving the signal to noise characteristic of the mirror.

At the same time, in section 3.4 it was speculated that the liquid mirror could be scaled to extremely large sizes to be used in future giant telescopes.

In this chapter, the size of the liquid mirror is scaled to verify these claims and determine the behavior of possible miniature and giant liquid mirrors.

5.1 Construction of a Large Area Liquid Mirror

Future groundbased telescopes with sizes of 30 m or larger require adaptive optical mirrors with thousands of actuators [1, 13, 133, 134]. It is estimated that

the 2.4 m adaptive M4- and 2.2 m by 2.7 m tipt/tilt M5-mirrors for the European Extremely Large Telescope (E-ELT) with a diameter of 39 m will cost about 50 M€ each (2012) [12].

One of the cost drivers is the need for a pristine reflective surface across the full area of the deformable mirror, which is increasingly difficult to obtain as the mirror size is scaled up. In contrast, the liquid mirror has a perfectly flat surface by default.

Here, a large area liquid mirror is realized and the possibility for a correction of large scale distortions is investigated.

5.1.1 Setup

The setup for the large area liquid mirror is shown in figure 5.1, it corresponds largely to the setup for the correction of wavefronts used in section 4.1.2. For the large scale liquid mirror an electrode structure with 70 actuators arranged in a rectangular grid (figures 5.2 and 5.2) was realized.
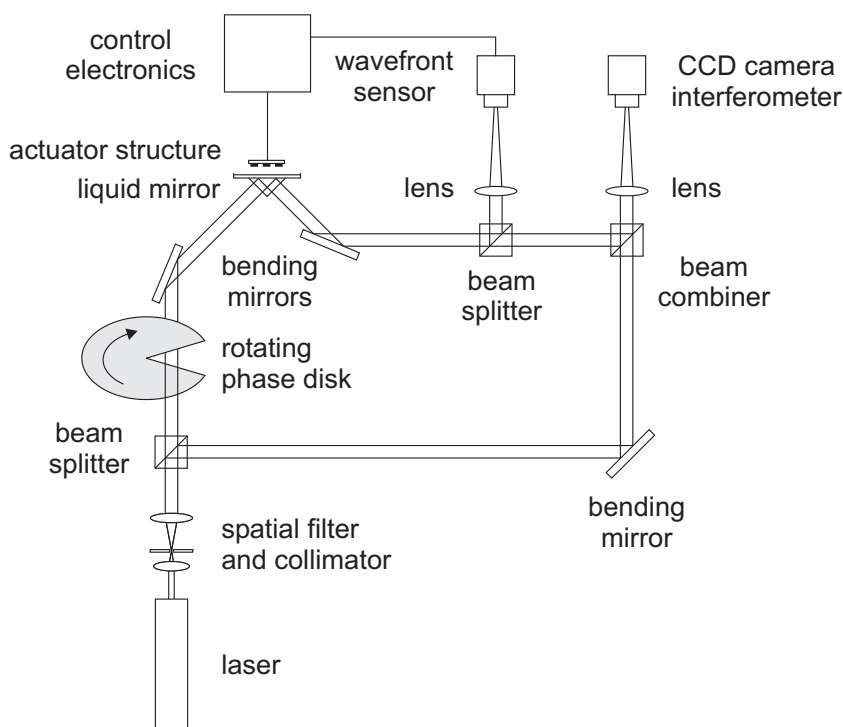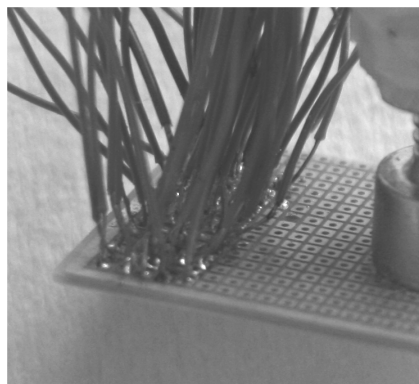

Figure 5.1: *Setup for the large scale liquid mirror.*
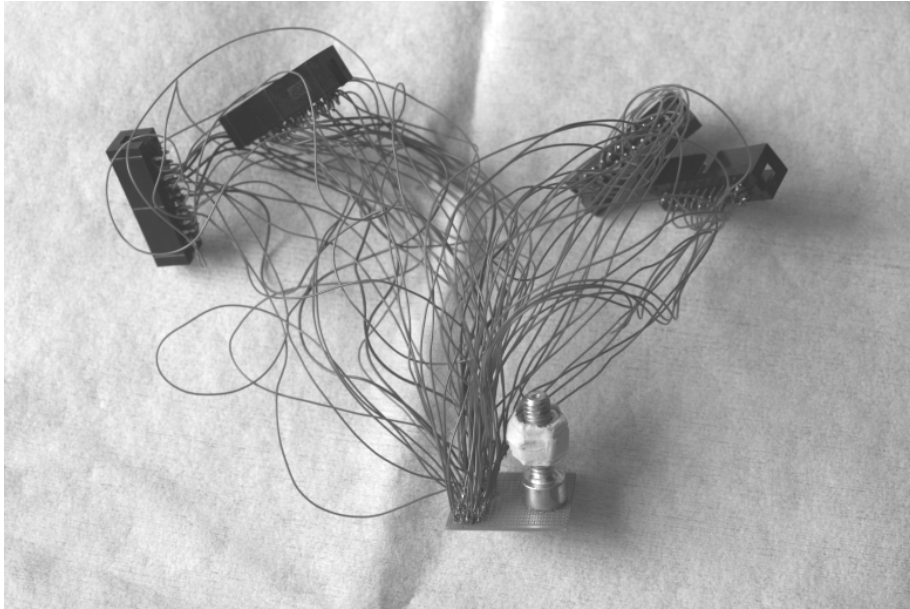
Figure 5.2: *Realization of the 70 actuator electrode structure. Wires connect the 70 electrodes in groups of 19 to four connectors that link the electrode to the high voltage amplifiers. The bolt attached to the board is used to position the electrode structure above the liquid surface.*


Figure 5.3: *Actuator structure of the large area liquid mirror (left) and detail of the electrode (right).*

The light of a HeNe-laser was split into two beams, of which one beam was aberrated by a rotating phase disk before it was directed to the liquid mirror to be corrected. The remaining part of the light was recombined with the corrected beam to form an interferometer. Behind the liquid mirror a part of the beam was directed onto a Shack-Hartmann type wavefront sensor with 127 subapertures.

The liquid used in the liquid mirror was an aqueous solution of 80% glycerin and the electrode structure used to apply a voltage and generate a static electric field to control the shape of the surface had 70 electrodes arranged in a rect6angular grid (figure 5.3) with dimensions of 1 mm squared each and overall dimensions of about 6.25 mm by 17.5 mm. The maximum voltage was $U = 380$ V and the distance between the actuators and the liquid surface was about $L = 800\,\mu$m, which resulted in a maximum stroke of about 6 μm (see figure 3.36 in section 3.4.3.2).

5.1.2   Measurements

Figure 5.4 shows the successful demonstration of the large scale mirror. The average residual rms-errors for the corrected and uncorrected wavefronts correspond to 0.38 μm and 1 μm, respectively, which results in an improvement factor of about 2.6.
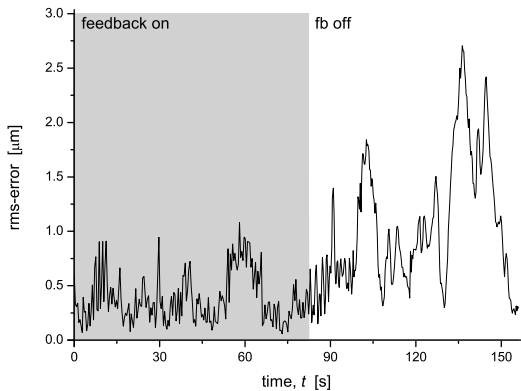
Figure 5.4: *Operation of the large scale mirror - during correction of the wavefronts (grey background color) the measured wavefront rms-error is significantly decreased.*
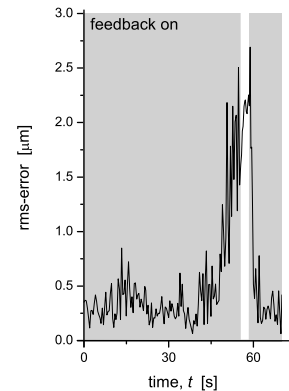
Figure 5.5: *Period of unstable behavior that could only be stopped by turning off the feedback and resetting the mirror.*

At one instance, it could be observed that the rms-error increased uncontrollably and the system became unstable. Once the large scale mirror exhibited this unstable behavior the feedback system was not able to recover itself – the feedback needed to be switched off and the mirror reset before re-establishing the feedback (see figure 5.5).

This unstable phase of the system was not caused by the Tonks-Frenkel instability (section 3.4.0.1) as the conditions for a stable regime were still fulfilled. The critical distance between electrode and liquid surface, d_c, is given by equation 3.8 and amounted in this case to $d_c = 475$ μm, which was well below the actual distance of about 800 μm.

The oscillations therefore were most likely caused by the interaction of the dynamics of the feedback system and random motion of the liquid surface, e.g. caused by the coupling of ambient vibrations to the liquid mirror (noise-waves) as described in section 4.1.5. Since the distance between electrode and liquid surface is larger for the large area liquid mirror, the maximum stroke of the system decreases, so that the signal-to-noise ratio of desired stroke to the amplitude of the noise-waves induced by random vibration decreases.
This means that the amplitude of the noise-waves approaches the maximum stroke of the system, so that the crest of a noise-wave may be interpreted by the system as an actuator at maximum stroke while a trough may be interpreted as an actuator at zero potential. In both cases the corrective action of the system will try to compensate these effects, but since both the crest and the trough of the noise-wave travel on, this may lead to an increase in the error.
Furthermore, the beam only overlaps with the center of the electrode structure, so that the electrodes at the edges (1 - 15 and 56 - 70, see figure 5.3) have no effect on the actual shape of the measured wavefronts.
Thus, these electrodes only interact with the noise-waves, which may lead to the introduction of additional errors that can travel into the area of the beam.
Under certain circumstances, depending on the delay time of the feedback system, the characteristics of the beam distortions, and the dynamics of the noise waves, this may lead to an amplification of the initially small noise-waves, such that the behavior of the entire system becomes unstable [135, 136].

5.1.3 Discussion

The liquid mirror was successfully scaled from 37 actuators to 70 actuators and applied to correct distorted wavefronts. An improvement factor of 2.6 was demonstrated.
The large area liquid mirror exhibited a phase of unstable dynamic behavior, which was not caused by the Tonks-Frenkel instability, but is speculated to be caused by the dynamics of the feedback system, in particular the interaction between the actuators at the edge of the electrode structure and waves due to ambient vibrations. If this system is optimized, i.e. when the shape and size of the electrode structure and the wavefront sensor are adapted to one another and to the optical beam, the performance and stability of the system should much improve. The observed instability does not put a principle limit on the size of the deformable mirror or the maximum number of actuators.

However, the size of the liquid surface and to a certain extent also the liquid depth scale with the size of the electrode, which will lead to longer wavelengths of the normal modes of the system and to a stronger coupling of ambient vibrations, thus increasing the probability of dynamic instabilities. The quadratic behavior of the maximum stroke (figure 3.36) will in turn require higher voltages to achieve a sufficiently large stroke, increasing the risk of the Tonks-Frenkel instabilities. This combination of effects suggests that the volume of the "sweet spot" in the parameter space of the control system, in which the large liquid mirror Adaptive Optics system is well behaved may progressively diminish with increasing size of the mirror. Consequently, for a liquid mirror with a size suitable for application in the E-ELT this implies that it is not clear, if a set of parameters for stable operation of the mirror can be found.

As the instability was observed only once, the behavior needs to be studied further as the scalability of the liquid mirror to hundreds and thousands of actuators awaits final confirmation.

5.2   Miniaturization of the Liquid Mirror

It was already illustrated in chapter 3 that use of the flexibility of a reflecting liquid surface promises to be a very useful tool when applied as a deformable mirror in Adaptive Optics. Likewise, the lack of rigidity might cause problems due to unwanted dynamics, if this is not accounted for in the design of the optical system, so that the dynamics of the liquid surface introduce larger errors to the optical system than the deformable mirror is able to correct in the first place.

The dynamic behavior of a liquid is determined on the large scale by gravity (gravity waves) and on the small scale by surface tension (capillary waves). Here, the resonant characteristics of the system are dominated by gravity (see chapter 3).

In order to reduce or eliminate the resonant behavior of the liquid while preserving the capability to electrostatically deform the surface and correct wavefront errors, the scale of the system may be reduced until gravity waves are no longer supported by the liquid layer. This miniaturization promises to suppress the dominant gravity waves and considerably reduce the errors introduced by ambient vibrations.
In the following sections the possibility of such a liquid micro mirror is explored and the boundary conditions and requirements for such a micro device are established.

5.2.1   Theory

The purpose of the miniaturization of the liquid mirror is to reduce the thickness of the liquid layer such that it is impossible for waves to propagate for any significant distance.

The rectangular base of a prism was used as a platform for the liquid layer. This could be approximated as a rectangular container with smooth walls, for which the normal modes are given by:

$$\omega_{ij}^2 = \left[g\,\zeta_{ij} + \frac{\gamma}{\rho}\,\zeta_{ij}^3 \right] \tanh\left(\zeta_{ij}\,h\right), \qquad (5.1)$$

where

$$\zeta_{ij} = 2\,\pi\,\sqrt{\frac{i^2}{L^2} + \frac{j^2}{\ell^2}}, \qquad (5.2)$$

with g the gravitational constant, γ the surface tension of the liquid, ρ the density of the liquid, h the fluid depth, i and j integers, and L and ℓ the dimensions of the container [95].

i j	glycerol		water	
	frequency f [Hz]	wavelength λ [m]	frequency f [Hz]	wavelength λ [m]
0 0	0	-	0	-
1 0	2.787	0.202	2.882	0.189
0 1	4.338	0.085	4.580	0.078
1 1	5.750	0.051	6.156	0.047
2 0	7.102	0.036	7.680	0.033
2 1	9.732	0.023	10.667	0.022
0 2	12.305	0.017	13.606	0.017
3 0	13.560	0.015	15.043	0.015
1 2	13.572	0.015	15.056	0.015
3 1	16.073	0.013	17.922	0.013

Table 5.1: *Frequency, f, and wavelength, λ, of the lowest ten modes for a rectangular geometry and a liquid depth of $h = 500\,\mu$m for an aqueous solution of 80% glycerol (left) and water (right).*

The corresponding wavelength may be computed with equations 3.20 and 3.21. The liquid was applied directly to the prism without using a container to prevent the formation of a meniscus at the container walls. For very thin liquid layers the results of equations 5.1 and 3.21 were relatively insensitive to the properties of the liquid, viz. surface tension and density. Contrariwise, the results depended strongly on the thickness of the liquid layer.

An estimate of the normal modes is given by equation 5.1: table 5.1 summarizes the first ten modes for the prism with dimensions of $L = 28.3$ mm and $\ell = 20$ mm and a liquid depth of $h = 500\,\mu$m.

In order to obtain a thin liquid layer of homogeneous thickness, the surface of the coupling prism was specially treated to increase the surface area and to prevent dewetting at the solid-liquid interface.

5.2.2   Etching of the Prism

At the length scale of the capillary constant, the effects of surface tension will be comparable to the effects of gravity (see section 3.4).
For both water and the aqueous solution of 80% glycerol the capillary constant is of the order of about $3 - 4$ mm, which means that the behavior of the liquid layer with a depth of about $700\,\mu$m will be dominated by surface tension. This leads to effects of dewetting, which may include discontinuities in liquid layer due to contaminants or defects of the glass surface, which makes the surface unsuitable for the use of the wavefront correction.

An even spreading of the liquid on the glass surface can be obtained when the surface tension, or surface free energy of the solid-air interface, γ_{SA}, is larger than the sum of the surface tension of the solid-liquid and liquid-air interfaces, or $\gamma_{SA} - \gamma_{SL} - \gamma_{LA} > 0$ [137].

Several methods can be applied for the manipulation of the surface tensions of a solid-liquid system:

- wetting agents,

- self-assembling monolayers (SAM),

- microstructuring of the surface, and

- etching of the surface.

Wetting agents are chemicals that are either added to the liquid or applied to the solid surface that alter the surface tension [138, 139], while SAM are organic molecules that adsorb to the solid surface and slowly organize themselves into a single layer [140, 141]. However, the use of chemicals might not only change the surface properties, but might also negatively impact the bulk properties of the liquid (e.g. the use of detergent to lower the surface tension may lead to foaming, rendering the liquid surface unusable for reflection).

Mechanical treatment of the surface has no influence on the properties of the liquid, so that the optical and dynamical characteristics of the liquid system are preserved. Through the creation of microstructures on the surface, its wetting properties may be tailored to specific needs. The microstructures are generally realized in the form of fibers or pillars, which may themselves have a structured or porous surface [137, 142–145]. Etching of the surface may result in two effects, viz. the rigorous cleaning of the surface, removing organic contaminants that may affect the properties of the surface [137, 146], and, if differently applied, cleaning is replaced by etching, from which a roughening of the surface can result [147]. This roughening increases the surface area and alters the properties of the surface such that a better wetting behavior is obtained [137, 148–150].

Here, the surface was etched with hydrofluoric acid (HF) to increase the wetting of the surface. Figure 5.6 shows the effect of the etching of the glass on the wetting behavior of an aqueous solution of 80% glycerol on the etched surface.

Images A to C nicely show the increase of the wetting after different times of etching with an aqueous solutions of 73% HF. Figure D shows that the optimum surface roughness is obtained after 40 seconds and that longer etching does not increase the wetting any further. Figures E and F show that an increase of the wetting can also be obtained with a considerable lower concentration of HF, although longer times of immersion were necessary.
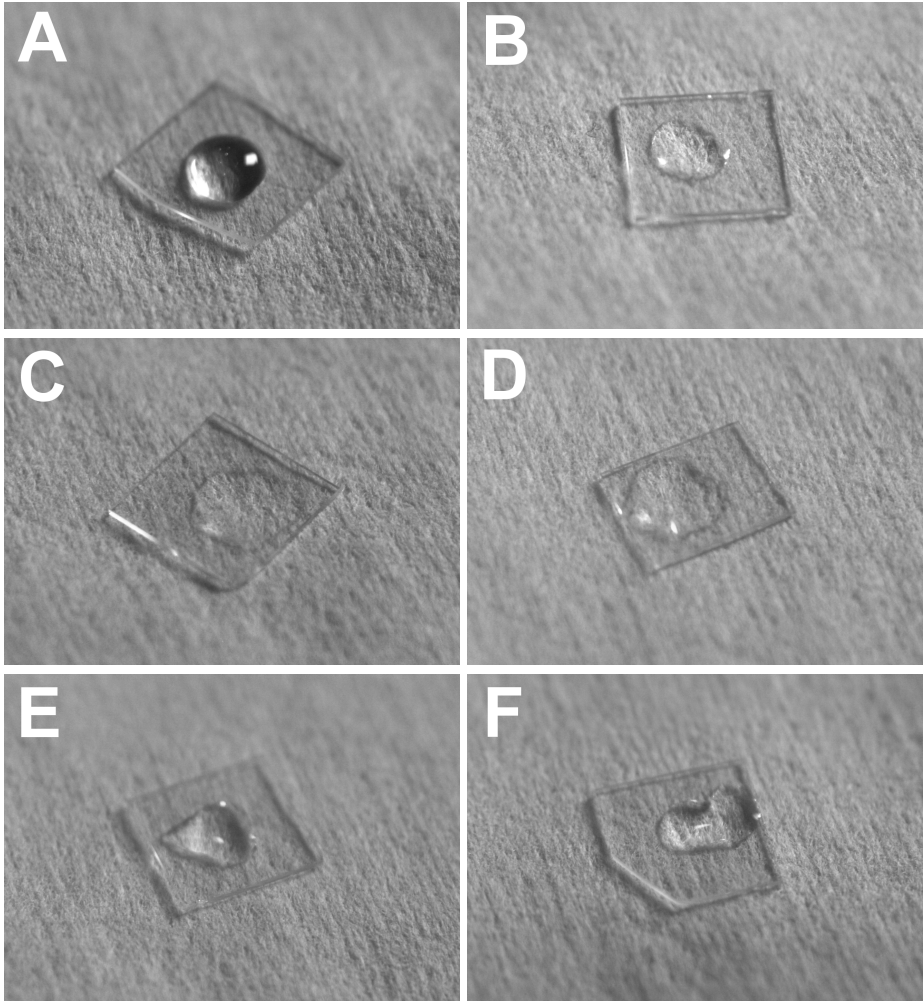
Figure 5.6: *Wetting behavior of an aqueous solution of 80% glycerol on the etched surface of a piece of glass. The etching was performed with aqueous solutions of 73% hydrofluoric acid (HF) (B - D) and 0.55% HF (E, F) for different times. A: untreated surface, B: 20 s of 73% HF, C: 40 s of 73% HF, D: 60 s of 73% HF, E: 120 s of 0.55% HF, and F: 600 s of 0.55% HF.*

Because of the inherent risks involved in handling HF at high concentration, the diluted solution of HF was chosen for the treatment of the BK7 glass prism. This allowed the liquid so spread thinly on the surface and form a very thin liquid film with a thickness of a few 100 μm.

5.2.3 Setup

The liquid micro mirror is shown in figure 5.7, the hypothenuse surface of the prism had dimensions of $L = 28.3$ mm and $\ell = 20$ mm. The setup of section 3.4.3.1 was used to characterize its characteristics with thin liquid films with thicknesses of $h < 1$ mm.
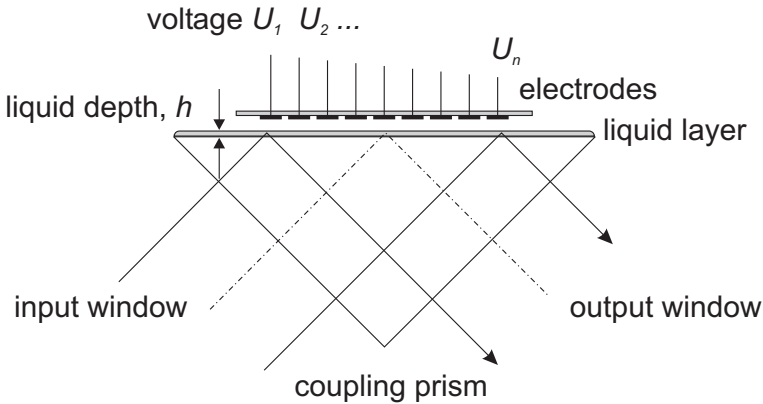
Figure 5.7: *The liquid micro mirror.*

5.2.4 Characterization of the micro mirror

As for the regular liquid mirror the properties of the liquid micro mirror were investigated for a thin film of an aqueous solution of 80% glycerol and additionally for water. While the thin liquid layer improves a number of the dynamic properties of the mirror, it also introduces new challenges: due to the large surface to volume ration of the liquid body, the liquid evaporates quickly and needs to be replenished in order to prevent a partial and subsequently total dewetting of the surface. The time required for the evaporation of the liquid layer is lower for water than for glycerol and is on the order of tens of minutes depending on ambient conditions.

5.2.4.1 Frequency response

Figure 5.8 shows the frequency response of the micro mirror with a thin layer of an aqueous solution of 80% glycerol (top) and water (bottom). The layer thickness

was estimated to be about $500\,\mu$m in both cases. The measured voltages were normalized such that the DC gain of the system equals unity, i.e. $G_{\mathrm{DC}} = 1 = 0$ dB.

For the aqueous solution of 80% glycerol the response of the system shows a constant decrease with a slope of about -15 dB/decade with resonances at 10 and 25 Hz. The resonance at 10 Hz corresponds to the mode $i = 2, j = 1$, which is the first mode the wavelength of which fits fully into the long side of the prism (compare table 5.1). The gain crossover frequency and the phase crossover frequency of the system are given by $f_{\mathrm{gc}} = 1$ Hz and $f_{\mathrm{pc}} = 1.7$ Hz, respectively, which leads to a gain margin of $GM = 4$ dB and a phase margin of $PM = 106\,^\circ$, which fulfills the stability criteria for a feedback system (compare section 3.5.2 and [102]).

The frequency response of water is relatively flat up to a frequency of about 6 Hz, after which the amplitude drops with a slope of about -25 dB/decade with resonances at 11, 18 and 25 Hz. The resonances at 11 and 18 Hz correspond to the modes with $i = 2, j = 1$ and $i = 3, j = 1$, respectively. Similar to the response of glycerol these are the first modes, the wavelengths of which fit once and twice into the long side of the prism, respectively. The gain crossover frequency and the phase crossover frequency of the system are given by $f_{\mathrm{gc}} = 6$ Hz and $f_{\mathrm{pc}} = 12$ Hz, respectively, which leads to a gain margin of $GM = 14$ dB and a phase margin of $PM = 162\,^\circ$. Here, the stability criteria are also fulfilled.

Figure 5.9 shows the open-loop response of the liquid micro mirror to ambient vibrations as fourier spectra of an aqueous solution of 80% glycerol (left) and water (right). Both graphs show no major excited modes, which indicates that the micro mirror is indeed insensitive to mechanical excitation from ambient vibrations.

### 5.2.4.2   Damping and time constants

The damping of the excited surface of the thin liquid layer as response to a mechanical impulse for an aqueous solution of 80% glycerol (left) and water (right) is shown in figure 5.10.

The damping times for the free surfaces of the thin liquid layer of the aqueous solution of 80% glycerol and water were measured as $\tau_{\mathrm{gly}} = 0.104 \pm 0.019$ s and $\tau_{\mathrm{water}} = 0.074 \pm 0.012$ s, respectively.
The excitations are damped stronger in water, although the viscosity of water ($\eta_{water} = 1.0$ mPa s) is much lower than that of the glycerol solution ($\eta_{gly} = 59.9$ mPa s), which would suggest that the excitations should be supported much longer.
Similar to the resonance frequencies (see equation 5.1), the amount of damping depends strongly on the liquid layer thickness. This suggests that the lower vis-
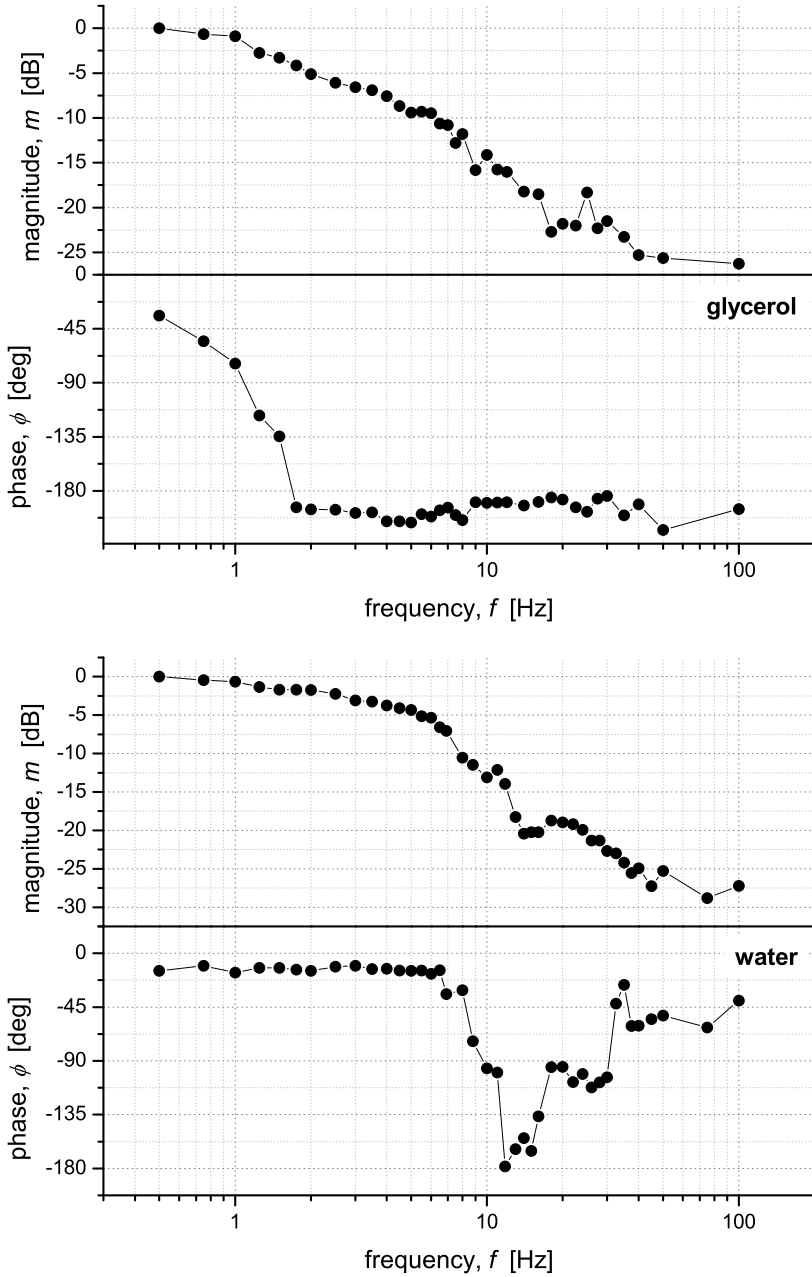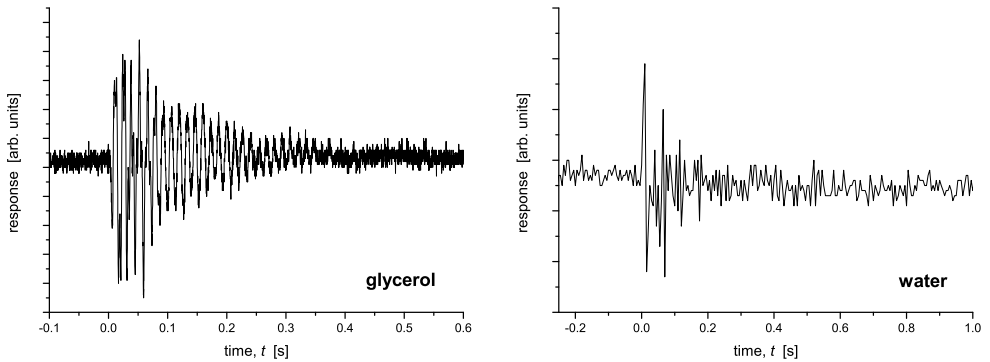
Figure 5.8: *Frequency response of the liquid micro mirror with a thin layer of an aqueous solution of 80% glycerol (top) and water (bottom).*
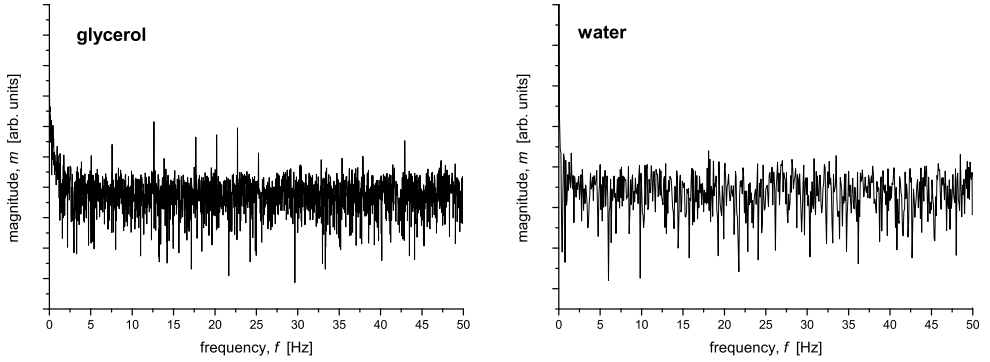
Figure 5.9: *Open-loop response of the liquid micro mirror to ambient excitations as a Fourier spectrum in the frequency domain for an aqueous solution of 80% glycerol (left) and water (right).*

Figure 5.10: *Damping of surface excitations from a mechanical impulse in thin liquid layers of an aqueous solution of 80% glycerol (left) and water (right).*

cosity of water allows it to spread more easily and form a much thinner film on the surface of the glass than the glycerol.

This has also been observed for the rise and relaxation times which are shown in figure 5.11.
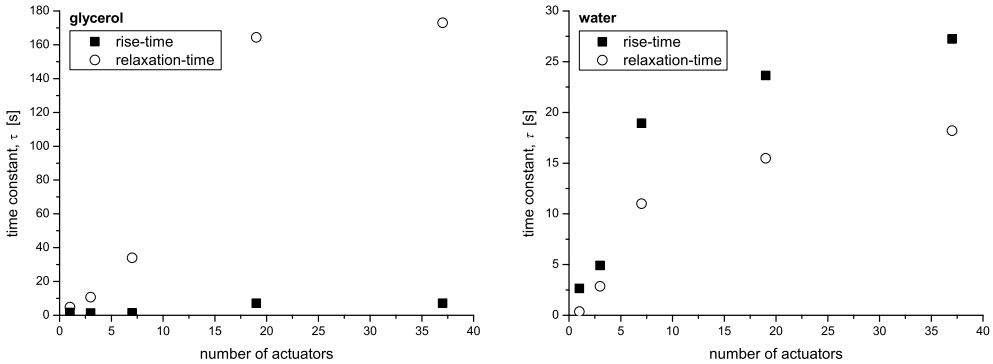
Figure 5.11: *Rise and relaxation time constants as a function of the number of actuators for a thin layer of an aqueous solution of 80% glycerol (left) and water (right).*

Both the rise- and relaxation times of the thin film of water and glycerol are much larger than for the deep glycerol as the total area through which the liquid can flow towards the pulling force of the electrode is limited by the thickness of the liquid layer. For water the rise- and relaxation-times are of comparable magnitude, while the thin film of glycerol shows a large difference, the relaxation times of the order of greater than 2 minutes make the thin film of glycerol unsuitable for the use in an Adaptive Optics system.

For small numbers of actuators the rise- and relaxation times behave according to equation 3.25 – however, for larger numbers of actuators the rise of the liquid is limited by the total amount of liquid, since there is no reservoir from which liquid can be drawn as with the liquid container in the case of the deep glycerol. For water this limit is at a number of about 7 actuators, while for glycerol this is at about 19 actuators, supporting the thesis that the layer thickness of water is smaller than that of the glycerol solution.

5.2.5   Further Development of the Micro Mirror

The measurements with the liquid micro mirror have shown that the reduction of the liquid layer thickness effectively prevents the coupling of ambient vibrations

to the normal modes of the liquid system. Furthermore, the thin liquid film successfully damps excitations of the surface.

However, through the careful tuning of the properties of the liquid and the electrodes, the characteristics of the micro mirror may be further improved.

5.2.5.1   Optimizing the Influence Function

The width, w, of a deformation of a liquid surface shaped by an electrostatic field is given by:

$$w = a + b_1 \cdot r + b_2 \cdot \rho + b_3 \cdot r \cdot \rho + (c_1 + c_2 \cdot r + c_3 \cdot \rho + c_4 \cdot r \cdot \rho) \cdot \sqrt{\frac{\gamma}{\rho \cdot g}}, \quad (5.3)$$

with r the effective radius of the electrode, ρ the density of the liquid, γ the surface tension, g the gravitational constant, and a, b_n and c_n constants [83]. An effective actuator radius of about $r_{\text{eff}} = 25$ μm is a reasonable assumption for the actuator structure of the liquid micro mirror. With this value equation 5.3 reduces for water with $\rho = 998.2 \, \text{kg/m}^3$ to:

$$w = a_1 + a_2 \cdot \sqrt{\gamma}, \quad (5.4)$$

with $a_1 = 2.508 \cdot 10^{-4}$ m and $a_2 = 3.807 \cdot 10^{-3}$ $\sqrt{\text{m}^3/\text{N}}$, so that for water with $\gamma = 0.073$ N/m the width of the influence function comes to: $w_{water} = 1.28$ mm. With the addition of surfactants the surface tension and thus the width of the influence function may be reduced even further.

A possible electrode structure for the liquid micro mirror is shown in figure 5.12. It would be able to accommodate 100 electrodes on a surface area of 5 mm by 5 mm having a greatly reduced footprint while maintaining a maximum stroke of the order of 10 μm.

5.2.5.2   Optimizing the Glass Substrate

In section 5.2.2 it was shown that the surface of the glass could be modified to increase the wetting of the liquid. By optimizing the wettability through etching or micro structuring the surface the liquid layer thickness may be further optimized. Additionally, smaller dimensions of the liquid surface lead through equation 5.2 to a further increase in the frequency of the normal modes. Since ambient vibrations are often low frequency building vibrations, this promises a further reduction of the coupling to the normal modes.

Due to the small volume of liquid the dynamic range of the mirror is limited. This could be improved through the addition of a reservoir connected to the liquid layer that does not extend the size of the glass determining the resonance
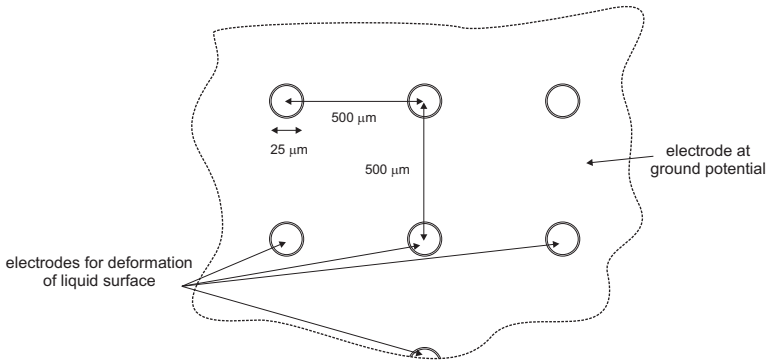
Figure 5.12: *Geometry of a flat electrode for the liquid micro mirror (not to scale). The individual electrodes are at a potential U_n to shape the liquid surface while the surrounding large electrode is at ground potential to prevent the individual fields from fringing (compare section 3.4.2).*

frequencies (see note above) – any oscillations excited in the reservoir would be quickly damped when coupled to the liquid layer.

5.2.5.3   Optimizing the Liquid Properties

The performance of the liquid may be further improved through the choice or the engineering of a liquid with optimized properties:

- While the distribution of the normal modes (equation 5.1) depends strongly on the thickness of the liquid layer and much less on the material properties of the liquid, the thickness and smoothness of the liquid layer depend strongly on the viscosity of the liquid, since a less viscous fluid spreads more easily and evenly on the surface and may form a thinner liquid layer.

- Due to the limited volume the flow of the liquid is reduced, which leads to an increase of the response times and a decrease in effective bandwidth (figures 5.8 and 5.11). A less viscous fluid may flow more easily through the limited volume and lower the time constants.

- The width of the influence function (equation 5.3) depends both on the density and the surface tension of the liquid. Lower density and surface tension allow for a smaller width of the deformation and thus a higher resolution of the device.

- The electrostatic force that acts on the liquid surface has to balance the surface tension and the gravitational force, which both act counter to it. While the precise shape of the deformation depends both on the surface tension

and the gravitational force, the maximum stroke is inversely dependent on the density of the fluid and may be increased for a less dense liquid [21].

- Since there is only a very small liquid volume, evaporation of the liquid may become an issue, so that the fluid should have a low vapor pressure.

- In order to facilitate the use of the micro mirror in a wide range of adaptive optical applications the liquid should be transparent over a wide range of wavelengths.

While the liquids used for the measurements presented here may not be the ideal fluids to operate the liquid micro mirror with, the above list describes the physical properties the ideal liquid should combine to enable an optimal operation of the liquid micro mirror.

While Ethanol does not fulfill the requirement of low vapor pressure, it is transparent and exhibits improved properties with respect to water or glycerol: ethanol has a density of $\rho_{\text{ethanol}} = 789$ kg/m^3, a surface tension of $\gamma_{\text{ethanol}} = 22.1$ mN/m, and a viscosity of $\eta_{\text{ethanol}} = 1.52 \cdot 10^{-3}$ mPa s, which would result in a width of the influence function of about $w_{\text{ethanol}} = 0.88$ mm.

This shows that even more suitable liquids may exist or may be engineered for the operation of the liquid micro mirror.

5.2.6 Discussion

Through reduction of the dimensions of the liquid mirror system a liquid micro mirror was successfully realized. A method to increase the wetting of the glass surface through etching in order to allow for a decrease of the liquid film thickness was demonstrated. The dynamic characteristics of the micro mirror were investigated with water and an aqueous solution of 80% glycerol.

Reduction of the thickness of the liquid layer successfully changed the normal mode structure of the liquid system such that the coupling of ambient vibrations to the liquid was effectively inhibited. The reduction furthermore increased damping of oscillations in the liquid layer, so that excitations that did couple to the liquid decayed quickly.

However, the reduction of the liquid layer also reduced the total amount of fluid and the effective area through which the liquid could flow, which resulted in a decrease of the available bandwidth to about 1.5 Hz for the aqueous solution of glycerol and 3 Hz for water and to an increase of the time constants of the mirror system. This effect was especially marked for glycerol which exhibits a slow component for the relaxation-time that makes it unsuitable for use in any dynamic Adaptive Optics system.

Suggestions for the further improvement of the liquid micro mirror and the properties of the liquid were derived and an improved electrode structure proposed.

"Things are never quite the way they seem."

Stan Ridgway,
Camouflage, from the album "The Big Heat," I.R.S. records 1986.

Chapter 6

Conclusions and Recommendations

6.1 Conclusions

The goal of this thesis as stated in chapter 1 was the demonstration of the functionality of the liquid mirror for Adaptive Optics, of which the theoretical background was described in chapter 2, the exploration of its characteristics, and the further development of its capabilities.

6.1.1 Liquid Dynamics

In chapter 3 it was found that the physical properties of an aqueous solution of 80% glycerol best match the requirements for the liquid mirror. It was shown that in the parameter space of the liquid mirror system a stable region exists, in which the mirror may be operated without occurrence of the Tonks-Frenkel instability. The best actuator structure was shown to consist of planar circular electrodes set inside a grounded electrode, for which the influence function, i.e. the radius of the liquid deformation was determined to mainly depend linearly on the radius of the actuator. The maximum amplitude of the liquid deformation was shown to be $u_{\max} \approx 155 \ \mu$m, where the effective voltage at the liquid surface was only about a third of the nominal value.

The liquid deformation was measured to have a FWHM value of $w_{\text{meas}} \approx 2.9$ mm where the simulation predicted a value of $w_{\text{theo}} = 2.8$ mm. Similarly the effective voltage at the liquid surface was determined to be $U_{\text{eff, meas}} = 97$ V while the simulations predict $U_{\text{eff, theo}} \approx 100$ V, showing that measurement and simulations are in good agreement. However, it was also found that the maximum amplitude of the deformation depends on the surface tension of the liquid – contrary to equations 3.5 and 3.16. This implies that the equations are incomplete and need to be revised.

Characterization of the dynamic system determined the liquid mirror to be a higher order transfer function with the symmetric 01-mode at 4.6 Hz as the main resonance. The open-loop frequency response showed the 3 dB bandwidth to be about 100 Hz and the gain crossover frequency and the phase crossover frequency of the system to be $f_{\text{gc}} = 27$ Hz and $f_{\text{pc}} = 115$ Hz, respectively. This leads to a gain margin of $GM = 11.4$ dB and a phase margin of $PM = 140\,^{\circ}$ with which the stability criteria for a feedback system are fulfilled.

It was shown that the time constants for deforming and releasing the liquid surface as a function of the number of actuators exhibit an exponential behavior. Excitations of the liquid surface couple mainly to the fundamental mode and decay with a characteristic damping time of $\tau_{\text{free}} = 1.27$ s for the free surface, which agrees well with the predicted value of $\tau_{\text{theo}} = 1.36$ s, and of $\tau_{\text{fb}} = 1.10$ s for the actively controlled surface.

6.1.2   Liquid Mirror Performance

The work of chapter 4 demonstrated that the liquid mirror may be applied as a wavefront corrector. It was shown that the improvement of aberrated wavefronts in terms of rms-error is a more useful measure of the wavefront correction than in terms of the Strehl ratio. The amount of wavefront correction that could be obtained was observed to depend on the parameters of the feedback system and the strength of the aberrations. For static and dynamic aberrations the improvement of the wavefront in terms of rms-error were measured to be as high as $I_{\text{rms, static}} = 12$ and $I_{\text{rms, dynamic}} = 4.5$. Modal analysis of the results showed that ambient vibrations mainly excite the tip and tilt modes. While it was demonstrated that the liquid mirror is most effective for correction of lower order modes, it was also shown that the liquid mirror changes the dynamics of the system rather than fully correcting the ambient vibrations. This change in dynamics manifests itself in a higher damping and a shift of the normal modes of the system to higher frequencies.

The improvement of image sharpness by the liquid mirror was demonstrated in a fine imaging setup. A comparative analysis of different image sharpness metrics showed that the spatial frequencies metric should be the most sensitive to the improvement of image sharpness in theory, while measurements showed that the global or local information metric worked best with the liquid mirror data (this can already be observed in figure 4.43). No direct correlation between wavefront

error and apparent image sharpness was found, since the systematic errors of the setup including the influence of the tilt of the liquid mirror with respect to the conjugate plane were not removed. Additionally, the effects of the tip and tilt modes are not considered by the sharpness metrics, but do significantly contribute to the wavefront error.

The application of the liquid mirror as a spatial light modulator was shown through demonstration of the creation of points, lines, and arbitrary structures. The resolution of the liquid mirror in this case is limited by the liquid properties of the mirror, since surface tension will cause two separate large structures to merge and appear as a single structure.

6.1.3   Mirror Scaling

In chapter 5 the scaling of the liquid mirror to larger and smaller sizes was successfully demonstrated. For a rectangular actuator structure with 70 actuators an improvement factor of 2.6 was measured. Due to the increased size of the actuator structure and adjusted physical parameters the liquid mirror showed instable behavior. The instable behavior cannot be attributed to the Tonks-Frenkel instability, which suggests that a large scale liquid mirror is possible when the physical parameters of the liquid mirror and the dynamics of the feedback system are adjusted for the larger size of the actuator structure.

The reduction of the surface area of the liquid and the liquid layer to about 500 μm effectively inhibited the coupling of ambient vibrations to the liquid layer both for water and an aqueous solution of 80% glycerol. It was found that the liquid micro mirror works best with a thin layer of water. Damping times were reduced and shown to be about 0.075 s and 0.1 s, respectively. This change in the liquid dynamics was also reflected in the available bandwidth, which was shown to be about 1.5 Hz for the aqueous solution of glycerol and 3 Hz for water, compared to about 100 Hz for the aqueous solution of glycerol for the regular sized liquid mirror.

6.1.4   Main Conclusions

Revisiting the initial advantages that were quoted in the outline (see section 1.1), the work of this thesis allows the following conclusions:

1. large surface displacements with relatively low applied voltages;
   confirmed: with a voltage of 380 V, surface displacements of up to 13 μm could reliably be measured (see section 3.4.3.2) - however, much higher displacements estimated to be larger than 100 μm could be observed, but not measured, since the interference fringes could no longer be resolved,

2. possibility of a large number of actuators;
   confirmed: this has been confirmed in section 5.1,

3. possibility of adjustment of the dynamics and the influence function through modification of the physical properties of the liquid;
partly confirmed: this has been confirmed in sections 3.3 and 5.2 - however, the development of the liquid micro mirror has shown that modification of the physical properties of the liquid container, i.e. size and thickness of the liquid layer, has not only a much larger effect on the normal modes of the system, but also a larger effect on the dynamic properties of the liquid mirror,

4. simple design without the need for sophisticated technology;
confirmed: the liquid mirror consisted of a customized printed circuit board (PCB) with an electrode structure ($\sim$ 5 €), a prism ($\sim$ 70 €), a liquid container, in which the prism was mounted ($\sim$ 4 €), and the liquid ($\sim$ 1 €), so that the total cost of the liquid mirror is below 100 €,

5. and close to 100% reflectivity for a broad wavelength range;
plausible: an investigation of the wavelength dependence was not part of the work, but if a clear liquid is used in combination with a prism with a broadband antireflection coating, no absorption and close to 100% reflectivity may be expected for the visible spectrum and near infrared (NIR) - the use of a custom liquid optimized to have low absorption in the IR and special optics and coatings may expand the range of the liquid mirror further into the IR.

The main conclusions of this thesis are:

- The liquid mirror was successfully applied for wavefront correction, fine-imaging, and spatial light modulation. Stable operation has been demonstrated for the correction of static and dynamic aberrations.

- The physical and dynamic characteristics of the liquid mirror system were determined. It was found that the theory for the liquid deformation is incomplete, in particular it was found that in contrast to theory the maximum amplitude of the liquid deformation depends on the surface tension of the liquid. Further work is needed to fully understand and describe the liquid mirror system.

- The shaping of the liquid surface for use as a deformable mirror was successfully demonstrated. With strokes greater than 100 μm the liquid mirror compares favorably with piezoelectric mirrors or even giant voice coil mirrors (see table 6.1). Its bandwidth of about 80 Hz is of the same order of magnitude as LC SLMs and close to the bandwidth of bimorph mirrors. With around 100 actuators the liquid mirror is comparable to the bulk of piezoelectric, bimorph, and membrane mirrors, while the definite proof of the scalability to a great number of actuators remains open. The average

residual rms-error for the correction of static aberrations is about 0.07 μm, which corresponds to about 13.7% residual aberrations. For comparison, equivalent 37-channel membrane and piezoelectric mirrors have 9.7% and 9.0% residual aberrations, respectively [2]. This shows that the surface accuracy of the liquid mirror is comparable to existing technology and might even be further improved with better isolation from ambient vibrations. The liquid mirror has a very simple design and no sophisticated technology, which makes it easy to operate and maintain. Furthermore, at a cost of less than 100 € it costs only a fraction of even the lowest cost deformable mirror of any other type, which is a few k€.

mirror type	stroke	size	number of actuators	bandwidth	complexity	cost
	[μm]			[Hz]		
piezoelectric	10	m	1000s	1000	very high	k€
bimorph	10	cm	100s	100	high	k€
membrane	1	cm	10s	1000	medium	k€
MEMS	1	mm	1000s	1000	high	k€
voice coil	100	m	1000s	1000	very high	M€
LC SLM	10	cm	1000s	1000	medium	k€
liquid	**100**	**cm**	**10s**	**100**	**low**	**< 100 €**
E-ELT requirement	70-80	-	1000s	80	-	-

Table 6.1: *Comparison of different deformable mirror types and the requirements for the E-ELT [1, 3].*

- The influence of ambient vibrations on the liquid mirror were investigated. It was observed that this affected particularly the tip and tilt modes of the current implementation of the liquid mirror. Correction of these ambient vibrations manifests itself rather through a change of the dynamics of the liquid mirror system than a full compensation of the aberrations.

- The liquid mirror was successfully scaled to larger and smaller dimensions. The up-scaled model was applied as a wavefront corrector but exhibited a phase of unstable behavior. It is believed that this is caused by the dynamics of the system and presents no fundamental obstacle to further scaling of the liquid mirror. However, the parameter space within which the liquid mirror system is well-behaved is located between the dynamic and Tonks-Frenkel instabilities and it remains to be proven that even larger liquid mirrors may be operated there. While the stroke and the bandwidth fulfill

the requirements of the E-ELT deformable mirror (table 6.1) and implementation of a liquid mirror with a few hundred actuators seems realistic, stable operation of a liquid mirror with a few thousand actuators remains to be demonstrated. If this can be accomplished, the liquid mirror is a possible candidate for application in a project like the E-ELT.

The characteristics of the liquid micro-mirror were successfully determined and it could be shown that the reduction of the layer thickness effectively inhibits the coupling of ambient vibrations to the liquid layer. While this reduces the noise in the system it also reduces the bandwidth, which limits the number of practical applications for the micro-mirror. This suggests the application of the micro-mirror in quasi-static or slowly varying systems that require a large stroke, e.g. in Ophthalmology.

6.2   Recommendations

The work presented in this thesis has focused on the characterization of the liquid mirror, both the dynamics of the liquid system and the use of the liquid mirror in different adaptive optical applications. The application of the liquid mirror as a wavefront corrector, fine imager, and spatial light modulator was successfully demonstrated, but only as a wavefront corrector a satisfactory performance was obtained. Scaling of the liquid mirror device was successfully implemented to larger and smaller dimensions. However, the large liquid mirror was shown to need further confirmation of the scalability to very large numbers of actuators.

Based on these findings the following research for the improvement of the liquid mirror is suggested:

- It was stated (sections 1.1 and 3) that the strength of the liquid mirror lies in the fact that it can freely shape the liquid surface and is not bound by the solid state properties of the mirror surface. I propose to take this principle one step further and completely abandon the two-dimensional actuator structure in favor of a three-dimensionally controlled static electric field. The goal is to fully control the shape of the liquid surface independent of the current limits imposed by the physical properties of the liquid.

- The properties of the liquid mirror, i.e. the use of a liquid, the application of the principle of total internal reflection, and the physical decoupling of the actuator structure from the liquid surface, indicate that the liquid mirror has very good thermal properties under high laser loads. This suggests further research of the liquid mirror for high-power laser applications. The thermal properties of the mirror may be further optimized by circulation of the liquid to remove the heat from the liquid layer.

- Demonstration of the suitability of the liquid mirror for large-scale applications by first scaling the mirror to a few hundred actuators and in a second

step to a few thousand actuators. This includes an implementation of the decoupling of the liquid layer from ambient vibrations and the investigation of the available parameter space for a stable operation of the system that meets both the requirements of the dynamic stability criteria due to the parameters of liquid mirror and feedback system and the Tonks-Frenkel instability.

- The liquid micro mirror is already very well decoupled from ambient vibrations and should therefore be able to very accurately shape static wavefronts. Because of its limited bandwidth, however, it is currently not suited for the correction of dynamic wavefronts. Further research is proposed to develop a micro mirror with increased bandwidth to combine its vibration isolation properties with the bandwidth of the regular liquid mirror. Possible lines of research include the use of a reservoir to provide more liquid in a shorter time for the micro mirror, the use of a system of baffles in the liquid container to suppress surface waves, or the substitution of a liquid for an elastic, gel-like substance that does not rely on the actual flow of material.

- Development of the liquid or micro mirror for use in quasi-static or slowly varying applications that require large stroke, e.g. vision science. Ophthalmology requires deformable mirrors with strokes of more than 10 μm, about 100 actuators, and bandwidths of about 30 Hz [151] and could benefit from a low-cost, low-tech deformable mirror like the liquid mirror. Another application is the compensation of aberrations caused by thermal effects in optical systems, as thermal effects generally vary slowly.

Bibliography

[1] Madec, P.Y., "Overview of deformable mirror technologies for adaptive optics and astronomy," in "Adaptive Optics Systems III," volume 8447 of *Proc. SPIE*, 844705 – 844705–18, 2012.

[2] Vdovin, G., Soloviev, O., Loktev, M., *et al.*, eds., *OKO Guide to Adaptive Optics*, fourth edition, Flexible Optical B.V., Polakweg 10-11, 2288 GG Rijswijk, the Netherlands, 2013.

[3] Hubin, N., "Deformable Mirror requirements for & feedbacks from VLT & E-ELT," in "Delft Workshop: High-performance Deformable Mirrors for Astronomy," OPTICON Innovation Network, Delft, 2013.

[4] Tyson, R., *Introduction to Adaptive Optics*, volume TT41 of *Tutorial texts in optical engineering*, SPIE Press, Bellingham, 2000.

[5] Roddier, F., ed., *Adaptive Optics in Astronomy*, Cambridge University Press, Cambridge, U.K., 1999.

[6] Vdovin, G. and Sarro, P.M., "Flexible mirror micromachined in silicon," *Appl. Optics*, **34** (16): 2968 – 2972, 1995.

[7] Devaney, N., Coburn, D., Coleman, C., *et al.*, "Characterisation of MEMs mirrors for use in atmospheric and ocular wavefront correction," in "MEMS Adaptive Optics II," volume 6888 of *Proc. SPIE*, 688802 – 688802–10, 2008.

[8] Flexible Optical B.V., "Micromachined membrane deformable mirrors," `http://www.okotech.com/mmdm/`, 2014, accessed: 2 March 2014.

[9] Helmbrecht, M. and Doble, N., "High Performance MEMS Deformable Mirrors for Adaptive Optics: Prototype Status," in "CfAO Fall Retreat," CfAO, Lake Arrowhead, CA, 2004.

[10] Boston Micromachines Corporation, "Kilo-DM," `http://www.boston micromachines.com/beam-shaper.htm`, 2013, accessed: 2 March 2014.

[11] Biasi, R., Gallieni, D., Salinari, P., *et al.*, "Contactless thin adaptive mirror technology: past, present, and future," in "Adaptive Optics Systems II," volume 7736 of *Proc. SPIE*, 77362B – 77362B–14, 2010.

[12] Tait, D., "Budget, Schedule, and Procurement Overview," `http://www.fct.pt/apoios/cooptrans/eso/docs/EELT_WBS.pdf`, 2012, accessed: 27 February 2014.

[13] European Southern Observatory, "The E-ELT Construction Proposal," `http://www.eso.org/sci/facilities/eelt/docs/e-elt_constrproposal.pdf`, 2012, accessed: 27 February 2014.

[14] Close, L., "Adaptive Optics at the MMT and First Science Results," `http://exoplanet.as.arizona.edu/~lclose/talks/ins/ESO_MMTAO_3`, 2004, accessed: 28 February 2014.

[15] Ambs, P., Otón, J., Millán, M., *et al.*, "Spatial Light Modulators For Information Processing: Applications And Overview," volume 949, 226 – 233, 2007.

[16] Loktev, M., *Modal Wavefront Correctors Based on Nematic Liquid Crystals*, Ph.D. thesis, Technische Universiteit Delft, Delft, 2005.

[17] Jewel, A., Akondi, V., and Vohnsen, B., "A direct comparison between a MEMS deformable mirror and a liquid crystal spatial light modulator in signal-based wavefront sensing," *J. Europ. Opt. Soc. Rap. Public.*, **8**: 13073–1 – 13073–10, 2013.

[18] Hong, D., Tao, X., and Cho, H., "An active imaging system using a deformable mirror and its application to super resolution," in "Optomechatronic Sensors, Instrumentation, and Computer-Vision Systems," volume 6375 of *Proc. SPIE*, 637503–637503–11, 2006.

[19] Laude, V., "Twisted-nematic liquid-crystal pixelated active lens," *Opt. Commun.*, **153**: 134 – 152, 1998.

[20] Boston Micromachines Corporation, "MEMS Deformable Mirrors," `http://www.bostonmicromachines.com/mems.htm`, 2013, accessed: 2 March 2014.

[21] Vdovin, G., "Closed-loop adaptive optical system with a liquid mirror," *Opt. Lett.*, **34** (4): 524 – 526, 2009.

[22] Harvard-Smithsonian Center for Astrophysics (CFA), Cambridge, MA, USA and V.E. Zuev Insitute of Atmosperic Optics (IAO), Tomsk, Russia, "Hitran on the web," `http://hitran.iao.ru/`, 2012, accessed: 2 December 2012.

[23] Rothman, L., Gamache, R., Goldman, A., *et al.*, "The HITRAN database: 1986 edition," *Appl. Optics*, **26** (19): 4058 – 4097, 1987.

[24] Rothman, L., Jacquemart, D., Barbe, A., *et al.*, "The HITRAN 2004 molecular spectroscopic database," *J. Quant. Spectrosc. Ra.*, **96** (2): 139 – 204, 2005.

[25] Rothman, L., Gordon, I., Barbe, A., *et al.*, "The HITRAN 2008 molecular spectroscopic database," *J. Quant. Spectrosc. Ra.*, **110** (9 - 10): 533 – 572, 2009.

[26] Hardy, J., *Adaptive Optics for Astronomical Telescopes*, Oxford University Press, Inc., New York, 1998.

[27] Taylor, G.I., "Statistical Theory of Turbulence," *Proc. R. Soc. Lon. Ser.-A*, **151**: 421 – 478, 1935.

[28] Kern, B., Laurence, T., Martin, C., *et al.*, "Temporal coherence of individual turbulent patterns in atmospheric seeing," *Appl. Optics*, **39** (27): 4879 – 4885, 2000.

[29] Kolmogorov, A., "The local structure of turbulence in incompressible viscous fluids for very large Reynolds numbers," *Dokl. Akad. Nauk SSSR*, **30**: 301 – 305, 1941, reprinted in Proc. R. Soc. Lon. Ser.-A **434**, 9 - 13 (1991).

[30] Kolmogorov, A., "Dissipation of energy in the locally isotropic turbulence," *Dokl. Akad. Nauk SSSR*, **32**: 16 – 18, 1941, reprinted in Proc. R. Soc. Lon. Ser.-A **434**, 15 - 17 (1991).

[31] Kolmogorov, A., "A refinement of previous hypotheses concerning the local structure of turbulence in a viscous incompressible fluid at high Reynolds number," *J. Fluid Mech.*, **13**: 82 – 85, 1962.

[32] Andrews, L., *Field Guide to Atmospheric Optics*, volume FG02 of *SPIE Field Guides*, SPIE Press, Bellingham, 2004.

[33] Richardson, L., *Weather Prediction by Numerical Process*, Cambridge University Press, Cambridge, U.K., 1922.

[34] Tatarski, V., *Wave propagation in a turbulent medium*, McGraw-Hill, New York, 1961.

[35] Batchelor, G., *The Theory of Homogeneous Turbulence*, Cambridge University Press, Cambridge, 1953.

[36] Tyson, R., *Principles of Adaptive Optics*, CRC Press, Boca Raton, 2011.

[37] Corrsin, S., "On the Spectrum of Isotropic Temperature Fluctuations in an Isotropic Turbulence," *J. Appl. Phys.*, **22** (4): 469 – 473, 1951.

[38] Strohbehn, J., ed., *Laser Beam Propagation in the Atmosphere*, Springer, New York, 1978.

[39] Tatarskii, V., *The Effects of the Turbulent Atmosphere on Wave Propagation*, Israel Program for Scientific Translations, Jerusalem, 1971.

[40] Lukin, V., *Atmospheric Adaptive Optics*, SPIE Press, Bellingham, 1996.

[41] Dainty, J., "A Short Course in Adaptive Optics: Lectures," in "Adaptive Optics short course," 1 - 3, Imperial College, London, 2006, lecture notes.

[42] Fante, R., "Electromagnetic Beam Propagation in Turbulent Media," *P. IEEE*, **63** (12): 1669 – 1692, 1975.

[43] Churnside, J. and Lataitis, R., "Wander of an optical beam in the turbulent atmosphere," *Appl. Optics*, **29** (7): 926 – 930, 1990.

[44] Chernov, L., *Wave Propagation in a Random Medium*, Dover, New York, 1967.

[45] Andrews, L. and Phillips, R., *Laser Beam Propagation through Random Media*, second edition.

[46] Jüngling, R., *Simulation gerichteter Ausbreitung optischer Wellen in turbulenter Atmosphäre*, Master's thesis, Westphälische Wilhelms-Universität, Münster, 2001.

[47] Clifford, S., Ochs, G., and Lawrence, R., "Saturation of optical scintillation by strong turbulence," *J. Opt. Soc. Am.*, **64** (2): 148 – 154, 1974.

[48] Ochs, G., Lawrence, R., Wang, T.I., *et al.*, "Refractive-turbulence profiles measured by one-dimensional filtering of scintillations," *Appl. Optics*, **15** (10): 2504 – 2510, 1976.

[49] Wang, T.I., Ochs, G., and Clifford, S., "A saturation-resistant optical scintillometer to measure C_n^2," *J. Opt. Soc. Am.*, **68** (3): 334 – 338, 1978.

[50] Rytov, S., "Diffraction of light by ultrasonic waves," *Izv. Akad. Nauk SSSR, Ser. Fiz.*, **2**: 223 – 259, 1937.

[51] Obukhov, A., "Influence of Weak Atmospheric Inhomogeneities Upon the Propagation of Sound and Light," *Izv. Akad. Nauk SSSR, Ser. Geofiz.*, **2**: 155 – 165, 1953.

[52] Tyson, R. and Frazier, B., *Field Guide to Adaptive Optics*, volume FG03 of *SPIE Field Guides*, SPIE Press, Bellingham, 2004.

[53] Fante, R., "Electromagnetic Beam Propagation in Turbulent Media: An Update," *P. IEEE*, **68** (11): 1424 – 1443, 1980.

[54] Fried, D., "The Effect of Wave-Front Distortion on the Performance of an Ideal Optical Heterodyne Receiver and an Ideal Camera," in "Conference on Atmospheric Limitations to Optical Propagation," U.S. National Bureau of Standards CRPL, Gaithersburg, MD, 1965.

[55] Taylor, G.I., "The spectrum of turbulence," *Proc. R. Soc. Lon. Ser.-A*, **164**: 476 – 490, 1938.

[56] Greenwood, D., "Bandwidth specification for adaptive optics systems," *J. Opt. Soc. Am.*, **67** (3): 390 – 393, 1977.

[57] Devaney, N., "GTC project," `http://www-obs.univ-lyon1.fr/IMG/ppt/1.ppt`, 2002, accessed: 20 October 2012.

[58] Roddier, F., "Atmospheric limitations to adaptive image compensation," in "Astronomical Site Evaluation in the Visible and Radio Range," volume 266 of *Astr. Soc. P.*, 546 – 561, Astronomical Society of the Pacific, Marrakech, Morocco, 2002.

[59] Liang, J. and Williams, D., "Aberrations and retinal image quality of the normal human eye," *J. Opt. Soc. Am. A*, **14** (11): 2873 – 2883, 1997.

[60] Liang, J., Williams, D., and Miller, D., "Supernormal vision and high-resolution retinal imaging through adaptive optics," *J. Opt. Soc. Am. A*, **14** (11): 2884 – 2892, 1997.

[61] Roorda, A., "Adaptive optics for studying visual function: A comprehensive review," *J. Vision*, **11** (5): 1 – 21, 2011.

[62] Porter, J., Queener, H., Lin, J., *et al.*, eds., *Adaptive Optics for Vision Science: Principles, Practices, Design, and Applications*, John Wiley & Sons, Hoboken, 2006.

[63] Babcock, H., "The possibility of compensating astronomical seeing," *Publ. Astron. Soc. Pac.*, **65** (386): 229 – 236, 1953.

[64] Hardy, J., "Adaptive optics – a progress review," in "Active and Adaptive Optical Systems," volume 1542 of *Proc. SPIE*, 2 – 19, 1991.

[65] Benedict, R., J., Breckinridge, J., and Fried, D., "Atmospheric compensation technology: Introduction," *J. Opt. Soc. Am. A*, **11** (1): 257 – 262, 1994.

[66] Born, M. and Wolf, E., *Principles of Optics*, sixth edition, Cambridge University Press, Cambridge, 1997.

[67] Zernike, F., "Diffraction theory of the knife-edge test and its improved form, the phase-contrast method," *Mon. Not. R. Astron. Soc.*, **94**: 377 – 384, 1934.

[68] Noll, R., "Zernike polynomials and atmospheric turbulence," *J. Opt. Soc. Am.*, **66** (3): 207 – 211, 1976.

[69] Maeda, P., "Zernike Polyomials and Their Use in Describing the Wavefront Aberrations of the Human Eye," in "Psych221/EE326 Applied Vision and Imaging Systems," Stanford University, 2002, lecture notes.

[70] Close, L., "AO System performance," in "Astro519 Adaptive Optics," University of Arizona, Tuscon, 2003, lecture notes.

[71] Wood, R., "The Mercury Paraboloid as a Reflecting Telescope," *Astrophys. J.*, **29**: 164 – 176, 1909.

[72] Borra, E., Beauchemin, M., and Lalande, R., "Liquid Mirror Telescopes: Observations with a 1 Meter Diameter Prototype and Scaling-up Considerations," *Astrophys. J.*, **297**: 846 – 851, 1985.

[73] Hickson, P., Borra, E., Cabanac, R., *et al.*, "UBC/Laval 2.7 Meter Liquid Mirror Telescope," *Astrophys. J.*, **436**: L201 – L204, 1994.

[74] Ragazzoni, R. and Marchetti, E., "A liquid deformable mirror," *Astron. Astrophys.*, **283** (2): L17 – L19, 1994.

[75] Borra, E.F., Ritcey, A.M., Bergamasco, R., *et al.*, "Nanoengineerd astronomical optics," *Astron. Astrophys.*, **419**: 777 – 782, 2004.

[76] Brousseau, D., Borra, E., Rochette, M., *et al.*, "Linearization of the response of a 91-actuator magnetic liquid deformable mirror," *Opt. Express*, **18** (8): 8239 – 8250, 2010.

[77] Vuelban, E., *Adaptive Optics: A Liquid Deformable Mirror for High-Order Wavefront Correction*, Ph.D. thesis, Technische Universiteit Delft, Delft, 2006.

[78] Fischer, F. and Thiemann, H., "Theoretische Betrachtungen über ein neues Verfahren der Fernsehgrossprojektion," *Schweiz. Arch. Angew. Wiss. Tech.*, **1** (1, 2, 3, and 4), 1941.

[79] Lide, D., ed., *Handbook of Chemistry and Physics*, 88th edition, CRC Press, Boca Raton, 2008.

[80] de Mendonça, C.G., Raetano, C., and de Mendonça, C.G., "Surface tension of mineral oils and vegetable oils," *Eng. Agrc.*, **27**: 16 – 23, 2007, in Portuguese.

[81] Panther Lubricants, "Technical Learning, Surface Tension," `http://www.pantherlubes.com/tl_14.html`, 2004, accessed: 22 June 2013.

[82] VWR International LLC, "Mineral Oil Safety Data Sheet," `https://us.vwr.com/stibo/hi_res/71003-510.pdf`, 2013, accessed: 22 June 2013.

[83] ten Have, E. and Vdovin, G., "Novel method for measuring surface tension," *Sensor. Actuat. A - Phys.*, **173** (1): 90 – 96, 2012.

[84] Landau, L. and Lifshitz, E., *Fluid Mechanics*, volume 6 of *Course of Theoretical Physics*, second edition, Butterworth Heinemann, 2009.

[85] Saranin, V., *Ravnovesie zhidkostey i ego ustoychivost*, Institut kompyuternykh issledovaniy, Moscow, 2002.

[86] Briskman, V. and Shaidurov, G., "Mechanisms of instability of liquid surfaces in constant and variable electric fields," in "Hydrodynamics," volume 2 of *Uch. Zap. Perm. Univ.*, 229 – 240, Perm Univ., Perm, 1970, in Russian.

[87] Reitz, J., Milford, F., and Christy, R., *Foundations of Electromagnetic Theory*, fourth edition, Addison-Wesley, Reading, 1993.

[88] Nishiyama, H. and Nakamura, M., "Capacitance of Disk Capacitors," *IEEE T. Compon. Hybr.*, **16** (3): 360 – 366, 1993.

[89] Bao, J.Z. and Davis, C., "Study of fringing-field effects on the capacitance of a dielectric disk with a circular conducting hole," *Phys. Rev. E*, **47** (5): 3670 – 3676, 1993.

[90] Hegg, M. and Mamishev, A., "Influence of Variable Plate Separation on Fringing Electric Fields in Parallel-Plate Capacitors," in "IEEE Int. Sym. Elec. In.", IEEE, Indianapolis, IN, 2004.

[91] Batchelor, G., *An Introduction to Fluid Dynamics*, Cambridge University Press, Cambridge, 2002.

[92] Bauer, H., "Fluid Oscillations in the Containers of a Space Vehicle and their Influence Upon Stability," *Technical Report NASA TR R-187*, NASA, George C. Marshall Space Flight Center, Huntsville, Alabama, 1964.

[93] Abramson, H., "The Dynamic Behavior of Liquids in Moving Containers with Applications to Space Vehicle Technology," *Technical Report NASA SP-106*, NASA, Scientific and Technical Information Division, Washington, DC, 1966.

[94] Dodge, F., "The New "Dynamic Behavior of Liquids in Moving Containers"," *Technical report*, Southwest Research Institute, San Antonio, Texas, 2000.

[95] Ibrahim, R., *Liquid Sloshing Dynamics, Theory and Applications*, Cambridge University Press, Cambridge, 2005.

[96] Bauer, H., "Tables of Zeros of Cross Product Bessel Functions," *Math. Comput.*, **18** (85): 128 – 135, 1964.

[97] Dong, J., Qi, J., and Miao, R., "Measurement of the Damping of Liquid Surface Wave by Diffraction Method," *Braz. J. Phys.*, **37** (3B): 1129 – 1133, 2007.

[98] Miles, J., "Surface-wave damping in closed basins," *Proc. R. Soc. Lon. Ser.-A*, **297**: 459 – 475, 1967.

[99] Lamb, H., *Hydrodynamics*, sixth edition, Cambridge University Press, 1975.

[100] Mei, C. and Liu, L., "The damping of surface gravity waves in a bounded liquid," *J. Fluid Mech.*, **59**: 239 – 256, 1973.

[101] Levich, V., *Physiochemical Hydrodynamics*, second edition, Prentice-Hall, Inc., Englewood Cliffs, N.J., 1962.

[102] DiStefano, J.J., Stubberud, A.R., and Williams, I.J., *Outline of Theory and Problems of Feedback and Control Systems*, Schaum's Outline Series, second edition, McGraw-Hill, 1990.

[103] Cheng, N., "Formula for viscosity of glycerol-water mixture," *Ind. Eng. Chem. Res.*, **47**: 3285 – 3288, 2008.

[104] Thomas, S., "A simple turbulence simulator for adaptive optics," in "Advancements in Adaptive Optics," volume 5490 of *Proc. SPIE*, 766 – 773, 2004.

[105] Rampy, R., Gavel, D., Dillon, D., *et al.*, "New method of fabricating phase screens for simulated atmospheric turbulence," in "Adaptive Optics Systems II," volume 7736 of *Proc. SPIE*, 77362Y – 77362Y–10, 2010.

[106] DiStefano, J.J., Stubberud, A.R., and Williams, I.J., *Schaum's Outline of Theory and Problems of Feedback and Control Systems*, Schaum's Outline Series, second edition, McGraw-Hill, New York, 1990.

[107] Golub, G. and Van Loan, C., *Matrix Computations*, Johns Hopkins Studies in the Mathematical Sciences, third edition, Johns Hopkins University Press, Baltimore, 1996.

[108] Paterson, C., Munro, I., and Dainty, J.C., "A low cost adaptive optics system using a membrane mirror," *Opt. Express*, **6** (9): 175 – 185, 2000.

[109] Dalimier, E. and Dainty, C., "Comparative analysis of deformable mirrors for ocular adaptive optics," *Opt. Express*, **13** (11): 4275 – 4285, 2005.

[110] Brusa, G., Riccardi, A., Wildi, F., *et al.*, "MMT adaptive secondary: first AO closed-loop results," in "Astronomical Adaptive Optics Systems and Applications," volume 5169 of *Proc. SPIE*, 26 – 36, 2003.

[111] Fishbain, B., Ideses, I.A., Shabat, G., *et al.*, "Superresolution in color videos acquired through turbulent media," *Opt. Lett.*, **34** (5): 587 – 589, 2009.

[112] Kern, B., Dimotakis, P.E., Martin, C., *et al.*, "Imaging through turbulence with a quadrature-phase optical interferometer," *Appl. Optics*, **44** (34): 7424 – 7438, 2005.

[113] Kuan, D.T., Sawchuck, A.A., Strand, T.C., *et al.*, "Adaptive Restoration of Images with Speckle," *IEEE T. Acoust. Speech*, **ASSP-35** (3): 373 – 383, 1987.

[114] Lohmann, A.W., Weigelt, G., and Wirnitzer, B., "Speckle masking in astronomy: triple correlation theory and applications," *Appl. Optics*, **22** (24): 4028 – 4037, 1983.

[115] Weigelt, B. and Wirnitzer, B., "Image reconstruction by the speckle-masking method," *Opt. Lett.*, **8** (7): 389 – 391, 1983.

[116] Yaroslavsky, L., Fishbain, B., Shabat, G., *et al.*, "Superresolution in turbulent videos: making profit from damage," *Opt. Lett.*, **32** (20): 3038 – 3040, 2007.

[117] Zamek, S. and Yitzhaky, Y., "Turbulence Strength Estimation and Super-Resolution from an Arbitrary Set of Atmospherically Degraded Images," in "Atmospheric Optical Modeling, Measurement, and Simulation II," volume 6303 of *Proc. SPIE*, 630303 – 630303–11, 2006.

[118] Chen, L., Singer, B., Guirao, A., *et al.*, "Image Metrics for Predicting Subjective Image Quality," *Optometry Vision Sci.*, **82** (5): 358 – 369, 2005.

[119] Thibos, L., Hong, X., Bradley, A., *et al.*, "Metrics of optical quality of the eye," *J. Vision*, 2003.

[120] Fienup, J.R. and Miller, J.J., "Aberration correction by maximizing generalized sharpness metrics," *J. Opt. Soc. Am. A*, **20** (4): 609 – 620, 2003.

[121] Ferzli, R., Karam, L., and Caviedes, J., "A robust image sharpness metric based on kurtosis measurement of wavelet coefficients," in "Proc. of Int. Workshop on Video Processing and Quality Metrics for Consumer Electronics," , 2005.

[122] Goodman, D., Lawrence, T., Johansson, E., *et al.*, *Signal Processing and its Applications*, volume 10 of *Handbook of Statistics*, chapter 10, 355 – 397, third edition, 1993.

[123] Linfoot, E.H., "Transmission Factors and Optical Design," *J. Opt. Soc. Am.*, **46** (9): 740 – 747, 1956.

[124] Lowitz, G.E., "Mapping the Local Information Content of a Spatial Image," *Pattern Recogn.*, **17** (5): 545 – 550, 1984.

[125] Luo, G., "Objective image quality measurement by local spatial-frequency wavelet analysis," *Int. J. Remote Sens.*, **27** (22): 5003 – 5025, 2006.

[126] Muller, R.A. and Buffington, A., "Real-time correction of atmospherically degraded telescope images through image sharpening," *J. Opt. Soc. Am.*, **64** (9): 1200 – 1210, 1974.

[127] Vu, C. and Chandler, D., "S3: A Spectral and Spatial Sharpness Measure," in "2009 First International Conference on Advances in Multimedia," 37 – 43, IEEE, Colmar, France, 2009.

[128] Shannon, C., "A Mathematical Theory of Communication," *Bell Syst. Tech. J.*, **27** (10): 379 423, 623 656, 1948.

[129] Cover, T. and Thomas, J., *Elements of Information Theory*, second edition, John Wiley & Sons, Hoboken, 2006.

[130] Sakarya, S., Vdovin, G., and Sarro, P., "Technology of reflective membranes for spatial light modulators," *Sensor. Actuat. A - Phys.*, **97 - 98**: 468 – 472, 2002.

[131] Hornbeck, L., "Deformable-Mirror Spatial Light Modulators," in "Spatial Light Modulators and Applications III," volume 1150 of *Proc. SPIE*, 86 – 103, 1990.

[132] Goodman, J., *Introduction to Fourier Optics*, second edition, McGraw-Hill, New York, 1996.

[133] Trancho, G., Espeland, B., Bouchez, A.H., *et al.*, "GMT AO system requirements and error budgets in the preliminary design phase," in "Adaptive Optics Systems III," volume 8447 of *Proc. SPIE*, 84475G – 84475G–17, 2012.

[134] Ellerbroek, B., "Adaptive Optics Systems for the Thirty Mirror Telescope," in Y. Clénet, J.M. Conan, T. Fusco, and G. Rousset, eds., "1st AO4ELT conference - Adaptive Optics for Extremely Large Telescopes," 02001, 2010.

[135] Taylor, G.I., "The Instability of Liquid Surfaces when Accelerated in a Direction Perpendicular to their Planes. I," *Proc. R. Soc. Lon. Ser.-A*, **201**: 192 – 196, 1950.

[136] Lewis, D., "The Instability of Liquid Surfaces when Accelerated in a Direction Perpendicular to their Planes. II," *Proc. R. Soc. Lon. Ser.-A*, **202**: 81 – 96, 1950.

[137] Quéré, D., "Wetting and Roughness," *Annu. Rev. Mater. Res.*, **38** (1): 71 – 99, 2008.

[138] White, W., "Use of Wetting Agents in Glass Apparatus," *Ind. Eng. Chem.*, **12** (9): 550 – 550, 1940.

[139] Zeller, H., *Laboratory Tests for Selecting Wetting Agents for Coal Dust Control*, U.S. Dept. of the Interior, Bureau of Mines, Pittsburgh, 1983.

[140] Callow, M., Callow, J., Ista, L., *et al.*, "Use of Self-Assembled Monolayers of Different Wettabilities to Study Surface Selection and Primary Adhesion Processes of Green Algal (Enteromorpha) Zoospores," *Appl. Environ. Microb.*, **66** (8): 3249 – 3254, 2000.

[141] Janssen, D., De Palma, R., Verlaak, S., *et al.*, "Static solvent contact angle measurements, surface free energy and wettability determination of various self-assembled monolayers on silicon dioxide," *Thin Solid Films*, **515** (4): 1433 – 1438, 2006.

[142] Bico, J., Thiele, U., and Quéré, D., "Wetting of textured surfaces," *Colloid Surface A*, **206** (1 - 3): 41 – 46, 2002.

[143] Ding, C., Bogorzi, P., Srivastava, N., *et al.*, "Super Wetting of Micro&Nano Structured Titania Surfaces," in "The 15th International Conference on Solid-State Sensors, Actuators and Microsystems (Transducers)," 401 – 404, IEEE, Denver, CO, 2009.

[144] Ding, C., "Tunable Wetting of Titanium and Gold Based Wicking Materials," in "Nanotech 2010," volume 1, 616 – 619, NSTI, Anaheim, CA, 2010.

[145] Öner, D. and McCarthy, T., "Ultrahydrophobic Surfaces. Effects of Topography Length Scales on Wettability," *Langmuir*, **16** (10): 7777 – 7782, 2000.

[146] Lazauskas, A. and Grigaliunas, V., "Float Glass Surface Preparation Methods for Improved Chromium Film Adhesive Bonding," *Mater. Sci.-Medzg.*, **18** (2): 181 – 186, 2012.

[147] Müller-Buschbaum, P., "Infuence of surface cleaning on dewetting of thin polystyrene films," *Eur. Phys. J. E*, **12** (3): 443 – 448, 2003.

[148] Bico, J., Tordeux, C., and Quéré, D., "Rough wetting," *Europhys. Lett.*, **55** (2): 214 – 220, 2001.

[149] Stjernström, M. and Roeraade, J., "Method for fabrication of microfuidic systems in glass," *J. Micromech. Microeng.*, **8** (10): 33 – 38, 1998.

[150] Washburn, E., "The dynamics of capillary flow," *Phys. Rev.*, **17** (3): 273 – 283, 1921.

[151] Zhang, Y. and Roorda, A., "MEMS Deformable Mirror for Ophthalmic Imaging," in "MEMS/MOEMS Components and Their Applications III," volume 6113 of *Proc. SPIE*, 61130A–1 – 661130A–8, 2006.

List of Abbreviations

AO	Adaptive Optics
CCD	charge coupled device
ch	channel
DC	direct current
DOC	degree of coherence
E-ELT	European Extremely Large Telescope
FWHM	full width at half maximum
GC	gain crossover
GM	gain margin
HeNe	Helium-Neon
HITRAN	high-resolution transmission molecular absorption database
HF	hydrofluoric acid
IAO	V.E. Zuev Insitute of Atmosperic Optics, Tomsk, Russia
IR	infrared
LC	liquid crystal
LGS	Laser Guide Star
MEMS	Micro Electro-Mechanical System
MMDM	micro-machined deformable mirror
MMT	Multiple Mirror Telescope
NIR	near infrared
PC	phase crossover
PCB	printed circuit board
PM	phase margin
rms	root mean square
SAM	self-assembling monolayer
SLM	spatial light modulator
SVD	singular value decomposition
TIR	total internal reflection

List of Figures

List of Tables

Summary

Adaptive Optics based on liquid Total Internal Reflection Mirrors

While an adaptive optical system consists of many parts, the wavefront corrector is at the heart of every system – here is where the actual shaping of the wavefronts takes place. In most cases the wavefront corrector is realized as a deformable mirror which consists of a solid reflecting surface to which an actuator structure is attached. Traditionally, these deformable mirrors suffer from the limitations of the solid reflecting surface, e.g. the limited relative movement of two adjacent actuators. Also, the cost of such a deformable mirror with a reflecting surface of high quality increases exponentially with the size of the mirror and the quality of the optical surface.

This thesis investigates a novel deformable mirror that works on the basis of the electrostatic deformation of a liquid surface. A static electric field is used to manipulate a liquid surface which shapes the wavefronts of a laser beam through total internal reflection. This mirror was expected to allow large surface displacements with relatively low applied voltages by a large number of actuators. Modification of the physical properties of the liquid mirror should permit the adjustment of the dynamics and the influence function of the device, while at the same time the design should remain simple without the need for sophisticated technology. Finally, the liquid mirror should deliver close to 100% reflectivity for a broad wavelength range and still be a low-cost device.

The goal of this thesis was to verify these claims, to demonstrate that the liquid mirror is capable of dynamically correcting distorted wavefronts, and to investigate the limits of operation of the liquid mirror.

Chapter 1 briefly presents the context for this work and the outline of the thesis. Chapter 2 gives an introduction into beam propagation through the atmosphere and turbulence. The Kolmogorov model of turbulence is discussed and the turbulence structure constant, which is a measure for the strength of turbulence, is derived. The optical effects of turbulence are summarized and the dynamics of turbulence are introduced through the isoplanatic angle and the Greenwood

frequency. The application of Adaptive Optics for the compensation of the effects of turbulence is introduced and the principle of representing wavefronts as a sum of Zernike polynomials, similar to the Fourier decomposition for waveforms, and the residual errors due to the compensation process are presented.

In chapter 3 the fluid for the liquid mirror is selected and the properties of the liquid system are investigated. An aqueous solution of 80% glycerol is chosen as liquid for the liquid mirror, because it combines a decoupling of the liquid system from ambient vibrations with short rise times of around 10 ms. The theory of the influence of static electric fields on liquid surfaces is presented, based on which the liquid deformation as a function of the system parameters is simulated. The simulations show that the width of the liquid deformation mainly depends on the width of the electrode. Measurements of the liquid deformation show a good agreement to the simulated results.

The theory of liquid motion is reviewed, from which the eigenmodes of the liquid container are derived. The open-loop frequency response is measured and shows good agreement with the calculations. The bandwidth is about 80 Hz with a gain margin of 11.4 dB and a phase margin of $140°$, while the rise-time for a single actuator is about 10.5 ms, and the relaxation-time about 4.5 ms. The damping times of both the open- and closed-loop systems are experimentally determined to be $\tau_{\mathrm{open}} = 1.3$ s and $\tau_{\mathrm{closed}} = 1.1$ s, respectively.

Chapter 4 examines the performance of the liquid mirror device. First, it it applied as a wavefront corrector and the correction of static and dynamic aberrations is investigated. The corrective power of the liquid mirror is expressed as the ratio of the amount of aberrations present on the wavefronts of the aberrated and corrected beams expressed in terms of the Strehl ratio or the rms-error of the wavefront. It is shown that the average improvement for static aberrations in terms of rms-error and Strehl ratio is $I_{\mathrm{rms}} = 6.44$ and $I_{\mathrm{S}} = 438$, respectively. The performance of the liquid mirror for the correction of dynamic aberrations is demonstrated to depend on the parameters of the feedback system, e.g. gain or control frequency, and the strength of the dynamic aberrations. According to expectations the liquid mirror performs better for static aberrations than for dynamic aberrations with improvements of up to $I_{\mathrm{rms, \ static}} = 12$ and $I_{\mathrm{rms, \ dynamic}} = 4.5$, respectively. The influence of ambient vibrations coupled to the liquid surface on the performance of the liquid mirror is investigated and it is shown that the liquid mirror partly compensates these disturbances.

In a second application the liquid mirror is used for fine imaging. Different metrics to evaluate image sharpness are reviewed and applied to distorted images corrected by the liquid mirror. It is demonstrated that the four metrics have different sensitivities to changes in image sharpness. While image sharpness appears higher after improvement by the liquid mirror, quantification of the sharpness increase with the metrics shows only a limited improvement.

Finally, the liquid mirror is applied as a spatial light modulator. The ability of the liquid mirror to manipulate an optical beam to generate points, lines, and arbitrary patterns in the far field is demonstrated.

In chapter 5 the possibility of scaling of the liquid mirror is examined. The first part investigates the behavior of the liquid mirror with a large number of actuators and demonstrates the successful operation with an actuator structure consisting of 70 actuators. A phase of instability is observed, which is attributed to the dynamics of the feedback system and therefore does not fundamentally limit the size of the liquid mirror or the number of actuators.

In the second part a liquid micro-mirror is developed that suppresses the coupling of ambient vibrations to the liquid layer. It is shown that the surface of a glass prism may be etched with an aqueous solution of HF such that the micro-mirror can be operated with a sub-mm film of water without the need for an additional liquid container. The eigenmodes and the open-loop frequency response of the liquid layer are determined for water and an aqueous solution of 80% glycerol. It is shown that due to excessively large time constants the aqueous solution of 80% glycerol is not suited for this application. For water, a bandwidth of about 3 Hz with a gain margin of 14 dB and a phase margin of 162°, a single actuator rise-time of about 2.5 s, a single actuator relaxation-time of about 0.4 s, and an open-loop damping time of $\tau_{\text{open}} = 0.07$ s were measured. Suggestions for a further development and optimization of the properties of the liquid micro-mirror are given.

Chapter 6 summarizes the results and conclusions of this thesis and presents recommendations for further work.

This thesis investigates a novel deformable mirror that works on the basis of the electrostatic deformation of a liquid surface. The liquid mirror allows large surface displacements, a large number of actuators, and the modification of its properties, while at the same time the mirror design is simple and may be realized without sophisticated technology. The mirror is capable of dynamic wavefront correction, fine imaging, and spatial light modulation. The mirror is demonstrated to be a low-cost versatile tool for Adaptive Optics that can be implemented for less than 100 €.

Samenvatting

Adaptieve optica met vloeistof spiegels gebaseerd op totale interne reflectie

Van alle onderdelen die een adaptief optisch systeem uitmaken vormt de golffront corrector het hart van het systeem – hier vindt de daadwerkelijke vorming van de golffronten plaats. In het algemeen is de golffront corrector gerealiseerd als een vervormbare spiegel bestaand uit een vast spiegel oppervlak met een aangehechte actuator structuur. Door de vaste stof eigenschappen van het spiegel oppervlak is het verschil in amplitude van twee naast elkaar liggende actuatoren begrensd. Ook nemen de kosten van een dergelijke deformeerbare spiegel met de grootte en de kwaliteit van het spiegel oppervlak exponentieel toe.

Dit proefschrift onderzoekt een nieuw type deformeerbare spiegel op basis van de elektrostatische vervorming van een vloeistof oppervlak. Met een statisch elektrisch veld wordt een vloeistof oppervlak gemanipuleerd welke de golffronten van een laserstraal vormt door totale interne reflectie. De verwachte eigenschappen van deze spiegel houden grote oppervlakte amplitudes bij lage elektrische spanningen met een groot aantal actuatoren in, de mogelijkheid tot aanpassing van de dynamische eigenschappen en de invloedsfunctie (influence function) van de spiegel door aanpassen van de fysische eigenschappen van de spiegel en de vloeistof en een bijna volkomen reflectiviteit over een breed golflengtegebied. Tegelijkertijd is de spiegel eenvoudig van opbouw, verijst geen geavanceerde technologieën en kan kosteneffectief gemaakt worden.

Het doel van dit proefschrift is de verificatie van deze stellingen, het aantonen van de geschiktheid van de vloeistof spiegel voor het compenseren van gestoorde golffronten en het verkennen van de grenzen van de toepasbaarheid van de spiegel.

Hoofdstuk 1 geeft een korte introductie in de context en de opzet van dit proefschrift.

In hoofdstuk 2 wordt de theorie van de propagatie van stralen in de atmosfeer en turbulentie geïntroduceerd. Het Kolmogorov model van de turbulentie wordt voorgesteld en de structuur constante, een maat voor de sterkte van turbulentie,

155

wordt afgeleid. De optische effecten van turbulentie worden samengevat terwijl de dynamiek van de turbulentie wordt geïntroduceerd door middel van de isoplanatische hoek en de Greenwood frequentie. Ook worden het gebruik van een adaptieve optiek voor de compensatie van de gevolgen van turbulentie, de representatie van golffronten als een reeks Zernike polynomen en de resterende fouten in het golffront als gevolg van het compensatie proces gepresenteerd.

Hoofdstuk 3 omvat de selectie van de vloeistof voor de spiegel en het onderzoek van de eigenschappen van de vloeistof spiegel. Als medium wordt een waterige oplossing van 80% glycerine gekozen vanwege de ontkoppelende werking tegenover vibraties uit de omgeving als ook de lage stijgtijden van ongeveer 10 ms. De theorie van de effecten van elektrostatische velden op vloeistof oppervlakken wordt gepresenteerd, op basis waarvan de vervorming van het spiegel oppervlak wordt gesimuleerd. De simulaties tonen aan dat de breedte van de vloeistof vervorming voornamelijk van de afmeting van de elektrode afhangt. De resultaten van de simulaties en de metingen tonen een goede overeenkomst.

De theorie van de beweging van een vloeistof in een gesloten container wordt besproken en daaruit de eigenmodes van het vloeistof systeem afgeleid. De openloop frequentierespons wordt gemeten en vertoont een goede overeenstemming met de berekeningen. De bandbreedte is ongeveer 80 Hz met een gain-marge van 11.4 dB en een fase-marge van $140\,^\circ$. De stijg- en relaxatie-tijden van een enkele actuator zijn respectievelijk 10.5 ms en 4.5 ms en de dempingstijden voor de open- en closed-loop systemen zijn respectievelijk $\tau_{\mathrm{open}} = 1.3$ s en $\tau_{\mathrm{closed}} = 1.1$ s.

Hoofdstuk 4 onderzoekt het vermogen van de spiegel om golffronten te corrigeren in verschillende experimentele opstellingen. Als eerste wordt de spiegel als golffront corrector voor de compensatie van statische en dynamische gestoorde golffronten toegepast. De mate van correctie wordt uitgedrukt als de verhouding tussen de grootte van de aberraties op de gestoorde en gecorrigeerde golffronten in termen van de Strehlverhouding en de rms-golffrontafwijking. De gemiddelde correctiefactoren voor statische storingen in termen van de rms-golffrontafwijking en de Strehlverhouding zijn respectievelijk $I_{\mathrm{rms}} = 6.44$. Onderzoek van de dynamische correctie van golffronten toont aan dat de correctiefactor afhankelijk is van de parameters van het regelsysteem, zoals de versterking of de regelfrequentie, en de sterkte van de dynamische storingen. Volledig volgens de verwachtingen presteert de vloeistof spiegel beter voor de correctie van statische aberraties dan voor dynamische met correctiefactoren tot $I_{\mathrm{rms,\,statisch}} = 12$ en $I_{\mathrm{rms,\,dynamisch}} = 4.5$. De invloed van omgevingstrillingen op de prestatie van de spiegel wordt onderzocht en het kan worden aangetoond dat deze trillingen gedeeltelijk gecompenseerd kunnen worden.

In een tweede toepassing wordt de spiegel gebruikt voor Fine-Imaging, dat wil zeggen voor het verbeteren van de scherpte van door turbulentie gestoorde beelden. Verschillende methodes voor de evaluatie van beeldscherpte worden vergeleken en op met de vloeistof spiegel gecorrigeerde beelden toegepast. Het kan aangetoond worden dat de vier methodes verschillende gevoeligheden voor veranderingen in de beeldscherpte hebben. Hoewel met de vloeistof spiegel een zichtbare verbe-

tering van de beeldscherpte bereikt kan worden, is de kwantitatieve verbetering maar beperkt aantoonbaar.

Tenslotte wordt de vloeistof spiegel toegepast als ruimtelijke licht modulator. Het vermogen van de spiegel om uit een laserstraal punten, lijnen en willekeurige patronen te vormen kan woorden aangetoond.

In hoofdstuk 5 wordt de mogelijkheid van schalering van de vloeistof spiegel onderzocht. Het eerste gedeelte beantwoord de vraag of vloeistof spiegel en actuatorstructuur uitgebreid kunnen worden en toont aan dat de spiegel succesvol met 70 actuatoren gebruikt kan worden. Een tussentijdse fase van instabiliteit kan met de dynamiek van de vloeistof spiegel verklaard worden en betekent geen principieel hindernis voor een vergroting van de vloeistof spiegel of een uitbreiding van het aantal actuatoren.

In het tweede gedeelte wordt een vloeistof micro-spiegel ontworpen die de koppeling van omgevingstrillingen naar de vloeistoflaag voorkomt. Het oppervlak van een glazen prisma wordt zodanig met een waterige oplossing van HF geëtst dat een sub-mm film van water gevormd kan worden en de micro-spiegel zonder een apart vloeistof reservoir gebruikt kan worden. De eigenmodes en de open-loop frequentierespons van de micro-spiegel zijn voor water en een waterige oplossing van 80% glycerine gemeten. Het wordt aangetoond dat de waterige oplossing van 80% glycerine door de grote stijgtijden niet geschikt is voor toepassing in de micro-spiegel. Voor water bedragen de bandbreedte ongeveer 3 Hz met een gain-marge van 14 dB en een fase-marge van $162°$, de stijg- en en relaxatie-tijden respectievelijk 2.5 s en 0.4 s en de open-loop dempingstijd $\tau_{\text{open}} = 0.07$ s. Het hoofdstuk sluit af met suggesties voor verdere ontwikkeling en optimalisering van de vloeistof micro-spiegel.

Hoofdstuk 6 geeft een overzicht van de resultaten en conclusies van dit proefschrift en doet aanbevelingen voor verder onderzoek.

In dit proefschrift wordt een nieuwe flexibele spiegel op basis van de elektrostatische vervorming van een vloeistof oppervlak onderzocht. Met een statisch elektrisch veld wordt een vloeistof oppervlak vervormt dat wederom door totale interne reflectie de golffronten van een laserstraal kan vormen. De vloeistof spiegel maakt grote amplitudes, een groot aantal correctie elementen en een bijna perfecte reflectiviteit over een breed golflengtebereik mogelijk. Tegelijkertijd heeft de vloeistof spiegel een eenvoudige opbouw en functioneert zonder ingewikkelde technologieën. De vloeistof spiegel is in staat om statische en dynamische golffrontstoringen te compenseren met een reductie van de rms-golffrontafwijking tot een factor 12 voor statische storingen en een factor 4,5 voor dynamische storingen. De toepassing van de vloeistof spiegel voor imaging met hoge resolutie en als licht modulator is ook aangetoond. De vloeistof spiegel is een voordelig en veelzijdig instrument voor de adaptieve optica dat voor minder dan 100 € gerealiseerd kan worden.

Zusammenfassung

Adaptive Optik mit Flüssigspiegeln basierend auf totaler interner Reflektion

Adaptive optische Systeme bestehen aus einer großzahl verschiedener Komponenten, deren Herzstück der Wellenfrontkorrektor ist – hier geschieht die eigentliche Formung der Wellenfronten. In den meisten Fällen ist der Wellenfrontkorrektor als deformierbarer Spiegel ausgeführt, der aus einer festen Spiegelfläche mit befestigter Aktuatorstruktur besteht. Durch die Festkörpereigenschaften der Spiegelfläche ist der Hub zweier benachbarter Aktuatoren allerdings begrenzt. Darüberhinaus steigen die Kosten für einen solchen deformierbaren Spiegel exponentiell mit der Größe und der optischen Güte der Spiegelfläche.

Diese Arbeit untersucht einen neuen deformierbaren Spiegel, dessen Prinzip auf der elektrostatischen Formung einer Flüssigkeitsoberfläche beruht. Mit einem elektrostatischen Feld wird die Oberfläche einer Flüssigkeit manipuliert, welche durch totale interne Reflektion die Wellenfronten eines Laserstrahls formt. Zu den erwarteten Eigenschaften des Flüssigspiegels gehören große Oberflächenauslenkungen bei relativ geringen Spannungen für eine große Anzahl von Aktuatoren, die Möglichkeit zur Abstimmung der dynamischen Eigenschaften und der Einflussfunktion des Spiegels an die jeweiligen Anforderungen durch Anpassung der Eigenschaften von Spiegel und Flüssigkeit und eine nahezu vollkommene Reflektivität für einen breiten Wellenlängenbereich. Gleichzeitig soll der Flüssigspiegel einen einfachen Aufbau haben, ohne komplizierte Technologie auskommen und kostengünstig herzustellen sein.

Die vorliegende Arbeit überprüft diese Ansprüche, demonstriert die Kompensation von dynamisch gestörten Wellenfronten in Echtzeit und zeigt die Grenzen für die Nutzung des Flüssigspiegels auf.

In Kapitel 1 wird der Hintergrund der Arbeit erläutert und die Gliederung vorgestellt.

Kapitel 2 gibt eine Einleitung in die Thematik der Strahlausbreitung in der Atmosphäre und der Turbulenz. Das Kolmogorov Modell der Turbulenz wird vorgestellt

und die Strukturkonstante der Turbulenz, ein Maß für die Turbulenzstärke, abgeleitet. Die optischen Effekte der Turbulenz werden zusammengefasst und die zeitliche Varianz der Turbulenz am Beispiel des isoplanatischen Winkels und der Greenwood Frequenz eingeführt. Schließlich werden hier auch die Anwendung einer Adaptiven Optik zur Kompensation von atmosphärischen Wellenfrontstörungen, das Prinzip der Repräsentation von Wellenfronten mithilfe von Zernike Polynomen und die Restfehler aufgrund des Kompensationsprozesses erläutert.

In Kapitel 3 werden die Flüssigkeit für den Spiegel gewählt und die Eigenschaften des Systems untersucht. Eine wässerige Lösung von 80% Glycerin wird aufgrund ihrer entkoppelnden Eigenschaften gegenüber Umgebungsschwingungen und ihrer dennoch kurzen Regelzeiten von etwa 10 ms als Arbeitsflüssigkeit gewählt. Der theoretische Hintergrund der Wirkung von elektrostatischen Feldern auf Flüssigkeitsoberflächen wird erläutert, auf dessen Basis die Verformung der Flüssigkeitsoberfläche als Funktion der Systemparameter simuliert wird. Die Simulationen zeigen, dass die Halbwertsbreite der Verformung der Flüssigkeitsoberfläche hauptsächlich vom Durchmesser der Elektrode abhängt. Messungen von Verformungen der Flüssigkeitsoberfläche zeigen eine gute Übereinstimmung mit den Ergebnissen der Simulationen.

Die Theorie zur Bewegung von Flüssigkeiten in geschlossenen Behältern wird erläutert und die Eigenmoden des Flüssigspiegels daraus abgeleitet. Die Übertragungsfunktion der offenen Regelschleife wird vermessen und zeigt eine gute Übereinstimmung mit den Berechnungen. Die Bandbreite des Systems beträgt 80 Hz mit einer Amplitudenreserve von 11.4 dB und einer Phasenreserve von 140°. Die Anstiegszeit eines einzelnen Aktuators beträgt etwa 10.5 ms, während die Abfallzeit etwa 4.5 ms beträgt. Die Dämpfungszeitkonstante für den offenen und geschlossenen Regelkreis betragen $\tau_{\text{offen}} = 1.3$ s bzw. $\tau_{\text{geschlossen}} = 1.1$ s.

In Kapitel 4 wird die Leistungsfähigkeit des Flüssigspiegels untersucht. Zunächst wird der Flüssigspiegel zur Korrektur von statisch und dynamisch gestörten Wellenfronten verwendet. Der Korrekturfaktor des Spiegels wird als Verhältnis der Wellenfrontfehler des gestörten und des korrigierten Strahls ausgedrückt, entweder auf Basis des Strehlverhältnisses oder des rms-Wellenfrontfehlers. Der durchschnittliche Korrekturfaktor des Flüssigspiegels für statische Aberrationen beträgt $I_{\text{rms}} = 6.44$ auf Basis des rms-Wellenfrontfehlers und $I_{\text{S}} = 438$ auf Basis des Strehlverhältnisses. Die Untersuchung zur Korrektur sich zeitlich verändernder Wellenfrontstörungen zeigt, dass der Korrekturfaktor für dynamische Aberrationen von den Parametern des Regelsystems, z.B. der Verstärkung oder der Regelfrequenz, und der Stärke der Wellenfrontstörungen abhängt. Entsprechend der Erwartungen können für den Flüssigspiegel höhere Korrekturfaktoren für die Kompensation statischer als für zeitlich variierender Wellenfrontfehler von bis zu $I_{\text{rms, statisch}} = 12$ bzw. $I_{\text{rms, dynamisch}} = 4.5$ nachgewiesen werden. Die Auswirkung von Umgebungsschwingungen auf die Funktion des Flüssigspiegels wurde untersucht, wobei gezeigt werden konnte, dass der Flüssigspiegel diese teilweise kompensieren kann.

Außerdem wurde der Flüssigspiegel als Fine-Imager, d.h. zur hochauflösenden

Bildgebung, eingesetzt. Unterschiedliche Maße zur Bildschärfebewertung wurden evaluiert und auf vom Flüssigspiegel korrigierte Bilder angewendet, wobei gezeigt werden konnte, dass die Maße verschiedene Empfindlichkeiten für Änderungen der Bildschärfe aufweisen. Obwohl die Bildschärfeverbesserung quantitativ nur in begrenztem Umfang nachgewiesen werden konnte, hat der Flüssigspiegel die Bildschärfe sichtlich erhöht.

Zuletzt wurde der Flüssigspiegel als räumlicher Lichtmodulator eingesetzt und die Fähigkeit des Flüssigspiegels, Punkte, Linien und willkürliche Muster zu erzeugen, wurde demonstriert.

In Kapitel 5 wird die Skalierbarkeit des Flüssigspiegels untersucht. Im ersten Teil wird die Anzahl der Aktuatoren erhöht und der Betrieb des Flüssigspiegels mit 70 Aktuatoren erfolgreich demonstriert. Dabei wurde durch die Dynamik des Regelsystems eine Phase der Instabilität hervorgerufen, welche die Erhöhung der Anzahl der Aktuatoren aber nicht grundsätzlich limitiert.

Im zweiten Teil wird ein flüssiger Mikrospiegel entwickelt, welcher die Übertragung von Umgebungsschwingungen auf die Flüssigkeit verhindert. Es wird gezeigt, dass durch das Ätzen der Oberfläche eines Prismas mit einer wässrigen HF Lösung ein Wasserfilm mit einer sub-mm Schichtdicke geschaffen werden kann, welchen den Betrieb des Flüssigspiegels ohne zusätzlichen Flüssigkeitsbehälter ermöglicht. Die Eigenmoden und Frequenzcharakteristik des Flüssigkeitsfilms werden für Wasser und eine wässerige Lösung von 80% Glycerin bestimmt und es wird gezeigt, dass die Glycerinlösung durch die extrem langen Steigzeiten nicht für den Betrieb mit dem flüssigen Mikrospiegel geeignet ist. Für den Wasserfilm wird eine Bandbreite von etwa 3 Hz mit einer Amplitudenreserve von 14 dB und einer Phasenreserve von $162°$, einer Anstiegszeit für einen einzelnen Aktuator von etwa 2.5 s, einer Abfallzeit von etwa 0.4 s und einer Dämpfungszeitkonstante von $\tau_{offen} = 0.07$ s für den offenen Regelkreis gemessen. Abschließend wurden Anregungen für die weitere Entwicklung und Optimierung des flüssigen Mikrospiegels gegeben.

Kapitel 6 fasst die Ergebnisse und Schlussfolgerungen dieser Arbeit zusammen und gibt Empfehlungen für weitere Untersuchungen.

Die vorliegende Arbeit untersucht einen neuartigen deformierbaren Spiegel, dessen Wirkung auf der Formung einer Flüssigkeitsoberfläche durch elektrostatische Felder beruht. Dieser deformierbare Spiegel ermöglicht große Oberflächenauslenkungen, eine große Anzahl von Aktuatoren und die Möglichkeit zur Justierung der Spiegeleigenschaften und besitzt gleichzeitig einen einfachen Aufbau, der ohne anspruchsvolle Technik auskommt. Der Flüssigspiegel kann für die Korrektur dynamischer Wellenfrontstörungen eingesetzt werden sowie zum Fine-Imaging und als räumlicher Lichtmodulator. Der Flüssigspiegel kann für verschiedene Anwendungen in der adaptiven Optik eingesetzt und für weniger als 100 € realisiert werden.

"There's no such thing
As a self made man
It's not too hard
To understand

There's no such thing
As a self made man
'Cause everyone
Needs a helping hand"

Morcheeba,
Self Made Man, from the album
"Blood Like Lemonade," Pias Recordings 2010.

Acknowledgements

This work is a story of twists and turns – in particular, every aspect of this thesis has gone differently from what was originally planned and as such this thesis reflects everyday life. One obvious difference to the real world is that as you hold this book in your hands my work for this thesis is complete, I now can close this chapter of my life and look into the future where new exiting projects lie ahead. Although there is only one name on the cover of this book, many people have contributed to its creation.

First of all I want to thank Michael Gowin and Gleb Vdovin, without whom this whole effort would never have seen the light of day. Michael has supported and encouraged me the entire way and I immensely enjoyed our professional and personal discussions. Everybody should have someone that believes as strongly in them as Michael did in me. I thank Gleb for giving me this opportunity and making his lab and workshop available to me for the experimental work. His vast experience in Adaptive Optics, his insights, and his comments have all helped to improve the work and this thesis.

I am grateful to Paddy French for being my promotor and taking care of the administrative side of the dissertation.

"Every letter written," said a medieval abbot,
"is a wound inflicted on the devil."

T.H. White,
The Once and Future King, Ace Books 1987.

Publications

In scientific journals

- ten Have, E.S. and Vdovin, G., "Novel method for measuring surface tension," *Sensor. Actuat. A - Phys.*, **173** (1): 90 – 96, 2012.

- ten Have, E.S. and Vdovin, G., "Characterization and closed-loop performance of a liquid mirror adaptive optical system," *Appl. Optics*, **51** (12): 2155 – 2163, 2012.

In conference proceedings

- ten Have, E.S. and Vdovin, G.V., "Characterization and closed-loop AO performance of a liquid deformable mirror," in "Unconventional Imaging, Wavefront Sensing, and Adaptive Coded Aperture Imaging and Non-Imaging Sensor Systems," volume 8165 of *Proc. SPIE*, 816504 – 816504-8, 2011.

- ten Have, E.S. and Vdovin, G., "Physical and mechanical properties of a TIR-based liquid micro deformable mirror," in "Micro-Optics 2012," volume 8428 of *Proc. SPIE*, 84281W-1 – 84281W-11, 2012.

165

As a coauthor

- Kim, B.J., Flamma, J.W., ten Have, E.S., *et al.*, "Moulded photoplastic probes for near-field optical applications," *J. Microsc.*, **202** (1): 16 – 21, 2001.

- Kim, G.M., Kim, B.J., ten Have, E.S., *et al.*, "Photoplastic near-field optical probe with sub-100nm aperture made by replication from a nanomould," *J. Microsc.*, **209** (3): 267 – 271, 2003.

- Wirth, C., Schmidt, O., Tsybin, I., *et al.*, "2 kW incoherent beam combining of four narrow-linewidth photonic crystal fiber amplifiers," *Opt. Express*, **17** (3): 1178–1183, 2009.

- Wirth, C., Schmidt, O., Tsybin, I., *et al.*, "High average power spectral beam combining of four fiber amplifiers to 8.2 kW," *Opt. Lett.*, **36** (16): 3118 – 3120, 2011.

- Ludewig, K., Gowin, M., ten Have, E., *et al.*, "High brightness spectral beam combining to 8.2 kW," in "Fiber Lasers VIII: Technology, Systems, and Applications" volume 7914 of *Proc. SPIE*, 791401 – 791401-36, 2011.

Patents

- Hofmann, J., Gowin, M., ten Have, E., *et al.*, "Anzünd- bzw. Aktivierungs-einheit zum Anzünden von Rot-Phosphor-Flares mittels Laser," **DE 10 2009 030 868 B4**, filed 26.06.2009, issued 16.01.2014.

"Experience is the name every one gives to their mistakes."

Oscar Wilde,
Lady Windermere's Fan, Penguin Books 1995.

About the Author

Eric ten Have was born in Berlin, Germany, on August, 28th, 1973. After graduating from the Werner-von-Siemens Gymnasium in 1993 he moved to the Netherlands to study Applied Physics at Twente University in Enschede. In 1999 he received his MSc in Applied Physics from Twente University on the topic of a Čerenkov Free Electron Laser. He continued to work at the university on the topic of near-field scanning optical microscopy (NSOM) before switching to industry to work on various aspects of high-power lasers and their applications, including materials processing and the application of Adaptive Optics for free space beam propagation. In 2010 he joined the Electronic Instrumentation Laboratory at Delft University and started to collaborate with Dr. Vdovin on the topic of deformable liquid mirrors. Since 2012 he works as an Optoelectronics engineer for Corning Optical Communications in Berlin.